UNIVERSITY OF OKLAHOMA

GRADUATE COLLEGE

SURFACE AREA STUDY IN ORGANIC-RICH SHALES USING NITROGEN ADSORPTION

A THESIS

SUBMITTED TO THE GRADUATE FACULTY

in partial fulfillment of the requirements for the

Degree of

MASTER OF SCIENCE

By

ANKITA SHARADKUMAR SINHA
Norman, Oklahoma
2017

SURFACE AREA STUDY IN ORGANIC-RICH SHALES USING NITROGEN ADSORPTION

A THESIS APPROVED FOR THE
MEWBOURNE SCHOOL OF PETROLEUM AND GEOLOGICAL ENGINEERING

BY

_____
Dr. Chandra Rai, Chair

_____
Dr. Carl Sondergeld

_____
Dr. Mark Curtis

Dedicated to my God mother Guru Maa, my parents and my sister

Acknowledgements

I would like to begin by thanking the almighty who has made everything possible. I deeply thank my family for their constant support and trust while I pursued my studies. Their constant inspiration, boundless love and affection have helped me achieve this.

I express my sincere gratitude to my advisors Dr. Chandra Rai and Dr. Carl Sondergeld for their guidance during the course of my thesis. I thank them for giving me time and evaluating my work and giving invaluable suggestions. They are a constant source of motivation and an immense source to learn from. Successful completion of my thesis were possible with their support. I want to express my sincere thanks to Dr. Mark Curtis for his help and guidance during my studies at OU.

I also want to thank, Gary Stowe, Jeremy Jernigen, Bruce Spears and Mikki for making my lab work more comfortable. Jeremy's efforts in helping me with the SEM images was a big savior for me. I wholeheartedly thank the Unconventional Shale Gas Consortium and Experimental Rock Physics Consortium members for their invaluable suggestions and financial support to make this research possible.

Last but not the least I want to thank all my friends: Aashish, Charles, Dongho, Jiwon, Jyot, Maria, Sangcheol, Sama, Sarvesh, Sekar, Son, Subbu, Sweta, Trupti and Vineet who were my family here and made my stay in Norman delightful and enjoyable. They have made an immense contribution in my success.

Table of Contents

Acknowledgements iv

List of Tables viii

List of Figures x

Abstract xvii

Chapter 1: Introduction 1

1.1 Overview – Shales 1

1.2 Pore Characterization 1

1.3 Purpose and Scope of Study 3

1.4 Synopsis 4

Chapter 2: Literature Review 5

2.1 Literature Review 5

2.2 Adsorption 11

2.2.1 Categories of Adsorption 12

2.2.2 Adsorption Isotherms 12

2.2.3 Adsorption Hysteresis 15

2.3 Adsorption Mechanism 18

2.3.1 BET Theory 18

2.4 Micropore Volume Determination: The t-plot technique 20

2.5 Mesopore Analysis 23

2.5.1 Capillary Condensation 23

2.5.2 BJH Method 24

2.5.3 Density Functional Theory Method 26

2.6 PSD Inversion Technique: BJH or DFT? 28
Chapter 3: Experimental Procedure 31
3.1 Introduction 31
3.2 Experimental Workflow and Sample Description 31
3.3 Methods 32
3.3.1 Nitrogen Adsorption 33
3.3.2 Solvent Extraction 40
3.3.3 Gas Chromatography-Mass Spectroscopy 40
3.3.4 Extra porosity Determination 42
3.3.5 Kerogen isolation 42
Chapter 4: Results and Discussions 43
4.1 Sample Mineralogy 43
4.2 Total Organic Carbon 45
4.3 Source Rock Analysis 47
4.4 Crushed Helium Porosity and Extra Porosity as a function of Maturity 49
4.5 SEM 53
4.6 Adsorption / Desorption Isotherms for shales and kerogens 58
4.6.1 Low pressure N_2 analyses – Organic rich shales 58
4.6.2 Pore size distribution for organic rich shales 63
4.6.3 Isolated Kerogen 72
4.6.4 Pore size distribution for isolated kerogens 75
4.7 Surface area correlation with clay, TOC and thermal maturity on adsorption 78
4.7.1 Immature window 85

4.7.2 Oil window 86
4.7.3 Condensate window 87
4.7.4 Gas window 88
4.8 Dependance of surface area on maturity of kerogens 93
4.9 Economic Analysis 94
4.10 Summary – Analysis of adsorption capacity of different shales. 96
Chapter 5: Conclusions 97
References 99
Appendix A: Experimental Procedure 110
1. Nitrogen Adsorption Procedure 110
2. Transmittance FTIR Mineralogy 111
3. Total Organic Carbon Determination 111
4. SRA™ 112
5. Scanning Electron Microscopy 113
6. Kerogen isolation procedure 113
7. Derivation for Extra Porosity 114
Appendix B: Sample Description 115

List of Tables

Table 1: Hysteresis Loop Types (Condon, 2006) 16

Table 2: List of clay minerals with its source 36

Table 3: Comparison of clay surface area from this study and literature studies based on N_2 adsorption isotherms. 39

Table 4: Summary of the measured specific surface areas for the samples shown in Fig 22. 62

Table 5: Statistical evaluation of TOC, clay and maturity on surface area in the "as-received" state. 84

Table 6: Statistical evaluation of TOC, clay and maturity on surface area post extraction. 90

Table 7: Data for estimating the in place reserves for oil and gas reservoirs. 94

Table B-1: Lower Bakken - Mineralogy, TOC, Porosity and Surface area (Immature)…….115

Table B-2. Wolfcamp 1 – Mineralogy, TOC, Porosity and Surface area (Immature)..123

Table B-3: Wolfcamp 2 – Mineralogy, TOC, Porosity and Surface area (Oil) 1124

Table B-4: Eagle Ford 1 – Mineralogy, TOC, Porosity and Surface area (Oil) 125

Table B-5: Wolfcamp 3 – Mineralogy, TOC, Porosity and Surface area (Condensate)……..118

Table B-6: Wolfcamp 4 – Mineralogy, TOC, Porosity and Surface area (Condensate)……..118

Table B-7: Woodford – Mineralogy, TOC, Porosity and Surface area (Condensate)..119

Table B-8: Barnett – Mineralogy, TOC, Porosity and Surface area (Gas)……....120

Table B-9: Marcellus – Mineralogy, TOC, Porosity and Surface area (Gas)……...120

Table B-10: The maturity and the BET surface area of different kerogens. The samples highlighted in gray are from this study and compared with the data from literature…121

Table B-11: Mineral content, Organic matter content and the thermal maturity of the formations……..123

Table B-12: Geochemical properties of Eagle Ford-1 formation (Oil Window)……..124

Table B-13: Geochemical properties of Wolfcamp-2 formation (Oil Window)……...125

List of Figures

Fig. 1: Classification of adsorption isotherms (Sing et al., 1985). Type I isotherm is for microporous solids, Type II and Type III for non-porous and macroporous solids, Type IV for mesoporous solids, Type V and Type VI are characteristic curves observed in rare case (after Lowell, 2006). 14

Fig. 2: The four classifications of adsorption isotherms with hysteresis loops (IUPAC, 1985). Significance of each characteristic curve is provided in Table 1. 16

Fig. 3: N_2 adsorption isotherm at 77.36K of a Woodford shale sample. The isotherm 'forced closure' is observed in the relative pressure range 0.40-0.55 due to the *tensile strength effect*. 17

Fig. 4: Typical BET Plot (slope and intercept help determine BET constant "C" and volume of adsorbed monolayer Vm).....18

Fig. 5: V-t curve for Type I isotherm, (after Lowell et al. 2006).....20

Fig. 6: An example of V-t curve for a sample showing filling of micropores. The lines in above figure correspond to the filling of micropores. (after Lowell et al. 2006) 22

Fig. 7: Schematic representation of multilayer adsorption, pore condensation and hysteresis in a single cylindrical pore (after Lowell et al. 2006) 24

Fig. 8: (a) Model isotherm (quantity adsorbed versus pressure) for argon in a 4 nm slit pore by DFT method. (b) Collection of model isotherms with different pore sizes (H), used to obtain the pore size distribution. (images from Micromeritics software manual, 2012).....27

Fig. 9: PSD obtained from the inversion of N_2 gas adsorption data for a Wolfcamp shale sample from oil window using different thickness equation in the BJH method. The PSD

shows similar peaks but the absolute volume differs depending on the thickness equation used.....29
Fig. 10: An example of PSD of a Wolfcamp shale sample from oil window obtained using DFT kernels with N_2 as the adsorbate. 29
Fig. 11: The model fit to the experimental adsorption data obtained for the Wolfcamp shale sample from oil window shown in Fig. 10. The average fitting error between the experimental and theoretical isotherm for DFT analysis as shown above is less than 0.9%. 30
Fig. 12: Flow chart summarizing the measurement sequence and the scope of the measurements. Part A: Samples are first analyzed in the "as-received" state and then solvent extracted as shown in Part B and reanalyzed.....32
Fig. 13: Schematic of a sample tube placed in dewar containing liquid nitrogen, LN_2, at cryogenic temperature of -196°C (77.36K). 34
Fig. 14: Adsorption-desorption isotherms using nitrogen at 77.36 K for carbon black (standard reference) in test ports 1, 2 and 3. The isotherms do not show hysteresis confirming the carbon black sample used is non-microporous. 36
Fig. 15: Adsorption-desorption isotherms using nitrogen at -196°C (77.36K) for powders of illite, kaolinite, montmorillonite and smectite. The hysteresis effect is prominent in illite, montmorillonite and smectite and not in kaolinite. This indicates that micro-, meso- and macropores dominate in illite, montmorillonite and smectite while macropores dominate in kaolinite. 38
Fig. 16: An example of GC-MS spectrum used to analyze residual hydrocarbon composition. Each of the major peaks corresponds to different alkanes from C_{11}-C_{30+}. 41

Fig. 17: Average FTIR mineralogy of the shales presented in this study 44

Fig. 18: Box and whisker plot of TOC measured in different shale formations plotted based on their maturities. The cross marks in each bar represents the average TOC value.The average TOC values for immature, oil, condensate and gas in their as-received state are 8.6, 5.8, 4.9, 4.9 wt% respectively. The TOC value reduces post extraction showing maximum reduction in the oil window and least in the gas window. N indicates the number of samples in each maturity window. 46

Fig. 19: Box and whisker plot of SRA S_1 peak values pre- and post-extraction for shale samples from different maturity windows. The change in S_1 peak post-extraction is significant indicating the removal of producible liquid hydrocarbons and a part of bitumen that are generated below 300°C. Gas shale samples do not show any S_1 peak affirming the conversion of the hydrocarbons to the gas. 47

Fig. 20: Box and whisker plot of SRA S_2 values pre- and post-extraction for shale samples from different maturity windows. The change in S_2 peak post-extraction is minor in comparison to the S1 peak. Similar to the S_1 peak the samples from the gas maturity window do not show significant presence of S_2 peak. 48

Fig. 21: Box and whisker plot of crushed helium porosity for different maturity shales pre- and post- solvent extraction. The cross marks in each histogram represents the average porosities in each case. The average percentage increase in porosity for immature, oil, condensate, and gas window are 93%, 39%, 19% and 10%, respectively. The increase in porosity post-extraction is high in the liquid rich shales implying the presence of soluble HC's leading to an underestimation of the effective porosity of the shales in the "as-received" state. N indicates the number of samples in each maturity window. 50

Fig. 22: Relationship between extra porosity and TOC – post extraction, wt% for different thermal maturity window. The strongest correlation coefficients are obtained with the immature and oil window. 51

Fig. 23: Relationship between extra porosity with TOC, wt.%. The extra porosity was obtained due to removal of soluble hydrocarbons during Soxhlet extraction. 52

Fig. 24: SEM images of the immature shale from the Lower Bakken formation.....53

Fig. 25: Alteration in organic microstructure before and after solvent extraction in Eagle Ford - late oil window (clay – 14.3 wt% and TOC – 5.2 wt%) sample qualitatively providing information about the location of the pores throughout the sample. In each case, the size of the pores within the organics increases upon solvent extraction. 55

Fig. 26: Organic porosity as a function of thermal maturity (Curtis et al. 2012). A weak positive correlation can be observed. This implies thermal maturity is a contributing factor but not the sole factor controlling adsorption. 56

Fig. 27: SEM images of the gas shale from the Marcellus formation (clay – 72 wt%, TOC – 4.5 wt%) showing abundant organic pores. There is no change in the microstructure pre- and post-extraction. The pores associated with clay minerals appear to be slit-shaped. 57

Fig. 28: Adsorption-desorption isotherms of the shale sample from: a. Bakken (immature), b. Wolfcamp 2 (oil), c. Wolfcamp 4 (condensate) and d. Marcellus (gas) formations. The isotherms for the native and clean samples from each formation are shown. In all but the Marcellus isotherm for the “as-received” sample shows a substantial surface area implying the presence of abundant nanopores. The circles represent the “as-received” state and the diamonds represent the solvent extracted state. 61

Fig. 29: Comparison of PSD for immature, oil, condensate, and gas window. The graph for differential and cumulative pore volume from each maturity is shown as a function of pore width derived from the N_2 adsorption branch of the isotherms using the DFT model. 68

Fig. 30: Comparison of surface area distribution with pore size derived from N_2 adsorption isotherm using DFT model for varying maturity samples. 69

Fig. 31: N_2 differential surface area plots for selected samples from varying thermal maturity window subjected to solvent extraction. Plots were generated using the DFT method applied to the adsorption branch of the isotherms. The maximum change in surface area was observed in the oil window suggesting removal of movable hydrocarbons from the finer mesopores. 71

Fig. 32: Nitrogen adsorption and desorption curves for different kerogen samples from the immature window. 73

Fig. 33: Nitrogen adsorption and desorption curves for different kerogen samples from the oil window.....74

Fig. 34: Nitrogen adsorption and desorption curves for different kerogen samples from gas window. 74

Fig. 35: Plots showing pore volume distributions with pore diameter derived from the N_2 adsorption branch of isotherms for Woodford, Bakken and Eagle Ford kerogens using BJH model. 76

Fig. 36: Plots showing pore surface area distributions with pore diameter derived from the N_2 adsorption branch of isotherms for Woodford, Bakken and Eagle Ford kerogens using BJH model. The abrupt increase in the pore volume (6 – 10 nm) for the Eagle Ford

sample can be due the irregular fit of the adsorption isotherm data points with the BJH model. 77

Fig. 37: Relationship between BET-surface area and clay for "as-received" shale samples from different maturity windows. The surface area shows a weak positive correlation with amount of clay. The surface area increases as a function of maturity from as 1.14 m^2/g (Wolfcamp 1 – immature) to as high as 41.51 m^2/g (Marcellus – gas). The low surface area in the immature window can be attributed to the presence of soluble hydrocarbons coating the surface os the shale samples, masking the true surface area. The increase in surface area with increasing maturity is attributed to the generation of nanopores.....79

Fig. 38: Relationship between BET-surface area and TOC for "as-received" shale samples from different maturity windows. The surface area shows a considerable scatter. There is no definite correlation observed between the two variables. 80

Fig. 39: Cross-plot of "as-received" surface area with illite content. The data set from all the maturity is plotted and shows a weak positive correlation between the two parameters. The vertical line at 20 wt% illite is indicative of two different relationships observed. Lower illite content (< 20 wt%) do not show any correlation with specific surface area whereas, illite content greater than 20 wt% shows a weak positive relation.....81

Fig. 40: Box and whisker plot of N_2-BET surface area in the "as-received" state for all wells, sorted by increasing maturity. The black line inside the bars is the median and the cross marks is the average. The wide range of values (e.g. Marcellus) may be indicative of the sedimentary variability. 82

Fig. 41: Relationships between BET-surface area with clay and TOC for “as-received” and solvent extracted state for the samples in the immature window (Bakken-dark orange, Wolfcamp 1-light orange).....85

Fig. 42: Relationships between BET-surface area and clay and TOC for “as-received” and solvent extracted state for the oil window (Eagle Ford 1-maroon, Wolfcamp 2-red) shale samples. 86

Fig. 43: Relationships between BET-surface area with clay and TOC for “as-received” and solvent extracted state for the condensate window (Eagle Ford 2-blue, Wolfcamp 3-light blue, Wolfcamp 4-dark blue, Woodford-purple) shale samples. 87

Fig. 44: Relationships between BET-surface area with clay and TOC, for “as-received” and solvent extracted state for the gas window (Barnett-dark green, Marcellus-light green) shale samples. 88

Fig. 45: Box and whisker plot for the 10 wells from six different shale formations showing the increase in surface area with increasing thermal maturity. The black cross marks shown in the figure are the mean values for each dataset. The average percentage increase in immature, oil, condensate, and gas window are 175%, 136%, 101% and 15% respectively. 92

Fig. 46: Graphical representation of the data reported in Appendix B, Table 15. The graph consists of data points from this study (blue dots) and from the literature (Rexer et al., 2014; Cao et al., 2015; Hu et al., 2015; Wang et al., 2015) (red dots). The increasing trend observed in BET surface area with increasing maturity from immature to over mature is in agreement with the previous studies in the literature. 93

Abstract

Low-pressure nitrogen adsorption technique was used to investigate the specific surface area and pore size distributions and controlling factors for 11 wells from seven different shale formations with varying thermal maturity, organic matter content and clay content. The pore structure of these shales and isolated kerogen were studied using nitrogen adsorption and SEM imaging. We show that low maturity samples from the immature window have very low specific surface areas ranging from 1.13 to 6.91 m^2/g; in contrast, samples in later stages of maturity have higher specific surface area ranging from 2.14 to 41.51 m^2/g. In the organic-rich shales, incorrect estimation of surface area leads to erroneous quantification of the pore size distribution. Surface areas measured in the "as-received" (before solvent extraction) state did not show a strong dependence on total clay or organic content although these two components have high surface areas. Underestimation of surface area is due to the non-removal of residual water and soluble hydrocarbons, including bitumen. We tested this proposal by extracting the shale samples using an 4:1 toluene:methanol azeotrope at 63.8°C in a standard Soxhlet extractor. Geochemistry and pore network attributes before and after removal of soluble hydrocarbons were characterized. Results show that the TOC, S_1, S_2 of the extracted samples decrease significantly and the extraction process greatly increases the specific surface area and pore volume of the samples. The increase in the specific surface area is maximum in the immature window having an average increase of 175% and minimum in the gas window having an average increase of 15%. We determined an empirical relationship between surface area, TOC and clay content for various maturity windows. Our results indicate that the specific surface area is a function of maturity and gas

adsorption increases with organic pore generation as an outcome of maturation. Grain density measurements pre- and post-solvent extraction were used to determine the "extra-porosity" associated with soluble bitumen and residual hydrocarbons in varying maturity window and then correlated with TOC. Solvent extraction increased porosity by an average of 93% in the immature window, 39% in oil window, 19% in condensate window, and 10% in the gas window. We show for isolated kerogen, the low-maturity samples have very few nanopores in addition to having very low specific surface areas ranging from 3.74 to 9.24 m^2/g. In contrast, nanopores are abundant in the mature to over mature kerogen, leading to high specific surface areas in range of 15.81 to 41.96 m^2/g.

Chapter 1: Introduction

1.1 Overview – Shales

Shales constitute more than 75% of the sedimentary rock in the earth's crust and are characterized by fissility and the presence of fine-grained rocks made of clay- and silt-sized particles which are typically less than 4 microns and not greater than 62.5 microns in diameter (Folk, 1974; Friedman 2003). They are characterized by low porosity (< 10%) and ultra-low permeability, i.e. in nanodarcy range. Shales, due to their nanodarcy permeabilities were considered reservoir seals, preventing the escape of hydrocarbon from conventional reservoirs. Potter et al. (2005) and Boggs (2012) defined shales as laminated fine-grained argillaceous rock. Passey (2010) defined shale resources as 'unconventional reservoirs', since they do not produce economic rates of hydrocarbons without stimulation and commonly referred them as mudstones. Bohacs (1998), Bohacs et al. (2005), Guthrie and Bohacs (2009) studied the shale formations rich in organic matter (OM) and concluded that even if the formations appear largely homogeneous, the vertical variability in the organic richness can occur on relatively short vertical scales (often much less than 1 meter). Cramer (2008) stated that each shale is different in its geology, geochemistry and geomechanical properties and requires unique drilling, completion and production techniques.

1.2 Pore Characterization

Shales have a heterogeneous and a complex microstructure. The heterogeneity in the micropores is influenced by organics, thermal maturity/diagenesis, and inorganics (Hao et al., 2013). Understanding the complex pore system is crucial in evaluating the storage

and transport properties of these unconventional shale resources (Chen et al., 2013; Guo et al., 2013; Tian et al., 2013). Fu et al. (2015) defined the pore structure as the geometric shape, size and distribution of pores and throats and their connectivity in geo-reservoirs. The pore structure of shale oil and shale gas reservoirs is difficult to characterize because of the nanopore structure, associated with OM content, and a broad pore size distribution (PSD) unique to every shale sample studied. The generation of these nanopores takes place during the burial and subsequent maturation of the OM (Bernard et al., 2012; Jarvie et al., 2007).

A diverse array of pore structures have been documented (e.g. Loucks et al., 2012 and Milliken et al., 2013) which are dependent on grain size, mineralogy, organic matter (OM) content that create a unique reservoir texture which in turn varies with burial depth, thermal maturity and chemical diagenesis. Methods such as low-pressure carbon dioxide (CO_2) and nitrogen (N_2) and mercury intrusion porosimetry (MIP) have been used to quantify the pore size distributions and pore throat distributions (Ross and Bustin, 2009; Chalmers et al., 2012; Clarkson et al., 2013; Kuila and Prasad, 2013). The pore structures that are documented in these studies are method dependent and studies have yielded different results because of the methods employed. Ambrose (2011) concluded that porosity and PSD are crucial from the viewpoint of estimation of shale gas reservoir volume and reservoir quality. Ross and Bustin (2009), Mastalerz et al. (2013), Zhu et al. (2013), Chalmers et al. (2012) concluded that OM is the main host of the pores, which provides the adsorption site and storage space for gas adsorption.

For conventional rocks, the porosity and PSD are measured using helium expansion and mercury intrusion (MICP) techniques. Hossain et al. (2011) showed that above-mentioned approach yields consistent results for conventional sandstone and carbonate rocks. Currently low-pressure CO_2 and N_2 gas adsorption techniques has been adopted by researchers, in addition, to the conventional crushed helium porosity measurements and mercury porosimetry to understand the PSD and total pore volumes in shales (Katsube et al., 1998; Ross and Bustin 2007, 2008; Chalmers and Bustin 2008; Wang and Reed 2009; Kuila and Prasad, 2013). Researchers recommended using Scanning Electron Microscopy (SEM) to image the microstructure of shales and to understand the characteristics of the different pore types. Combining these results with the gas adsorption and MICP provides a more comprehensive analysis of pores and their distributions in shale.

1.3 Purpose and Scope of Study

The pore size terminology of the International Union of Pure and Applied Chemistry (IUPAC), which was developed by Sing et al. (1985), has been used to classify pores in shales. According to this classification, the pores are divided into three categories:

a. Micropores: pores less than 2 nm diameter
b. Mesopores: pores in range of 2 nm and 50 nm in diameter, and
c. Macropores: pores greater than 50 nm in diameter.

This classification of pores is based on the physics of nitrogen adsorption in various pore sizes at -196°C (77.36 K). Various mechanisms, such as micropore filling (micropores),

combination of multilayer adsorption and capillary condensation (mesopores), and multilayer adsorption (macropores) dominate in the different pore sizes.

This study attempts to use the nitrogen adsorption technique (BET – surface area) to achieve the following objectives:

1. To understand the effect of rock components (clay and TOC) and thermal maturity on specific surface area measurements using the principal of nitrogen adsorption on various shale formations from Barnett, Eagle Ford, Lower Bakken, Marcellus, Vaca Muerta, Woodford and Wolfcamp.
2. To evaluate the impact of solvent extraction using toluene and methanol (4:1) on surface area, PSD, porosity and pyrolysis measurements in organic rich shales.
3. To determine correlation between surface area, clay content, organic content and thermal maturity pre- and post- solvent extraction.
4. To investigate the specific surface area of kerogen isolated from organic rich shales.

1.4 Synopsis

This study is divided into 5 chapters. Chapter 1 provides an introduction for the study and the motivation. Chapter 2 discusses the theory and principles behind gas adsorption measurement and previous studies related to the field. Chapter 3 describes the experimental procedures used in petrophysical, geochemical measurements and subcritical N_2 gas adsorption measurements. Chapter 4 summarizes the results and their applications. Chapter 5 presents the conclusions and findings from our studies.

Chapter 2: Literature Review

Low-pressure isothermal gas adsorption measurements using liquid N_2, CO_2 and CH_4 have been used extensively by several researchers (Ross and Bustin, 2009; Chalmers et al., 2012; Kuila and Prasad, 2013; Labani et al., 2013). These studies have been carried out on shales for nearly a decade, in particular to quantify the various pore network attributes (surface area, pore volume and pore size distribution). Understanding and quantifying these pore network attributes are crucial to modeling the behavior of fluids in porous media. Estimating the specific surface area of shales is crucial in estimating gas storage, since natural gas is adsorbed on the internal surfaces of the pores contributing to large gas storage capacity. Porosity and pore size distribution are essential in calculating the reservoir storage or economics.

2.1 Literature Review

Shales have received great attention in the recent years because of their emergence as commercial hydrocarbon resources in North America (Curtis, 2002; Montgomery et al. 2005; Bowker 2007; Jarvie et al., 2007; Scheiber, 2010; Sondergeld et al., 2010b; Slatt and O'Brien, 2011). Attributes of the pore structure are porosity and pore size distribution (PSD). Nimmo (2004) said, 'porosity is a single value quantification' and it does not consider heterogeneity of pore structures that occur in nature. The other attribute used for characterizing the pore structure is the pore size distribution (PSD), which quantifies the volumes associated with the different pore sizes. The simplest model developed for inverting experimental data to the PSD is the capillary bundle approximation, where the

porous material is assumed to contain stack of open-ended cylindrical capillaries with different diameters.

Porosity and PSD are used for reservoir evaluation (Ambrose et al., 2010), permeability prediction (Nelson, 2009), and elastic property calculations (Kuila and Prasad, 2013). A major challenge in estimating the transport and storage capacity of the shales is the poor understanding of their pore properties including size, distribution and pore hosting components (Nelson, 2009; Chalmers et al., 2012; Loucks et al., 2012; Kuila et al., 2014). The main deterrent to reliable and accurate laboratory measurements is lack of accessibility of the displacement fluids to the pore system. Saidian et al. (2015) states the reason for limited accessibility of the displacement fluids can be due to extremely low permeability, complicated mineral surface and fluid interactions or insufficient equilibration time.

The visual analysis of the pore shapes, pore sizes and its distribution have been conducted using field emission scanning electron microscopy/transmission electron microscopy (FE-SEM/TEM) and focused ion beam scanning electron microscopy (FIB-SEM) by (Loucks et al., 2009; Curtis et al., 2010; Lemmens et al., 2011; Bernard et al., 2012; Chalmers et al., 2012; Curtis et al. 2012; Milliken et al., 2013). In addition to the qualitative estimation, the presence of micropore and mesopore spaces in a shale matrix has been documented by several researchers over the last decade, using non-visual techniques. Some examples of non-visual techniques are low-pressure gas adsorption (Ross and Bustin, 2009; Chalmers et al., 2012; Clarkson et al., 2013), mercury intrusion

(Howard, 1991; Mathhews et al., 1995) and NMR (Sondergeld et al., 2010a; Jiang et al., 2013; Rivera et al., 2014; Saidian et al., 2015).

Surface area and pore size distribution of nanopores have been studied through low pressure N_2 and CO_2 gas adsorption technique coupled with high pressure mercury injection capillary pressure (MICP) (Ross and Bustin, 2009; Mastalerz et al., 2012; Clarkson et al., 2013; Kuila and Prasad, 2013; Labani et al., 2013; Schmitt et al., 2013) and small angle and ultra-small angle neutron scattering techniques (SANS/USANS) (Clarkson et al., 2012; Mastalerz et al., 2012). Mercury intrusion technique is preferred for measuring porosity and obtaining the PSD for conventional reservoir rocks where pores are characterized by micrometer scale (Mathhews et al., 1995; Clarkson et al., 2012; Mastalerz et al., 2013). In shales, MICP can potentially create some artificial macropores and also cause particle deformation since shales are weak in comparison to conventional rocks (Giesche, 2006; Bustin et al., 2008; Sigal, 2009). On the contrary, the low-pressure gas adsorption technique does not create artificial macropores during the measurement but relies on an imperfect inversion model to determine the PSD within the limited range of 2 to 200 nm.

Most of the gas adsorption measurement are performed using liquid nitrogen as the adsorbate at 77.36 K and relative pressure (*P/Po*) range of 0.05 – 0.99. One limitation of using N_2 as the adsorbate at 77.36 K is that the molecules cannot enter into the micropores (< 2 nm) (Gan et al., 1972; Ross and Bustin 2009) and another is that this temperature is hardly reservoir temperature. However, using CO_2 at 273.1 K, micropores between 0.5

and 2 nm can be characterized (Ross and Bustin 2009). The cross-sectional area of CO_2 molecules is 0.17 nm^2 which is smaller than N_2, thus enabling it to access pores between 0.5 nm to 2 nm. Studies indicate that single-point BET method can be used to compute the specific surface area of these micropores and using the Density Functional Theory (DFT) to characterize the pore distribution. BET has been used by Ross and Bustin (2009), Adesida (2011), Chalmers et al., (2012), Kuila and Prasad (2013) to characterize nanopores in shale.

Bustin et al. (2008) recommended using a combination of low pressure gas adsorption measurement with the MICP to overcome the problems associated with the inability of low pressure gas-adsorption techniques and high-pressure mercury intrusion (MICP) to capture small and large pores respectively. They studied shales from the Antrim and Barnett formations (particle size < 60 mesh and degassing at 110°C) and reported bimodal size distributions with modes at 10 nm and around 10,000 nm, using a combination of low pressure CO_2 and N_2 adsorption and MICP. However, the authors did not distinguish between the pore-throat and the pore-body size distributions that were obtained as a result of the different techniques, but acknowledged the disagreement in pore volume in the overlapping region due to different theoretical assumptions used in the inversion.

Ross and Bustin (2009) studied the pore structure of the Devonian-Mississippian and Jurassic shales (particle size < 60 mesh and degassing at 110°C) from Western Canadian Sedimentary Basin using combination of high pressure CH_4 adsorption, low pressure CO_2 and N_2 adsorption measurements and MICP. They reported positive correlation between

the micropore volumes and the TOC content of the organic rich shales, indicating that micro-porosity associated with the organic fraction is a primary control on CH_4 adsorption. In addition, they observed a good correlation between clay content and the total mercury intrusion porosity and a systematic change in pore structure with increasing clay content. Their work could not exclusively address the effect of clay minerals on gas adsorption because of the co-existence of organic matter.

Lu et al. (1995), Ross and Bustin (2007), Cui et al. (2009) used CH_4 adsorption on several shale formations and reported a positive correlation of CH_4 adsorption capacity with the TOC in shales. Chalmers and Bustin (2008) conducted high pressure (6 MPa) methane adsorption measurements on Lower Cretaceous gas shale sample from Northeastern British Columbia. The authors reported a strong positive correlation between the adsorption capacity and the TOC, implying TOC content is the primary control on the methane adsorption capacity. Chalmers et al. (2012), Curtis et al. (2012), Wang et al. (2013), stated that the main factors controlling the organic pore structure are the type and content of OM and the maturity of shale.

Hou et al. (2014) studied lower Paleozoic marine shale and Mesozoic continental shale to investigate the effect of pore structure characteristics on the methane adsorption of shale using a combination of FE-SEM, low pressure N_2 adsorption (particle size 10-14 mesh) and high pressure CH_4 adsorption measurements. They observed a positive correlation between the organic content, N_2 – BET surface area and adsorption capacity, implying micro-porosity associated with organic fraction in these shales is the key factor

controlling the methane adsorption capacity. They also concluded that the major pore system of shale reservoir changes from inorganic matter pores to organic matter pores with the increasing thermal maturity thereby increasing the methane adsorption capacity of shale.

Fu et al. (2015) analyzed 40 lacustrine shale samples of the Mesozoic Yanchang Formation in the Ordos Basin, to investigate the factors that influence the development of pore structure. The authors used both the qualitative and quantitative methods to study the pore type and size distribution using SEM, nano-computed tomography (CT), N_2 adsorption and low-field nuclear magnetic resonance (NMR) imaging. The results show that the pore and throat structures are dispersed in three dimensional space with spherical, tubular and irregular shapes. The results also show that the micro- and mesopores provide the main specific surface areas of pores, whereas mesopores provide the primary pore volume. The TOC, mineral components, and thermal maturity are the main factors that control the development and evolution of pore structure in lacustrine shale.

Apart from the traditional way, i.e. using the "as-received" sample state for measuring the various pore network attributes (surface area, pore volume and pore size distribution), some researchers (Wei et al., 2014; Ghanizadeh et al., 2015; Wood et al., 2015) proposed using the solvent extraction technique to identify the impact of the maturation and formation of solid bitumen on the pore connectivity. Furmann et al. (2013) studied the impact of solvent extraction on two high-volatile bituminous coals from the Illinois Basin to understand the degree of bitumen extractability. The study reported an increase in

microporosity (using CO_2 adsorption after extraction) and a shift in pore size distribution from meso- to macro- attributing this effect to the alteration of OM porosity for samples when cleaned with organic solvents. Valenza et al. (2013) compared the pre- and post-solvent (dichloromethane:methanol in 9:1 ratio) extraction data for various maturity windows and concluded the impact of cleaning was significant in the early mature window. Wei et al. (2014) conducted a similar research using series of solvent (DCM for 72 hours followed by toluene for 96 hours) extraction on samples from New Albany organic rich shales. They reported that the process of solvent extraction opens additional pore space for N_2 and CO_2 adsorption which is previously masked due to the presence of oil and bitumen.

In this study, PSD and specific surface area were quantified using N_2 adsorption isotherms and their relation to the amount of clay present, OM content, thermal maturity was studied for the samples pre- and post-solvent extraction. Specific surface area was determined using the multi-point BET method and the PSD was obtained using the DFT model (**discussed in Section 2.5.3**). Image analyses for the shale samples from various maturity windows before and after solvent extraction were done using SEM.

2.2 Adsorption

Adsorption is defined as the "phenomenon of attracting and retaining the fluid molecules on the solid surface resulting in a higher concentration of the molecules on the surface" (Barnes and Gentle, 2005). The solid is called the adsorbent while the fluid molecules adhering to its surface are known as the adsorbate.

2.2.1 Categories of Adsorption

Depending upon the strength of interaction between the fluid molecules and the solid, adsorption can be divided into two categories Lowell (1979) namely:

- Physical Adsorption: also, known as physisorption is a process in which the force of attraction existing between the adsorbate and the adsorbent are weak Van der Waals forces of attraction. It takes place with formation of multilayer of adsorbate on adsorbent.
- Chemical Adsorption: also, known as chemisorption is a process in which the force of attraction existing between adsorbate and adsorbent are chemical forces of attraction or chemical bond. It takes place with formation of unilayer of adsorbate on adsorbent.

2.2.2 Adsorption Isotherms

An adsorption isotherm provides a relationship between the amount of adsorbate adsorbed on the solid surface and the relative pressure (concentration) of the adsorbate in the fluid phase under equilibrium condition. The isotherm shape and the hysteresis pattern obtained provide useful information about the physisorption mechanism, energy interaction between the solid and gas; the shape is used to predict the types of pores present in the adsorbent. The International Union of Pure and Applied Chemistry (Sing et al., 1985) classified the adsorption isotherms into six types (Type I to VI) and four hysteresis pattern types (H_1 to H_4) based on the extensive research, performed by Brunauer, Emmet and Teller (1938). An elaborate description of the IUPAC adsorption

isotherm classification is presented in Sing et al. (1985) and Rouquerol et al. (1998). The isotherm types are shown in **Fig. 1**.

Type I isotherm: This isotherm is concave to the relative pressure axis and the isotherm shape is observed with microporous solids.

Type II isotherm: This type of isotherm is concave in the initial region to the relative pressure axis, then linear and finally convex at higher relative pressure. This type of isotherm profile does not exhibit a saturation limit and indicates an unrestricted monolayer-multilayer adsorption after monolayer completion. Point B (knee) observed in the isotherm indicates completion of monolayer adsorption and initiation of adsorption of successive multilayers. The isotherm is completely reversible and is typically exhibited by nonporous or macroporous solids.

Type III isotherm: This type of isotherm is convex to the relative pressure axis and does not show multilayer adsorption and the isotherm is indicative of non-porous or macroporous solids with weak adsorbate-adsorbent interactions. This type of isotherm is not observed in shales.

Type IV isotherm: This type of an isotherm is a variation of Type II isotherm but with a finite multi-layer formation corresponding to the phenomenon of capillary condensation and evaporation. The hysteresis loop observed in Type IV isotherm is a characteristic of mesopores.

Type V isotherm: This isotherm is initially convex to the relative pressure axis. It exhibits hysteresis indicating the mechanism of pore filling and emptying (condensation).

Type VI isotherm: This type shows a stepped adsorption isotherm. This type of isotherm is associated with adsorption on uniform surface. The sharpness of steps depends on pressure and temperature of the adsorbate.

Of the six isotherms shown in **Fig 1**, the most important for unconventional shale gas formation evaluation are Type I, Type II and Type IV (Kuila and Prasad 2013).

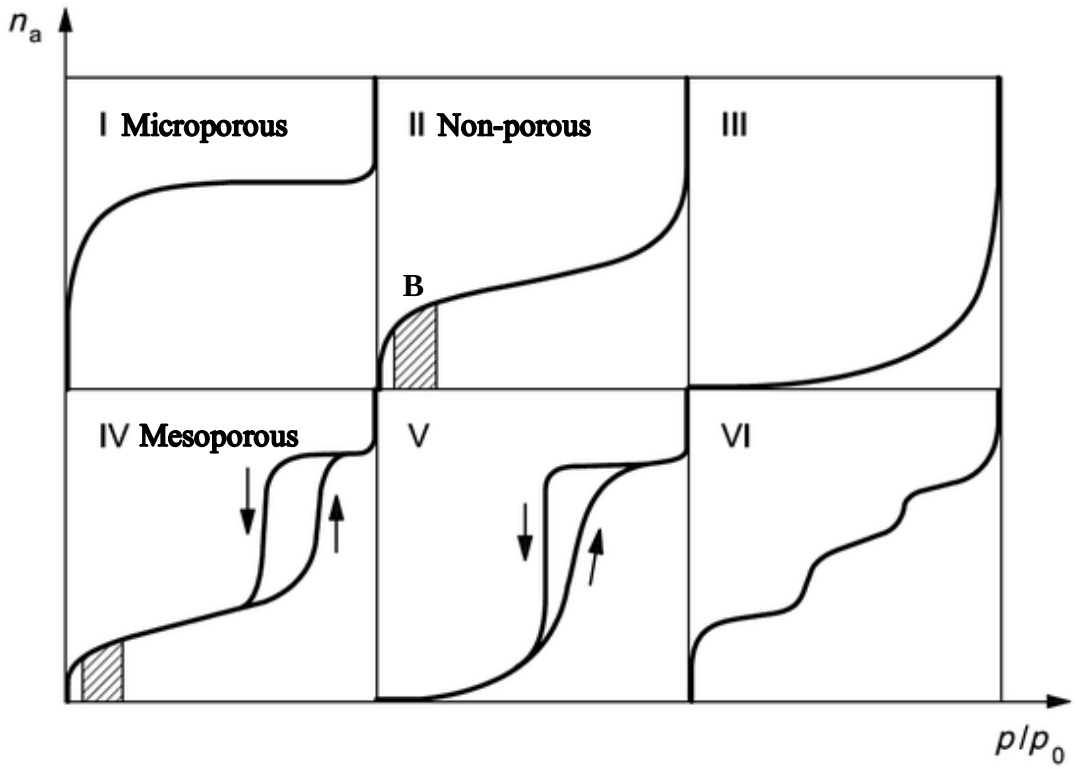

Fig. 1: Classification of adsorption isotherms (Sing et al., 1985). Type I isotherm is for microporous solids, Type II and Type III for non-porous and macroporous solids, Type IV for mesoporous solids, Type V and Type VI are characteristic curves observed in rare case (after Lowell, 2006).

2.2.3 Adsorption Hysteresis

Adsorption hysteresis takes place when there is change of isotherm profile during the adsorption and desorption process. It provides useful information about the pore shapes. Sing et al. (1985) characterized the hysteresis patterns obtained from different mesoporous shapes into four types H_1 to H_4 (see **Table 1**). In the H_1 hysteresis loop, the two branches are almost vertical and nearly parallel and are seen in porous materials with a narrow distribution of cylindrical pores. The H_2 hysteresis loop indicates presence of interconnected pores with narrow and wide pore openings. The H_3 hysteresis types are observed in materials having platy particles, which give rise to slit-shaped pores and do not exhibit any limiting adsorption at high relative pressures. In the H_4 hysteresis loop, the two branches remain horizontal and are parallel to wide range of relative pressure. This type of loop is often associated with narrow slit-shaped pores.

Several isotherms do not readily fit into any of the above classifications. These include isotherms with characteristics of more than one Type, such as the mixed Type I/IV and mixed Type II/IV. There is a special type of isotherm shape, classified as Type IIB (Rouquerol et al., 1998), which is characteristic of shales (**Fig. 2**). The adsorption branch of the isotherm has a general shape like Type II isotherms, but with a distinct H_3– type hysteresis loop. As mentioned above, hysteresis indicates the presence of mesopores. These materials are not purely mesoporous as there is no indication of the completion of mesopore filling that would result in a plateau at higher relative pressures as in a typical Type IV isotherm.

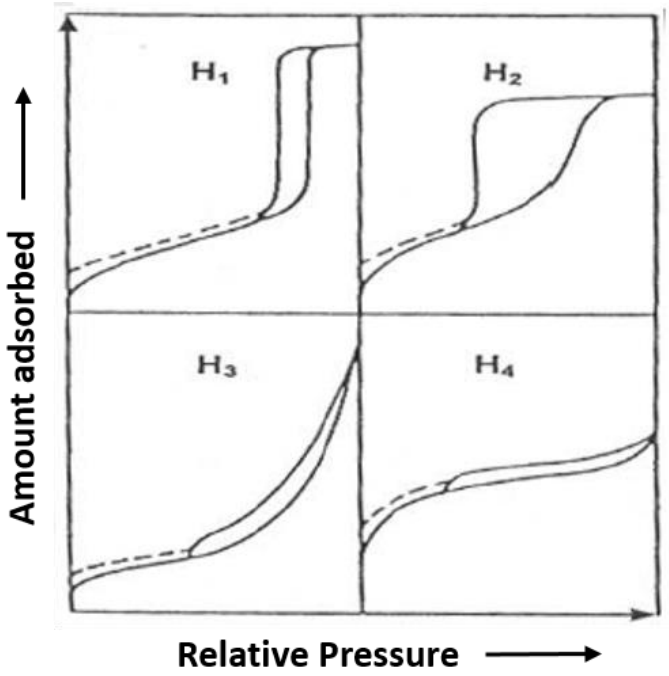

Fig. 2: The four classifications of adsorption isotherms with hysteresis loops (IUPAC, 1985). Significance of each characteristic curve is provided in Table 1.

Table 1: Hysteresis Loop Types (Condon, 2006)

Type	Characteristics	Usual Interpretation
H_1	Nearly vertical and parallel adsorption and desorption branches	Regular even pores without interconnecting channels
H_2	Sloping adsorption branch and nearly vertical desorption branch	Pores with narrow and wide sections and possible interconnecting channels
H_3	Sloping adsorption and desorption branches covering a large range of relative pressure with underlying Type II isotherm	Slit-like pores for which adsorbent-adsorbate pair yield a type II isotherm without pores
H_4	Underlying Type I isotherm with large range for the hysteresis loop	Slit-like pore for the type I adsorbent-adsorbate pair

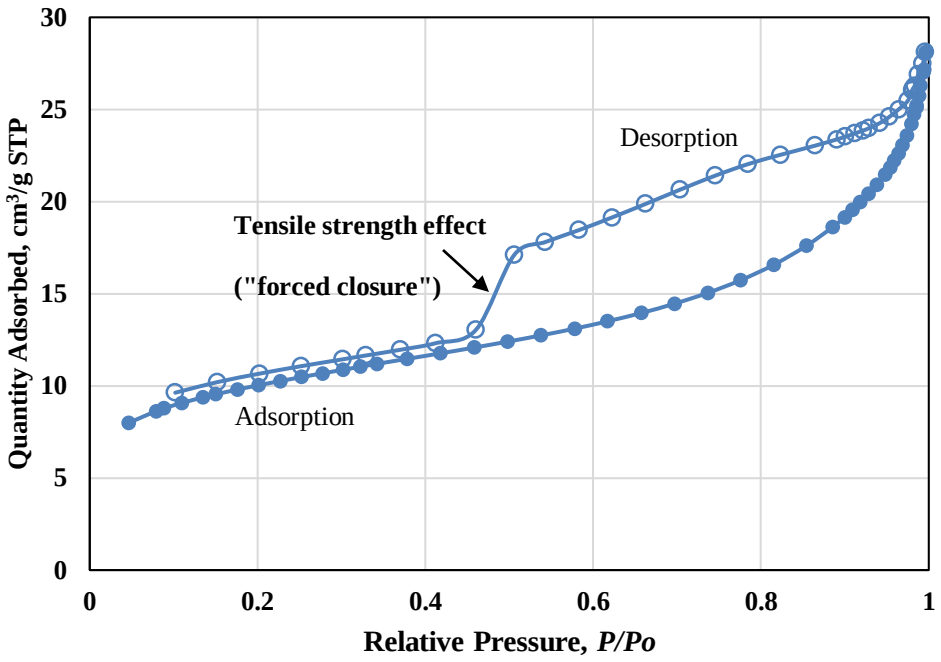

Fig. 3: N_2 adsorption isotherm at 77.36K of a Woodford shale sample. The isotherm 'forced closure' is observed in the relative pressure range 0.40-0.55 due to the *tensile strength effect*.

Another important feature observed in many hysteresis patterns is the forced closure of the desorption branch where the isotherm 'closes' at relative pressure (*P/Po*) of 0.40–0.50 for N_2 isotherms as shown in **Fig. 3**. This phenomenon is attributed to a process called the *Tensile Strength Effect* (TSE) (Gregg and Sing, 1982). Disappearance of the hysteresis is due to the instability of the hemispherical meniscus during capillary evaporation in pores with diameters smaller than approximately 4 nm (Groen et al., 2003). In these pores, the surface tension forces are stronger than the tensile strength of the liquid causing the meniscus to collapse which leads to a spontaneous evaporation of the bulk liquid phase.

Therefore, the desorption curve is not used for pore size inversion in most shales.

2.3 Adsorption Mechanism

2.3.1 BET Theory

Langmuir's monolayer adsorption study was extended by Brunauer, Emmett and Teller (1938), to multilayer adsorption (Lowell 1979). The BET theory assumes uppermost molecules in adsorbed stacks are in dynamic equilibrium with the vapor. Using Langmuir's theory as the starting point the specific surface area from BET theory can be calculated using the following equation:

$$\frac{1}{V\,[(P_o/P)-1]} = \frac{C-1}{V_m\,C}\left(\frac{P}{P_o}\right) + \frac{1}{V_m\,C} \qquad (1)$$

where,

V – volume adsorbed, cm^3/g STP

P – equilibrium adsorption pressure, mmHg

Po – saturated vapor pressure, mmHg

V_m – volume adsorbed in completed monolayer, cm^3/g STP

C – BET constant

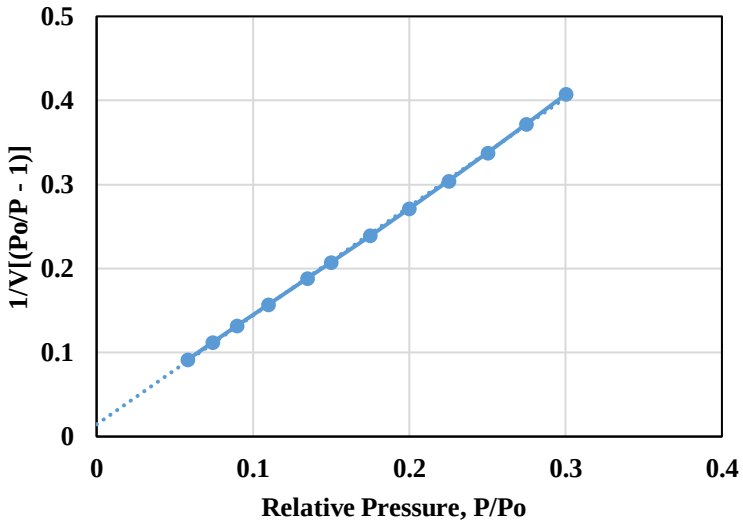

Fig. 4: Typical BET Plot (slope and intercept help determine BET constant "C" and volume of adsorbed monolayer Vm)

The slope *s* and the intercept *i* of the BET plot are,

$$s = \frac{C - 1}{V_m\, C} \tag{2}$$

and

$$i = \frac{1}{V_m\, C} \tag{3}$$

Solving equation 2 and 3, V_m and C are,

$$V_m = \frac{1}{s + i} \tag{4}$$

and

$$C = \frac{s}{i} + 1 \tag{5}$$

The total surface area can then be calculated using

$$S_t = \frac{V_m\, N_A\, A}{M} \tag{6}$$

where,

N_A – Avogadro's number (6.023×10^{23})

A – atomic surface area of N_2 at 77 K (0.162 nm^2)

M – adsorbate molecular weight (22.4)

The 'specific surface area', defined as the area of the solid surface per unit mass of material, can then be computed by dividing the total surface area by the mass of the sample.

Applications – BET theory works best for nonporous, mesoporous, and macroporous materials and is theoretically not applicable for microporous material (with pores < 2 nm) because of the occurrence of micropore filling instead of multilayer adsorption.

2.4 Micropore Volume Determination: The t-plot technique

t- plot (Lippens and de Boer, 1965) is a widely used method permitting the determination of micropore volume and the external surface area (includes surface area from mesopores and macropores). In this method, the adsorbed nitrogen volume (V_A) is plotted against the statistical thickness (t) of the adsorbed layer of N_2. The statistical thickness obtained varies with the relative pressure *(P/Po)*. The plot yields a straight line passing through the origin as shown in **Fig. 5B**, implying the sample is free of micropores. **Fig. 5B**, is considered as the standard V-t curve for a Type I isotherm and any deviation from the standard V-t curve, is considered as a non-linear region of the t- plot. t–plot of microporous material shows a straight line at medium values of t and a concave–down curve at lower values of t. Extrapolation of the linear region to the V_A axis gives the specific micropore volume and the slope of the linear fit gives the external surface area. At higher t, convex-up deviation from the linear trend indicates capillary condensation in mesopores (usually the case for all the shale samples studied in this work).

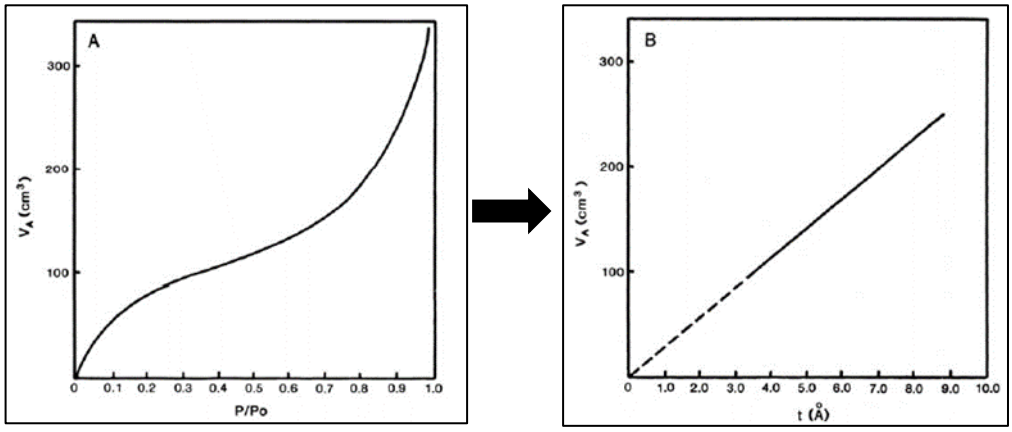

Fig. 5: V-t curve for Type I isotherm, (after Lowell et al. 2006).

In theory, the t- values were calculated using an empirical equation proposed in literature by Harkins-Jura (1944), Halsey (1948) and Lippens and de Boer (1965), and several other researchers considering N_2 adsorption at 77 K on specific type of materials.

Halsey equation

$$t = 3.54 \left[\frac{5}{\ln({}^{P_o}/_{P})}\right]^{1/3} \quad \text{Å} \tag{7}$$

de Boer's equation is expressed as

$$t = \left[\frac{13.99}{\log(Po/P) + 0.34}\right]^{1/2} \quad \text{Å} \tag{8}$$

A general form of the equation is shown below

$$t = a \left[\frac{1}{\log\left(\frac{P_o}{P}\right)}\right]^{1/b} \tag{9}$$

a = 6.053 and b = 3 when liquid N_2 is used as the adsorbate at -196°C (77.36 K).

The proposed way of computing the micropore volume and external surface area using the t- plot method is shown in **Fig. 6.** The straight line represented by (1) is indicative of a non-microporous material. For a porous material, the line will have a positive intercept as shown by (3), indicating presence of micropores, or it suggests filling of the mesopores.

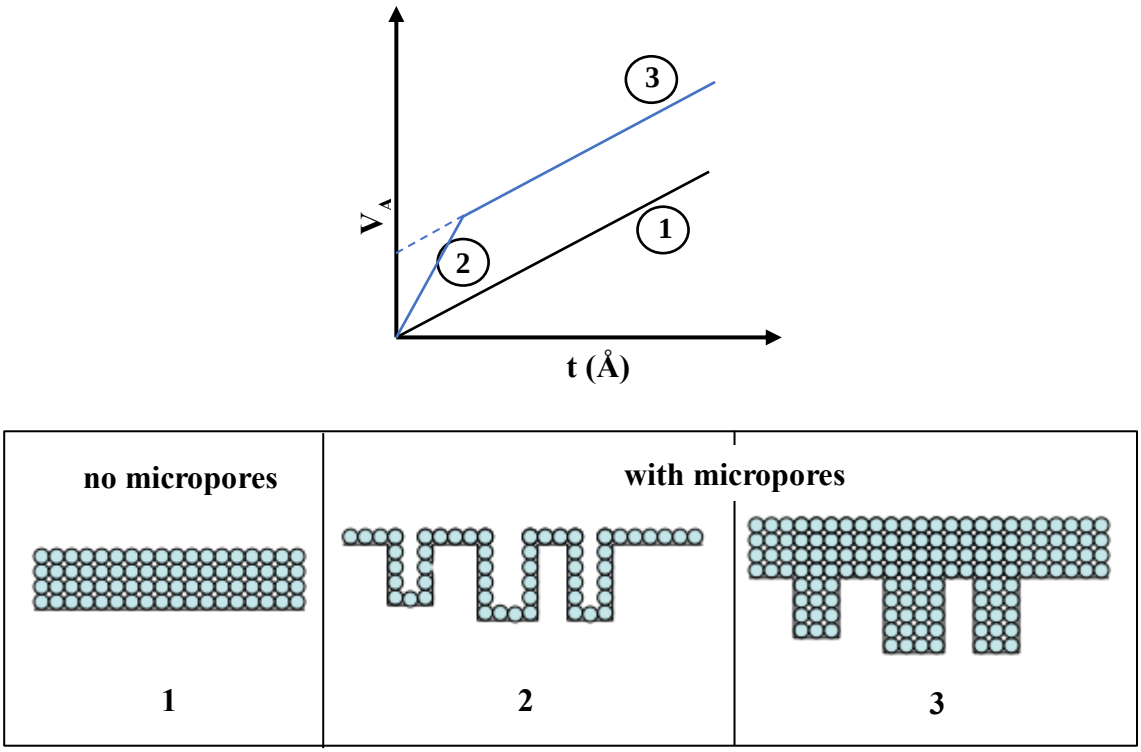

Fig. 6: An example of V-t curve for a sample showing filling of micropores. The lines in above figure correspond to the filling of micropores. (after Lowell et al. 2006)

Intercept: Volume of micropores

$$V_{MP} = i * 0.001547 \quad cm^3 \tag{10}$$

Slope: Surface area of micropores

$$S_t = s * 15.47 \quad m^2/g \tag{11}$$

The surface area of micropores (S_{mic}) can be estimated by subtracting the external surface area (S_{ext}) calculated by the t- plot methods from the total surface area (S_{BET}) obtained by the BET equation (Rouquerol et al., 2007; Webb and Orr 1997; Kuila and Prasad 2013). The following equations are used to compute the micropore surface area.

Nonporous material: $S_t = S_{BET}$

Microporous material: $S_t = S_{ext}$

$S_{micro} = S_{BET} - S_{ext}$

2.5 Mesopore Analysis

Mesopores are characterized by multilayer adsorption onto the pore walls and phenomenon of capillary condensation at high relative pressures with the formation of a curved liquid-like meniscus. Mesopore size distribution is generally computed using the Kelvin equation (eq. 12).

2.5.1 Capillary Condensation

The adsorption beyond the relative pressure range of 0.35 results in filling of the mesopores (2 to 5 nm) with the adsorbate liquid through the process of capillary condensation. The onset of hysteresis loop is an indication to the initiation of the process of capillary condensation. It is generally regarded as a secondary process, which is always preceded by adsorption of the gas on the pore walls.

Fig. 7, gives a detailed understanding about the mechanism by which capillary condensation occurs. In a confined space (capillary tube) there is higher Van der Waal's forces of attraction between each particle which implies less pressure is needed for condensation to occur. Eventually the vapor particles stick to the walls of the capillary mainly due to the adhesive forces (**Fig. 7A**). As more vapor particles enter the capillary tube the vapor particles attract to each other thus forming a multilayer adsorption (**Fig. 7B**). This process continues until a meniscus forms at the liquid vapor interface (**Fig. 7D**). During the desorption phase the pore is filled completely and the adsorbate starts to evaporate from the liquid meniscus, taking the form of hemispherical shape having some contact angle at a pressure less than the condensation pressure (**Fig. 7E**). The radius of

curvature at that point is related to the pore radius (basis for Kelvin equation). The closure of the hysteresis at lower relative pressure resembles the situation of an adsorbed multilayer film, which is in equilibrium (**Fig. 7F**).

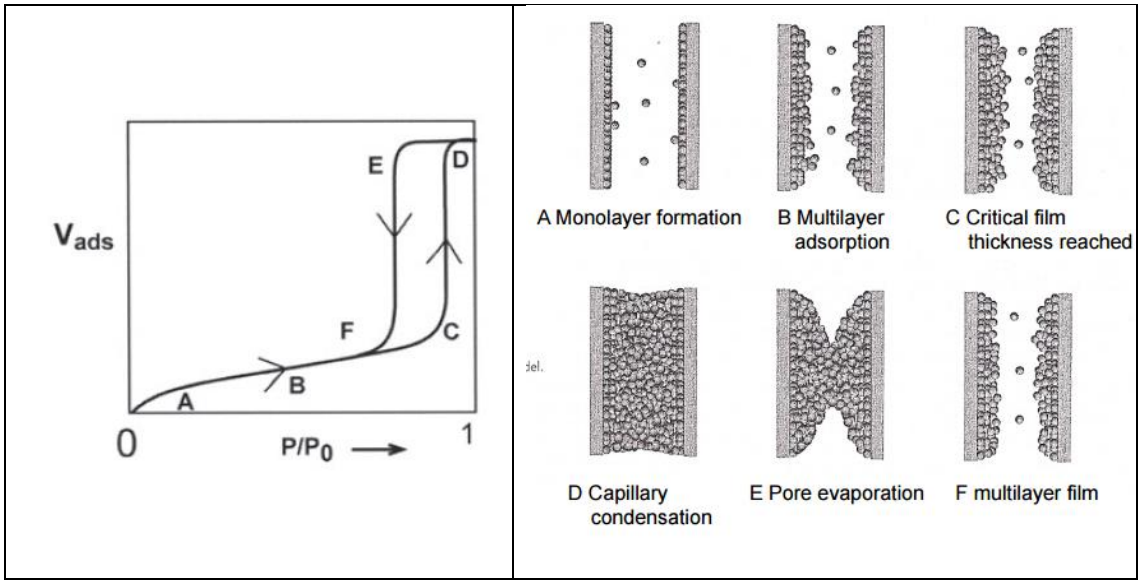

Fig. 7: Schematic representation of multilayer adsorption, pore condensation and hysteresis in a single cylindrical pore (after Lowell et al. 2006)

2.5.2 BJH Method

The Barret-Joyner-Halenda (BJH) method was developed by Barret et al. (1951) to describe the phenomenon of capillary condensation in a cylindrical pore and for calculating the PSD using the Kelvin equation. They proposed a computational method of applying the Kelvin's equation, to be able to account for the thinning of the adsorbed multilayer in the larger pores to determine the PSD from the measured adsorption isotherm data with decreasing relative pressure. The Kelvin equation (eqn. 12) gives the relationship between the relative pressure and the meniscus curvature of liquid condensed in a pore (**Fig. 7E**).

For nitrogen at the boiling temperature, the Kelvin equation is expressed as:

$$\ln \frac{P}{P_o} = \frac{-0.953}{r_m} \quad (12)$$

where,

P – actual vapor pressure, mmHg

Po – saturation vapor pressure, mmHg

r_m – mean radius of curvature the liquid meniscus, Å

Since the process of condensation is considered to occur after an adsorbed layer has formed on the pore walls, thickness of the adsorbed film is accounted for using one of the empirical equations to compute ta. For cylindrical pores,

$$r_p = r_m + t_a \quad (13)$$

where,

r_p – cylindrical pore radius, Å

t_a – thickness of the adsorbed film, Å

The curvature of the equilibrium meniscus is affected by pore geometry and hence, the Kelvin equation should be represented differently every time the meniscus changes.

Groen et al. (2003) reported that use of the desorption branch of the isotherm to obtain the PSD would limit the accessibility of pores to approximately 4 – 5 nm, due to the phenomenon of *tensile strength effect* (TSE). Instead if, the adsorption branch of the isotherm was used for obtaining the PSD, the accessibility of the pores will be 2 nm, since the Kelvin equation becomes invalid in the micropores.

2.5.3 Density Functional Theory Method

The Density Functional Theory commonly known as the DFT model is based on the principle of molecular statistical thermodynamics. The DFT model offers a practical alternative to the previously used methods, i.e. molecular dynamics and Monte Carlo simulations. Based on the microscopic properties of the system, such as fluid-fluid and fluid-solid interaction energy parameters, the pore size, the pore geometry, as a function of temperature has been modeled in the past using different molecular simulation approaches such as GCMC (Grand Canonical Monte Carlo simulation) and molecular dynamics to model the distribution of gas molecules in a system that is in equilibrium. The DFT model is a practical alternative to the above-mentioned methods since it is computationally less intensive and provides an accurate method of describing heterogeneous systems. This model results in a realistic equilibrium density distribution for the confined fluid as a function of temperature and pressure. Do and Do (2003) reported the DFT model provides a more accurate approach for pore size distribution (PSD) and can be used for pore size analysis for pores in the micro (< 2 nm) and meso (2 – 50 nm) scale.

Any porous solid material is never characterized by a single pore dimension, instead exhibits a wide distribution of pore sizes. DFT is useful in determining pore size distributions. The isotherm obtained as a result of adsorption on the pores, is assumed to be a combination of isotherm behavior in individual pores of different sizes, as shown in **Fig. 8a**. Each pore size contributes to the total isotherm. Mathematically, the relation

between the total isotherm obtained and the fraction of the total area of the sample that it represents is given by,

$$Q\ (p) = \int dH\ q(p,H)\ f(H) \qquad (14)$$

where,

$Q(p)$ – the total quantity adsorbed per unit weight at pressure p

$q\ (p, H)$ – the quantity adsorbed per unit area at pressure p in an ideal pore size H

$f(H)$ – the total area of pores of size H in the sample

Several researchers preferred using the DFT technique for inversion of the data to obtain the PSD, e.g. Adesida (2011) and Clarkson et al. (2012). The advantage of the DFT model is that it applies over the complete (*P/Po*) range of the isotherm and is not restricted to a confined range of relative pressures or pore sizes; however, it strictly applies to slit-like pores.

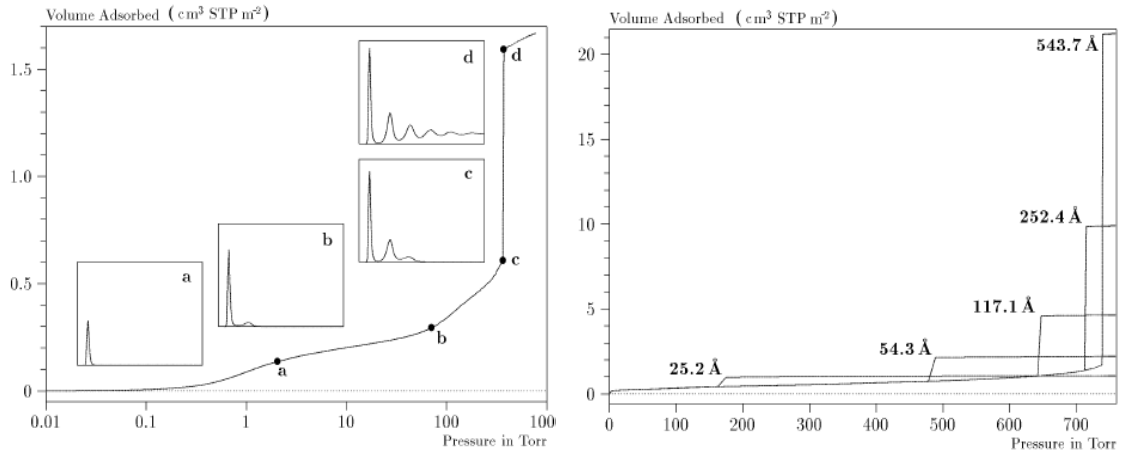

Fig. 8: (a) Model isotherm (quantity adsorbed versus pressure) for argon in a 4 nm slit pore by DFT method. (b) Collection of model isotherms with different pore sizes (H), used to obtain the pore size distribution. (images from Micromeritics software manual, 2012)

2.6 PSD Inversion Technique: BJH or DFT?

The two most common inversion techniques for PSD analysis from N_2 isotherm data include BJH and DFT techniques.

One of the key assumptions used for inverting the isotherm data to obtain PSD by BJH technique, is the thickness equation that quantifies the thickness of the adsorbed layer on the pore surface as a function of relative pressure (*P/Po*). BJH inversion of adsorption isotherm data using different thickness equations is shown in **Fig. 9.** Significant differences in the calculated differential pore volume exists for the same isotherm experiment depending on which thickness equation is used (**Fig. 9**). In each case, the dominant pore modes remain the same regardless of the thickness equation used but the differential pore volume for each pore-size differs particularly at the smaller size range. For comparative purposes the choice of any given thickness equation is immaterial as long as it is kept consistent across a sample set. Rouquerol et al. (1994) concluded that the real pore structures are much more complex than the models can account for and that the inversion is based on theoretical assumptions. The reported pore sizes are considered as cylindrical PSD.

The key assumption used for inversion in the DFT technique, is the shape of the pores is slit-type. This technique is more rigorous and has potential for applications in the study of shales, since the model calculates the specific adsorption amount in an individual pore range at a given experimental temperature and pressure by solving the function of grand

thermodynamic potential in terms of the distribution of gas density in a specific pore space (Li et al., 2016).

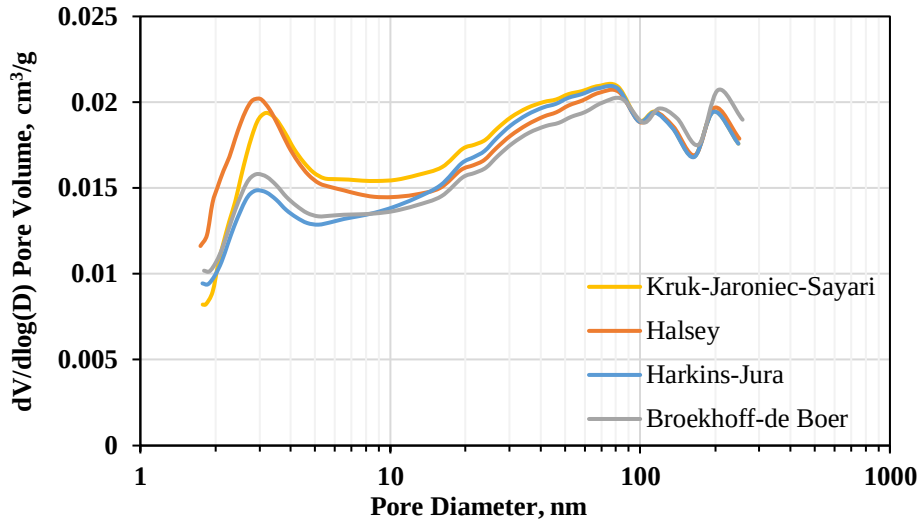

Fig. 9: PSD obtained from the inversion of N_2 gas adsorption data for a Wolfcamp shale sample from oil window using different thickness equation in the BJH method. The PSD shows similar peaks but the absolute volume differs depending on the thickness equation used.

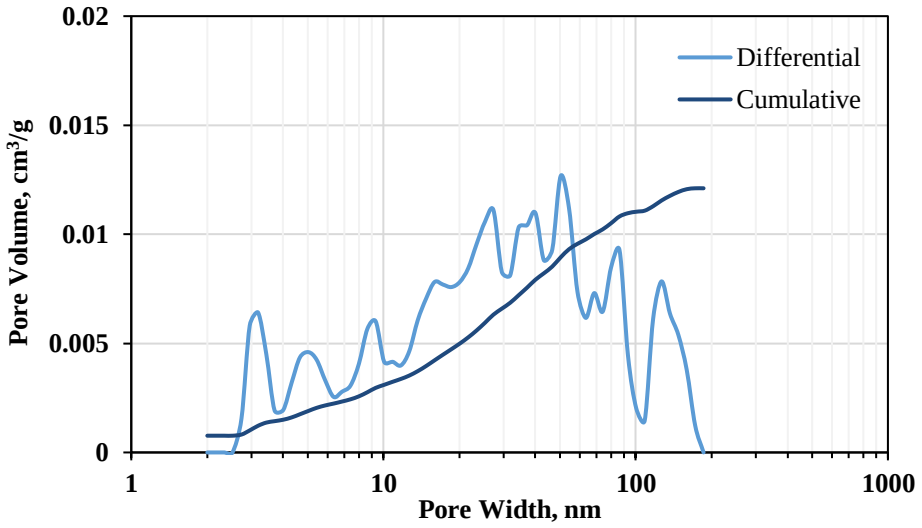

Fig. 10: An example of PSD of a Wolfcamp shale sample from oil window obtained using DFT kernels with N_2 as the adsorbate.

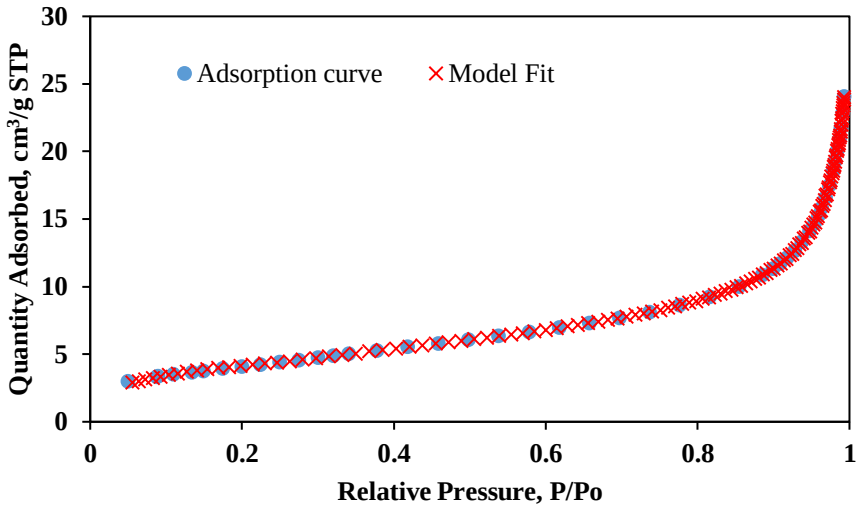

Fig. 11: The model fit to the experimental adsorption data obtained for the Wolfcamp shale sample from oil window shown in Fig. 10. The average fitting error between the experimental and theoretical isotherm for DFT analysis as shown above is less than 0.9%.

The inversion of the adsorption data from the Wolfcamp shale sample from the oil window using DFT model results in PSD as shown in **Fig. 10** and the fit for the adsorption isotherm data points is as shown in **Fig. 11.** The isotherm data fits perfectly with the model indicating lesser chances of error in the inversion of data to determine the PSD.

In this study, DFT inversion technique was used, since in most cases the wt% of minerals dominate the composition of the shale matrix over the OM content. In addition, the pore shapes associated with these minerals are mainly slit type (inferred using SEM-**Fig. 25**) and hence using the DFT inversion is appropriate in shales over other inversion models. BJH method of inversion was used for the kerogens since the SEM images confirmed that the organic pores are cylindrical in shape.

Chapter 3: Experimental Procedure

3.1 Introduction

A brief description of sample preparation and methodology adopted for solvent extraction of shale samples is explained. SEM images were used for visualizing the pore structure and for analyzing the removal of soluble hydrocarbons through pre- and post- solvent extraction imaging. Shale samples studied during the course of this work include: Lower Bakken, Wolfcamp, Woodford, Eagle Ford, Barnett, and Marcellus. In addition, two samples of kerogen from immature Green River and Kimmeridge shales were part of this study. The shale samples studied vary in maturity from immature, oil, condensate and gas window.

3.2 Experimental Workflow and Sample Description

Samples were pulverized to 35 mesh (500 µm) and oven dried at 100°C for 24 hours (Sondhi 2009) to remove any free water or volatile hydrocarbons. Thereafter, the samples were subjected to petrophysical measurements. In addition, the "as received" (native-crushed) shale samples were subjected to solvent extraction using a 4:1 mixture of toluene:methanol in a Soxhlet extractor to remove the soluble hydrocarbons. **Fig. 12** shows a flow diagram of the procedure followed in measuring the petrophysical properties.

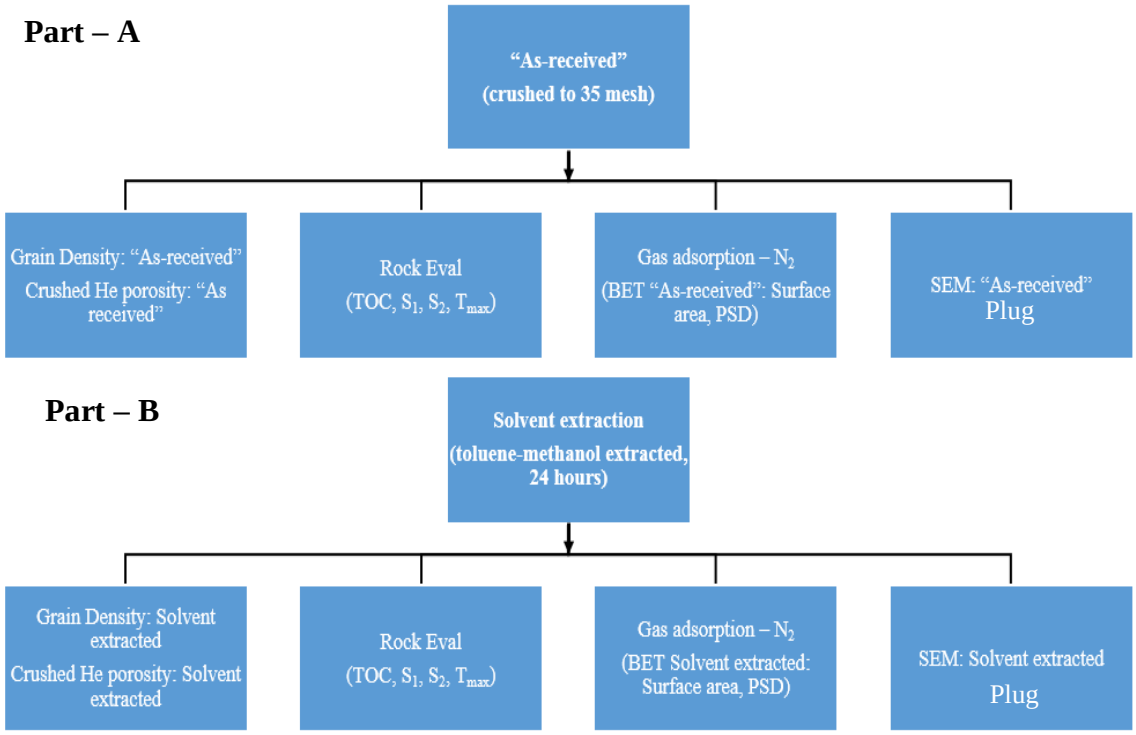

Fig. 12: Flow chart summarizing the measurement sequence and the scope of the measurements. Part A: Samples are first analyzed in the "as-received" state and then solvent extracted as shown in Part B and reanalyzed.

Petrophysical and geochemical properties of each formation are given in the **Appendix B**. In addition to the organic rich shale samples, seven – isolated kerogen sample were also studied. Durand (1980) defined kerogen as the fraction of sedimentary OM insoluble in commonly used organic solvents. The isolated kerogen ranged in maturity from immature to overmature.

3.3 Methods

A brief description of the methods for mineralogy (FTIR), TOC, SRA and SEM is given in **Appendix A**.

3.3.1 Nitrogen Adsorption

Low-pressure N_2 gas adsorption is a technique used to characterize the pore structure of shale (Ross and Bustin, 2009; Labani et al., 2013; Mastalerz et al., 2013). In this study, liquid nitrogen is used at its boiling point (77.36 K at 730 mm Hg pressure). The adsorption and desorption isotherms are obtained over a relative pressure *(P/Po)* range of 0.05 to 0.99 at a constant temperature using Micromeritics Surface Area and Porosity Analyzer instrument. The experiment is carried out by increasing the pressure up to condensation pressure (adsorption branch) followed by reduction of pressure from *Po* i.e. the saturation pressure (desorption branch). The gas adsorption isotherm is reported as the quantity of gas adsorbed as a function of relative pressure *(P/Po)*. Depending on the shape of the isotherm and the hysteresis pattern obtained the types of pores present can be qualitatively predicted based on the IUPAC classification. The details of each isotherm and its interpretation are discussed in detail in Chapter 2, **section 2.2.2**.

3.3.1.1 Set up

Micromeritics Tri-Star™ II 3020 instrument was used for adsorption study. **Fig. 13** shows the schematic of the sample tube which is placed inside the dewar containing liquid nitrogen at -196°C (77.36 K) for determining the quantity of nitrogen adsorbed. The detailed procedures are described in the **Appendix A.**

In the analysis port, at first the free space (dead volume of the tube) is volumetrically measured using helium prior to the measurement of the adsorption and desorption isotherm. The sample tube, as shown in **Fig. 13**, is kept in a liquid nitrogen dewar and dosed with a known amount of nitrogen at a series of precisely controlled pressures. The

molar quantity of nitrogen dosed to the sample is calculated from the pressure and temperature measurement, using the real gas equation of state.

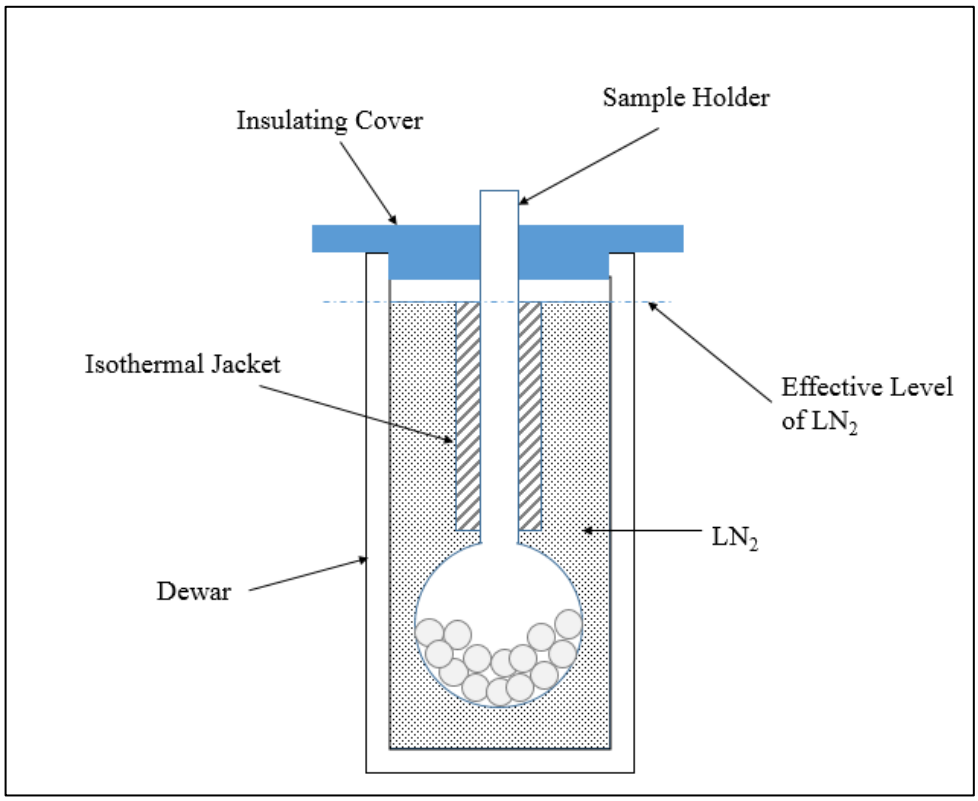

Fig. 13: Schematic of a sample tube placed in dewar containing liquid nitrogen, LN_2, at cryogenic temperature of -196°C (77.36K).

The instrument was used to measure the amount of gas adsorbed on the surface of the crushed shale samples which was then used to determine the surface area within the relative pressure range of 0.05 – 0.30 using the multi-point BET equation (Brunauer et al., 1938). The PSD was computed using the adsorption branch of the nitrogen isotherm using the DFT model for pores between 2 to 200 nm in diameter.

3.3.1.2 Calibration

Accurate calibration of the system is crucial in determining the quantity of gas dosed and subsequently the quantity adsorbed by the sample. The pressure transducers are crucial measuring devices in this setup and are calibrated using an empty sample tube to get a value of zero quantity adsorbed. The system is then checked for accuracy using a reference material, in this case carbon black. The calibrated isotherms in all three test ports are shown in **Fig. 14**. The surface area for carbon black in all the three ports were within the range of **20.6 ± 0.75 m^2/g** provided by the manufacturer.

Additionally, the system was run with pure clay minerals obtained from University of Missouri – Columbia Source Clay Minerals Repository. This was done as an additional check. The clay minerals tested are listed in Table 2. The results obtained are compared with those reported in literature.

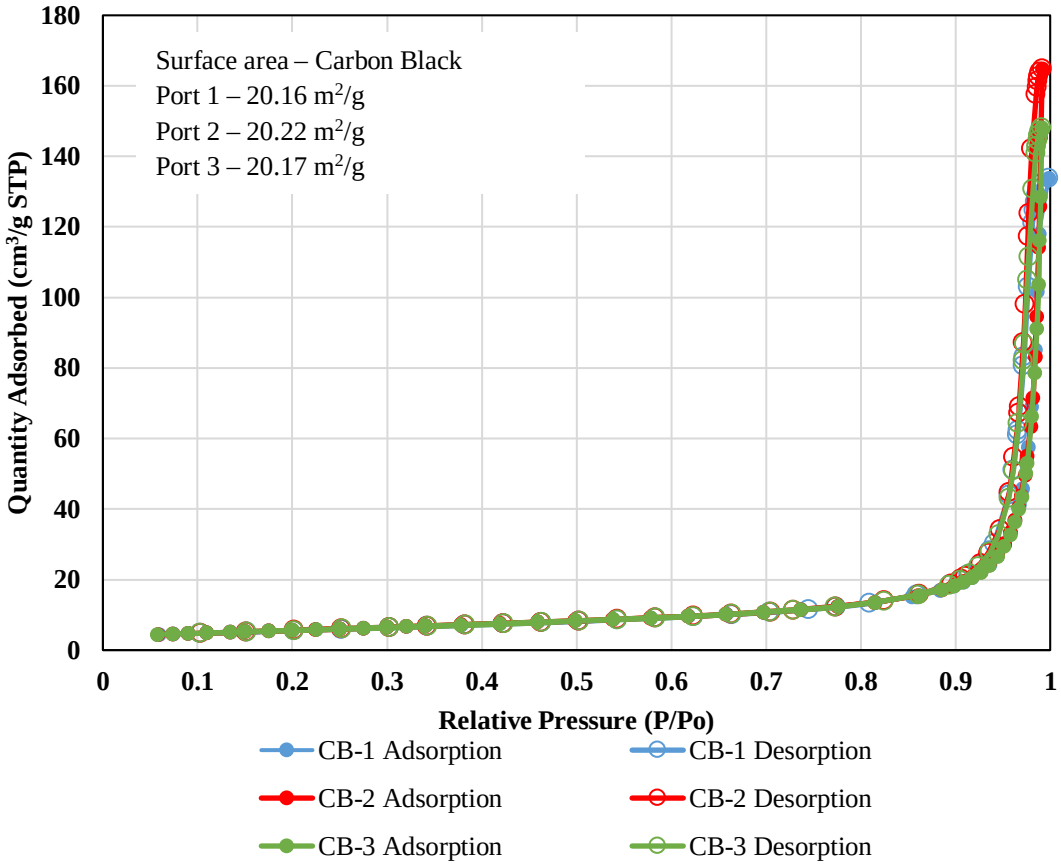

Fig. 14: Adsorption-desorption isotherms using nitrogen at 77.36 K for carbon black (standard reference) in test ports 1, 2 and 3. The isotherms do not show hysteresis confirming the carbon black sample used is non-microporous.

Table 2: List of clay minerals with its source

Clay Minerals	**Source**
Illite (IMt-1)	Cambrian Shale
Kaolinite (KGa-1b)	Warren County, Georgia
Na-Montmorillonite (SWy-2)	Gonzales County, Wyoming
Smectite	Separated by density using a proprietary gravimetric procedure developed by Statoil

Fig. 15 shows the adsorption-desorption isotherms of the clay samples. We know, that the shape of the isotherms can be used to qualitatively assess the porous structure of the materials. The isotherms of illite, montmorillonite and smectite differ from the shape of isotherm obtained for kaolinite.

Kaolinite shows an almost reversible Type II isotherm indicating absence of micro- and mesopores with macropores being dominant. The amount of gas adsorbed at low relative pressure (*P/Po* – 0.05) is very small indicating that kaolinite has negligible or non-existent micropores. On the other hand, illite, montmorillonite and smectite show a significant hysteresis pattern. As per the IUPAC classification, they show a Type IV isotherm. The distinct hysteresis patterns observed between the evaporation and condensation isotherms, suggest that capillary condensation has occurred within the mesopores (Gregg and Sing, 1982; Bustin and Clarkson, 1999). Failure to show a plateau at high relative pressure is an indication of presence of macropores in the material. These clay minerals show Type H_3 hysteresis pattern indicating the presence of slit-like pores.

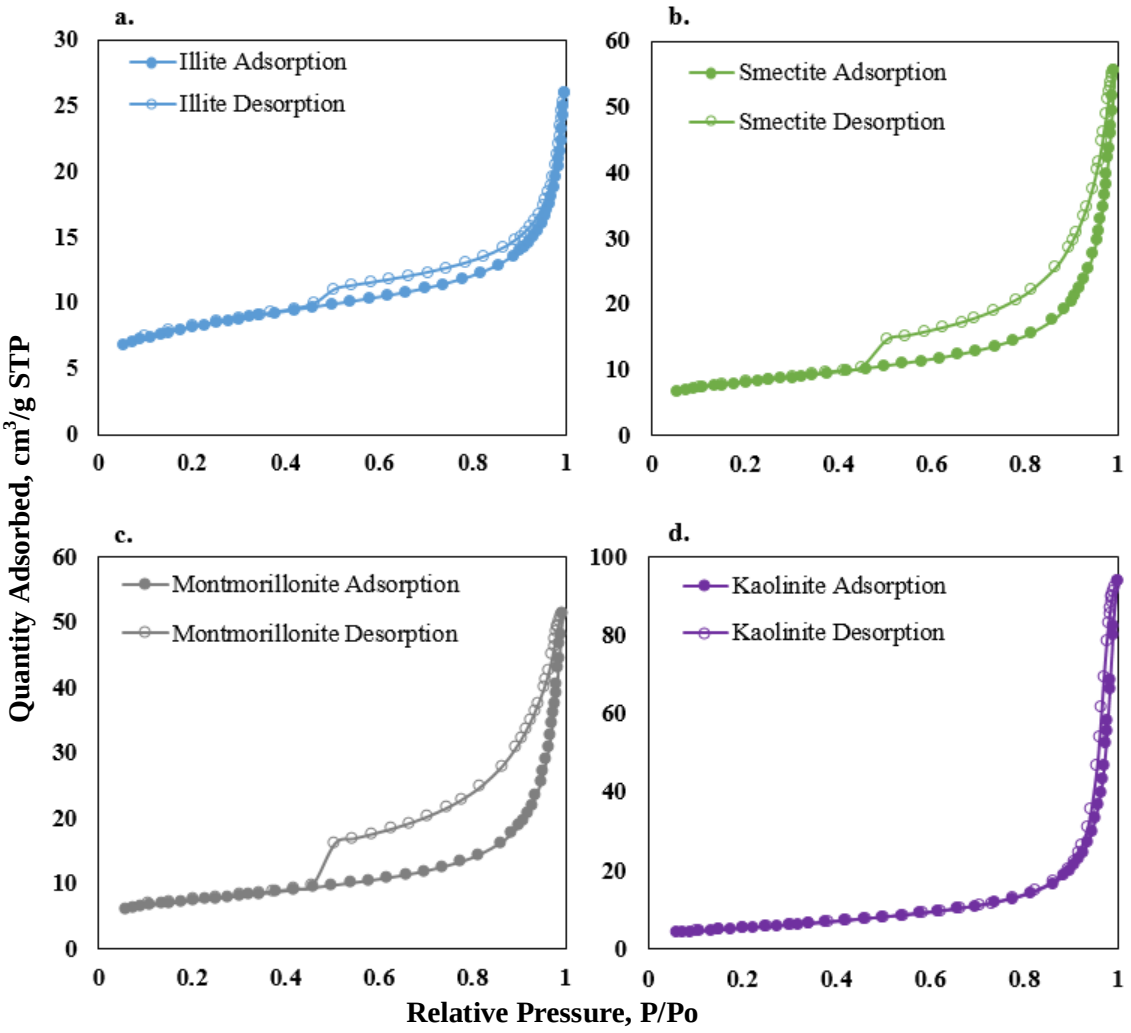

Fig. 15: Adsorption-desorption isotherms using nitrogen at -196°C (77.36K) for powders of illite, kaolinite, montmorillonite and smectite. The hysteresis effect is prominent in illite, montmorillonite and smectite and not in kaolinite. This indicates that micro-, meso- and macropores dominate in illite, montmorillonite and smectite while macropores dominate in kaolinite.

Cases et al. (1992) and Kuila and Prasad (2013) reported that micropores in smectite have slit-shaped or wedge shaped pores. The isotherms also show the 'forced closure' of the desorption branch at relative pressure of 0.45-0.5 due to the '*tensile strength effect'*. This indicates that illite, montmorillonite and smectite have significantly larger amount of small mesopores with diameter < 4 nm (Groen et al. 2003). This implies that the illite, montmorillonite and smectite have more micropores in comparison to the kaolinite.

Macht et al. (2011) studies of pure clay minerals, reported that the surface area of various pure clay minerals varies from 40 m^2/g to about 200 m^2/g depending on the particle size and the degassing temperature. The results in this study are consistently lower than those reported in literature since our degassing temperature (100°C) was lower than the values reported by other reserachers. A comparison of the lab study on the clay minerals with those reported in literature is shown in **Table 3**.

Table 3: Comparison of clay surface area from this study and literature studies based on N_2 adsorption isotherms.

Clay Minerals	N_2 S_{BET} – This study (m^2/g)	N_2 S_{BET} - Literature (m^2/g)	References
Smectite	26.8	31.1	Kuila and Prasad 2013
Illite	23.4	29.4	Ross and Bustin 2009
Na-rich Montmorillonite	24.7	30	Ross and Bustin 2009
Kaolinite	19.1	15.7 11.5 – 21.0	Liu et al., 2013 Cao et al., 2015

3.3.2 Solvent Extraction

The samples in this study were analyzed in two different states:

a. “as-received” and

b. toluene and methanol extracted.

About 10 – 12 grams of shale samples were crushed to a uniform particle size less than 35 mesh (<500 microns). The samples were thoroughly mixed. The basic petrophysical measurements included values of crush helium porosity, grain density, surface area, organic content and thermal maturity. Shale samples for solvent extraction were individually wrapped in a filter paper thimble. Based on a previous study by Gupta et al. (2017), we used a mixture of toluene and methanol in the ratio of 4:1 and heated between 65 to 75°C for a period of 24 hours to remove soluble hydrocarbons or ‘bitumen’. The samples after solvent extraction were dried in an oven for 48 hours at 100°C for evaporating any organic solvents present in the sample post extraction. Petrophysical measurements were repeated post extraction.

3.3.3 Gas Chromatography-Mass Spectroscopy

The shale samples from each well/formation were solvent extracted as described in **section 3.3.2**. The extracted filtrate or hydrocarbons after cleaning the shale samples, were concentrated using rotary evaporation and then analyzed using gas chromatography-mass spectroscopy (GC-MS). GC-MS analysis was performed using Agilent Technologies 7890B GC system. The GC oven temperature was maintained between 70°C and 300°C.

An example of the gas chromatography (GC) spectrum conducted on the extracted hydrocarbons is shown in **Fig. 16**. GC measurements provide the composition of the extracted liquid hydrocarbon phase. Liquid hydrocarbon constituents from C_{11} to C_{30+} were measured. The measured density of the soluble hydrocarbons varied from 0.71 to 0.85 g/cc. The apparent density of bitumen was calculated by volumetric averaging of elemental alkanes. The quantified density of the soluble hydrocarbons was later used to compute "extra" porosity (discussed in **section 3.3.4**), which was occupied by residual heavy hydrocarbons.

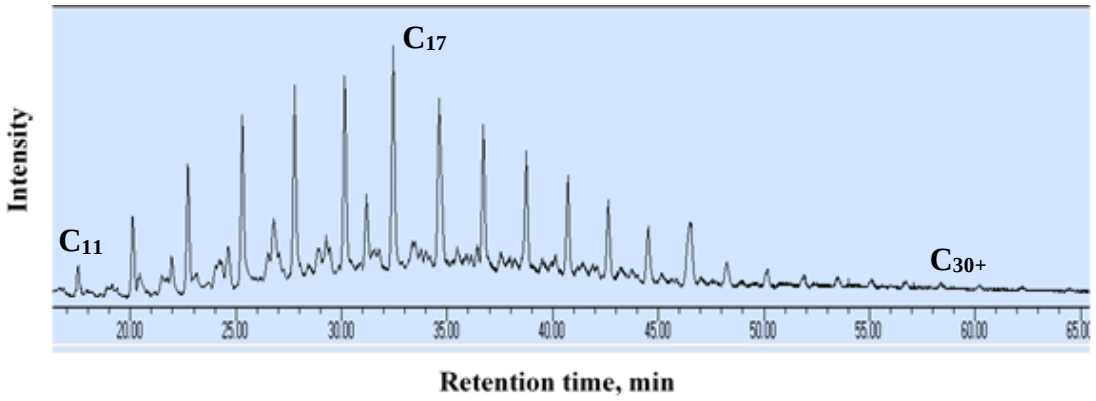

Fig. 16: An example of GC-MS spectrum used to analyze residual hydrocarbon composition. Each of the major peaks corresponds to different alkanes from C_{11}-C_{30+}.

3.3.4 Extra porosity Determination

The amount of extra porosity exposed in each sample during the process of solvent extraction was then computed using the **equation 16** (derived in **Appendix A**):

$$\emptyset_{He}^{clean} = \emptyset_{He}^{native} + \emptyset_{extra} \quad (15)$$

$$\emptyset_{extra} = \frac{\rho_g^{clean} - \rho_g^{native}}{\rho_g^{clean} - \rho_{bitumen}} (1 - \emptyset_{He}^{native}) \quad (16)$$

where,

ρ_g^{clean} – grain density of the clean sample, gm/cc

ρ_g^{native} – grain density of the native sample, gm/cc

$\rho_{bitumen}$ – density of the extracted HC obtained using mass spectroscopy, gm/cc

$\emptyset_{He}^{clean}$ – porosity of the clean sample

$\emptyset_{He}^{native}$ – porosity of the native sample

$\emptyset_{extra}$ – porosity obtained after extraction of the soluble HC's

3.3.5 Kerogen isolation

To investigate the impact of thermal maturity and different OM type on surface area measurements and to understand their dominant pore sizes, kerogen samples from different shale formations (Kimmeridge, Green River, Woodford, Marcellus) were selected for this study. Kerogen concentrates of the bulk were prepared by means of conventional demineralization method by a commercial lab. A detailed procedure is discussed in the **Section 6, Appendix A**.

Chapter 4: Results and Discussions

A total of 94 samples were studied: 27 samples from Wolfcamp, 8 samples from Barnett, 16 samples from Lower Bakken, 8 samples from Woodford, 4 samples from Marcellus, 23 samples from Eagle Ford and 8 from Vaca Muerta. Petrophysical measurements were carried out on all the samples in their "as-received" and after solvent extracted state. The shale samples were analyzed to examine the relationship between nitrogen gas adsorption capacity, TOC content, kerogen type, thermal maturity, mineral compositions and pore size distribution (PSD).

4.1 Sample Mineralogy

Mineralogy of all the samples was determined using transmission FTIR. The average mineralogy for the shale formations is presented in the **Fig. 17**. Lower Bakken, Wolfcamp, Woodford and Marcellus samples are rich in clay (average of greater than 40 wt.%). Eagle Ford samples are rich in carbonates with calcite being the dominant carbonate mineral (greater than 70 wt%). All the shales had clays present with illite being the dominant clay. No significant amount of smectite was present in the samples studied.

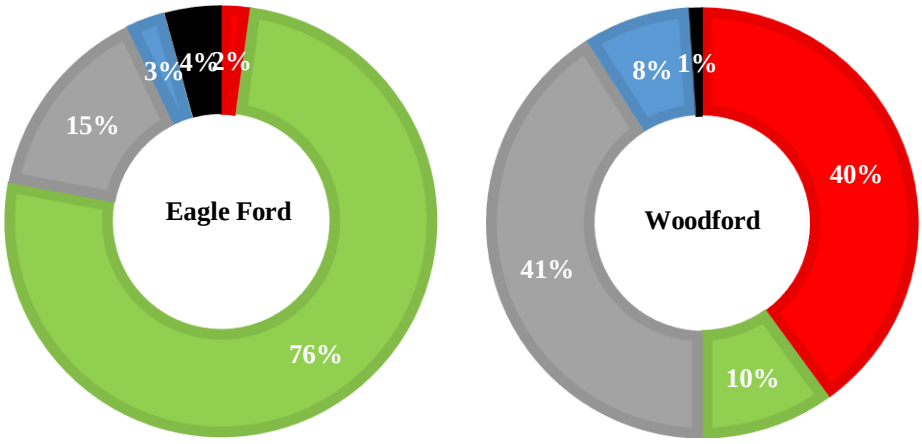

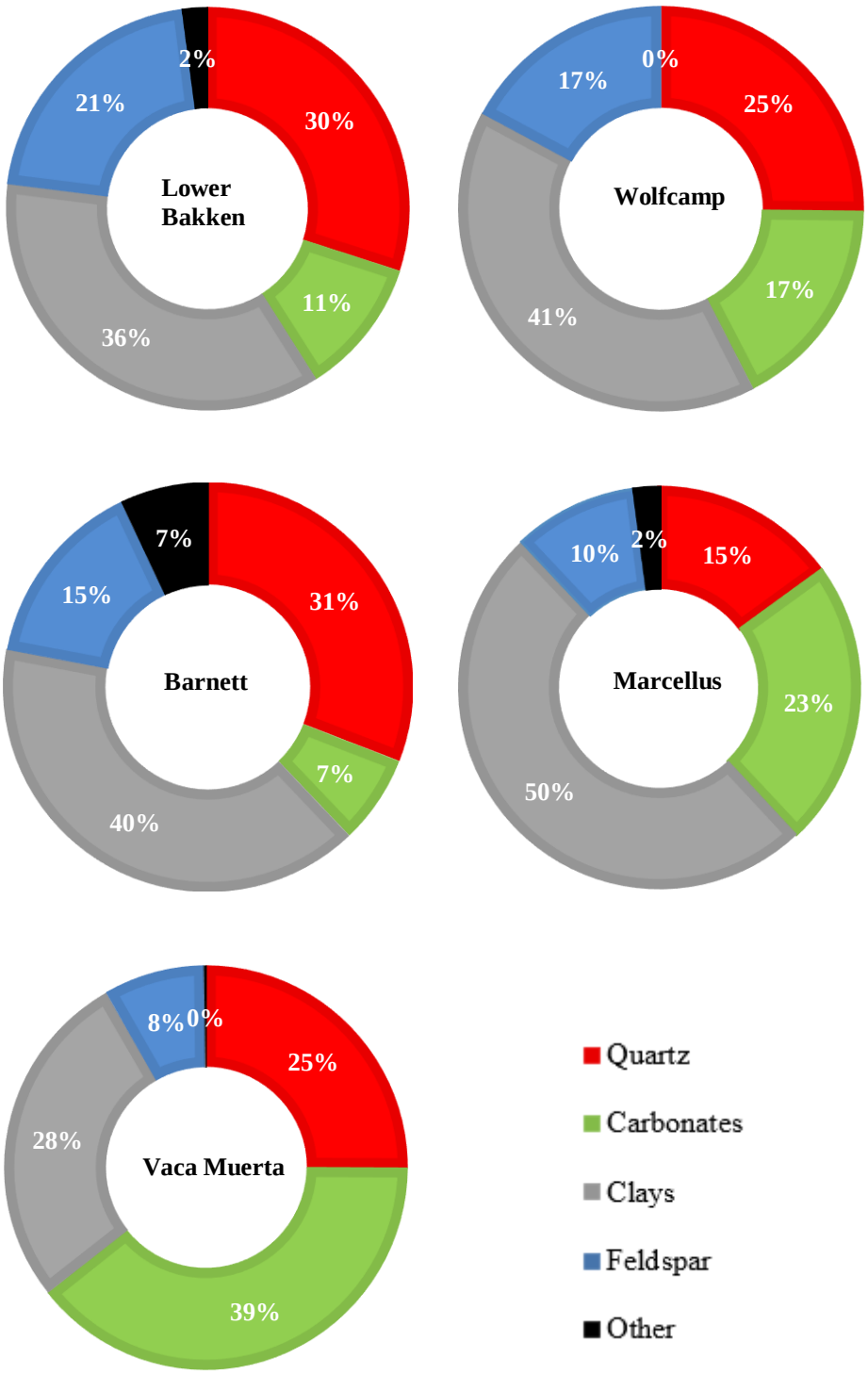

Fig. 17: Average FTIR mineralogy of the shales presented in this study

4.2 Total Organic Carbon

The TOC values for the "as-received" samples from the immature window range from as low as 0.7 wt% to as high as 16 wt% (**Fig. 18** – immature: patterned bars). The average TOC values for each of the maturity window in their "as-received" state are immature 8.6 wt%, oil 5.8 wt%, condensate 4.9 wt%, gas 4.9 wt%.

Fig. 18 represents a box and whisker plot for measured TOC values for all the shale samples pre- and post- solvent extraction from varying maturity windows. The patterned bars represent TOC values in the as-received state whereas the filled bars represent the TOC values post extraction. The cross marks within the box plots represent the average values for each case and the horizontal black line represents the median of the dataset. Post extraction the TOC value reduces the maximum in the oil window and least in the gas window. N indicates the number of samples in each maturity window. Individual value of TOC for each sample are reported in **Appendix B**.

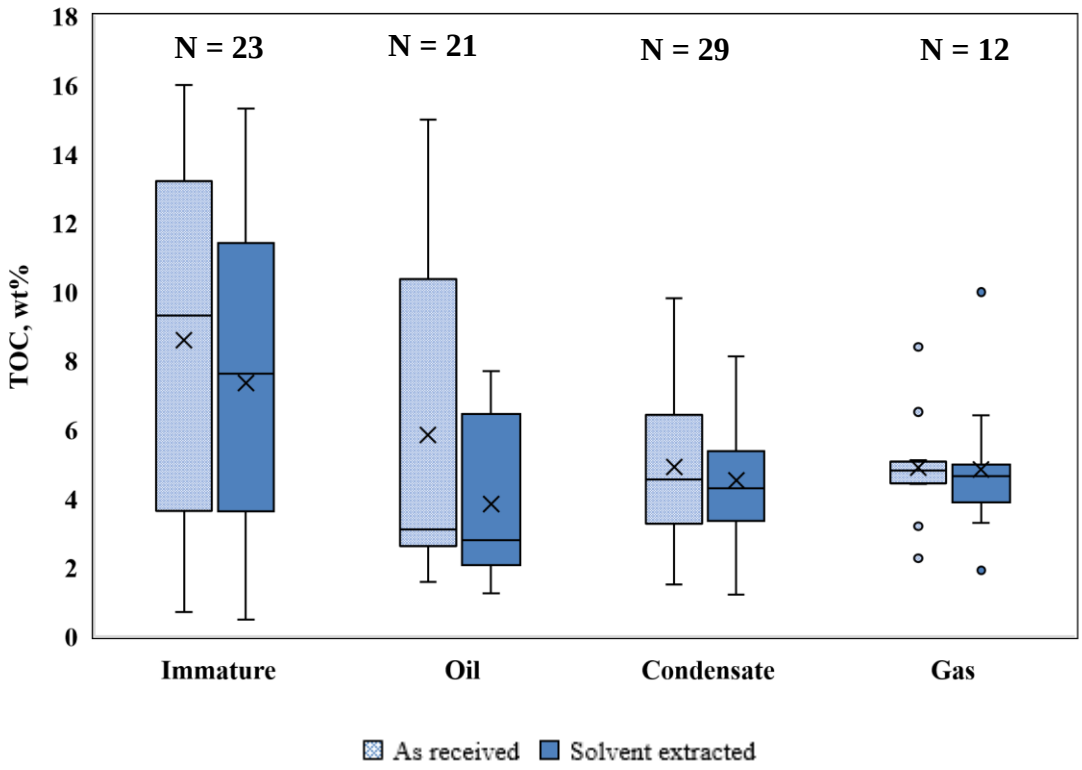

Fig. 18: Box and whisker plot of TOC measured in different shale formations plotted based on their maturities. The cross marks in each bar represents the average TOC value.The average TOC values for immature, oil, condensate and gas in their as-received state are 8.6, 5.8, 4.9, 4.9 wt% respectively. The TOC value reduces post extraction showing maximum reduction in the oil window and least in the gas window. N indicates the number of samples in each maturity window.

4.3 Source Rock Analysis

The pyrolysis flame ionization detector was used to detect the S_1 and S_2 peaks to identify the hydrocarbon components liberated at varying temperatures. The S_1 fraction contains most of the residual light hydrocarbons and condensate trapped within the pore spaces of the rock. McCarthy et al. (2011) states that majority of the S_2 peak comes from kerogen and is thus immovable. **Fig. 19** and **Fig. 20** represents the SRA S_1 and S_2 values pre- and post-extraction respectively in the form of a box and whisker plot. The S_1 value decreases considerably post extraction in immature, oil and condensate window implying the removal of the producible liquid hydrocarbons by dissolution in the organic solvents. In case of the gas window there is negligible S_1 indicating all the producible liquid hydrocarbon has been converted to gas.

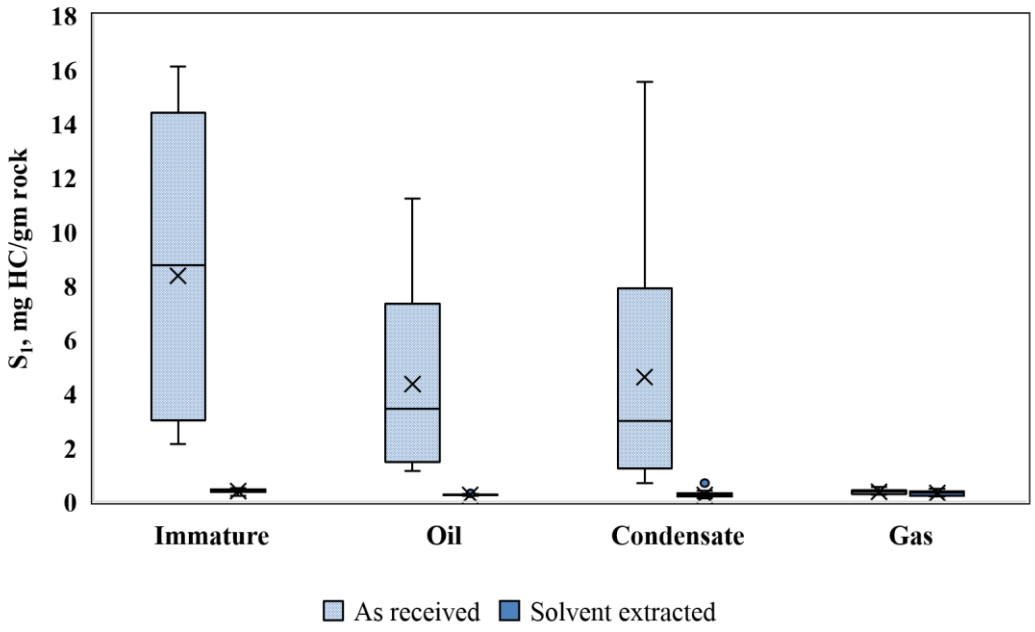

Fig. 19: Box and whisker plot of SRA S_1 peak values pre- and post-extraction for shale samples from different maturity windows. The change in S_1 peak post-extraction is significant indicating the removal of producible liquid hydrocarbons and a part of bitumen that are generated below 300°C. Gas shale samples do not show any S_1 peak affirming the conversion of the hydrocarbons to the gas.

Fig. 20 shows the change in S_2 values for different maturity windows. S_2 represents the fraction of hydrocarbons that are generated above 300°C. It is observed that the change in S_2 value is minor in comparison to the significant change seen in the S_1 values post-extraction. The minor change observed in S_2 value is likely due to the dissolution of the bitumen since the majority of kerogen which contributes to the S_2 value is insoluble in the organic solvents.

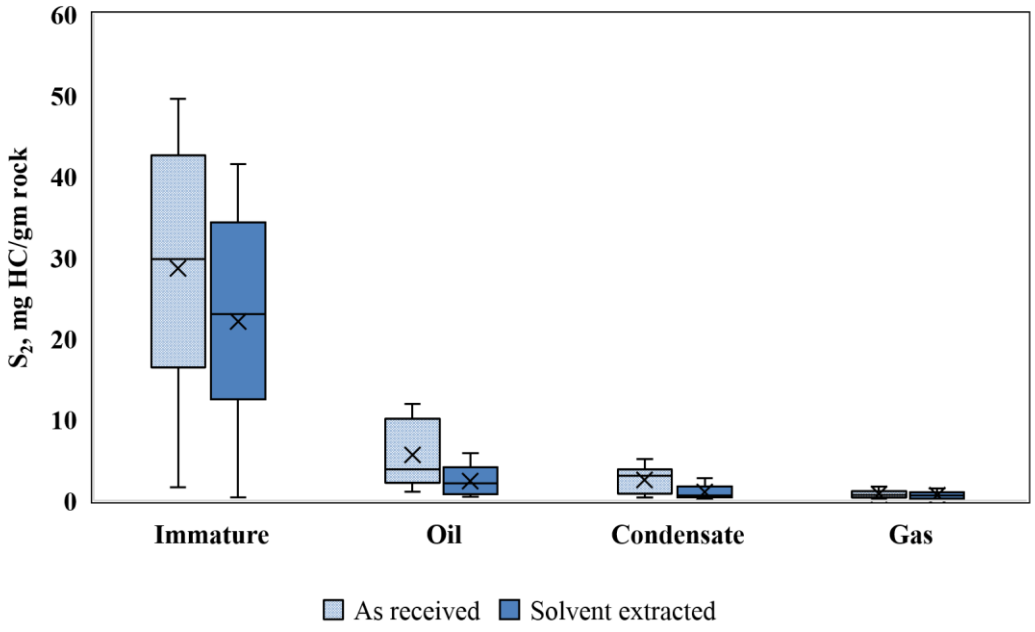

Fig. 20: Box and whisker plot of SRA S_2 values pre- and post-extraction for shale samples from different maturity windows. The change in S_2 peak post-extraction is minor in comparison to the S1 peak. Similar to the S_1 peak the samples from the gas maturity window do not show significant presence of S_2 peak.

4.4 Crushed Helium Porosity and Extra Porosity as a function of Maturity

The effective porosity of the samples was obtained using Karastathis (2007) method. The porosity for the "as-received" state of samples ranges between 1.65% to 12.55%. The average porosity values for each of the maturity studied are 3.74% (immature), 6.19% (oil), 7.85% (condensate), and 7.2% (gas). The porosity measurements were repeated after samples were Soxhlet extracted using toluene and methanol (4:1). Post extraction there was a certain coloration of the organic solvents suggesting removal of mobile hydrocarbons. The bitumen density was computed using GC-MS spectra for each well after the extracted fluids were concentrated and then using **equations 15 and 16** described in section 3.3.4, the increase in porosity was computed.

A comparison of the "as-received" and solvent extracted porosities is shown in **Fig. 21** in the form of box and whisker plot. The cross marks in the center of the bars indicate the average value for each case. Crushed rock helium porosities measured pre- and post-solvent extraction shows a general increase in porosity. Post extraction the average porosities in each maturity window increase from 3.7% to 7.2% for immature, 6.2% to 8.6% for oil, 7.9% to 9.3% for condensate and 7.2 to 7.9% for gas window. This increase implies, that the occupancy and blockage of pore spaces in shales by bitumen and mobile oil significantly affects the porosity measurements. The average percentage increase in porosity is in the following order: immature (93%) > oil (39%), condenste (19%) > gas (10%).

The increase in porosity can be attributed to the removal of soluble hydrocarbons and solid bitumen from the pore system (either coating on the grains or from the pore network of the samples) using organic solvents. To identify as to where the soluble HC's are being removed from, the PSD analysis for pre- and post- solvent extraction was done, results are shown in **Section 4.6.2**. In addition, the SEM images (discussed in detail in Section 4.5) were used as a visual aid to quantify the removal of soluble hydrocarbons during Soxhlet extraction in each maturity window and visually identify the removal of HC coating on the grains.

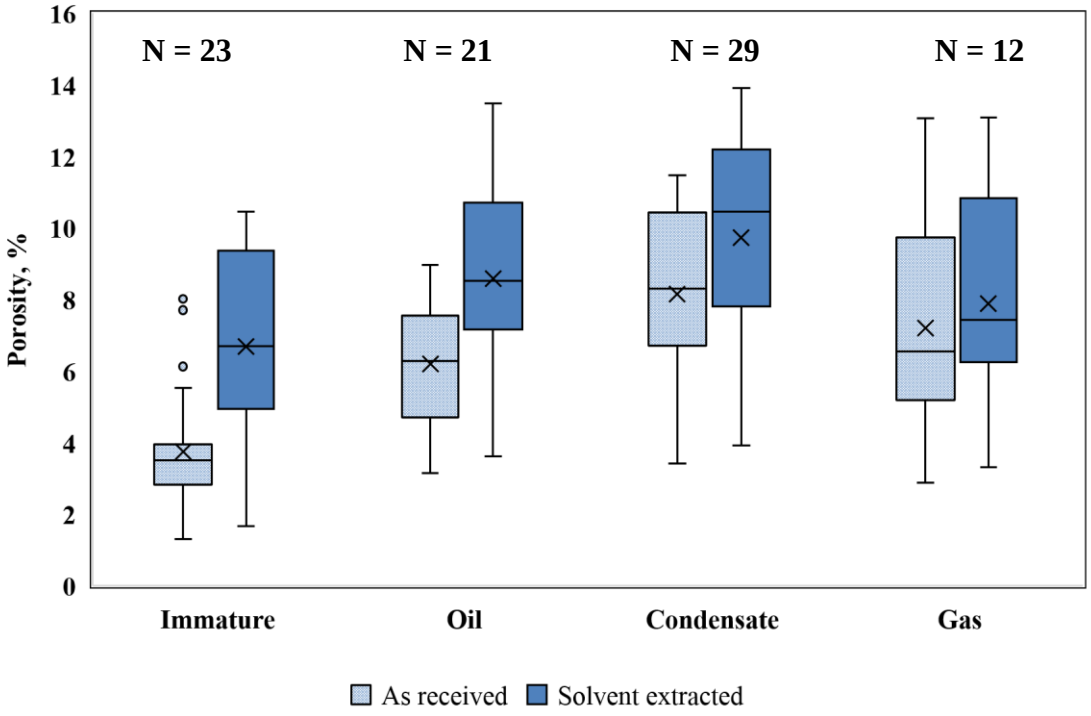

Fig. 21: Box and whisker plot of crushed helium porosity for different maturity shales pre- and post- solvent extraction. The cross marks in each histogram represents the average porosities in each case. The average percentage increase in porosity for immature, oil, condensate, and gas window are 93%, 39%, 19% and 10%, respectively. The increase in porosity post-extraction is high in the liquid rich shales implying the presence of soluble HC's leading to an underestimation of the effective porosity of the shales in the "as-received" state. N indicates the number of samples in each maturity window.

The next step of this study, was to correlate the increased porosity, referred to as the "extra-porosity" with organic content for different thermal maturity windows (**Fig. 22**).

We observe a good correlation for the samples in the immature and the oil window. This implies that the impact of Soxhlet solvent extraction is good in immature and oil window removing the soluble (mobile) hydrocarbons. In case of the gas window there is a weak negative correlation, suggesting absence of the mobile hydrocarbons.

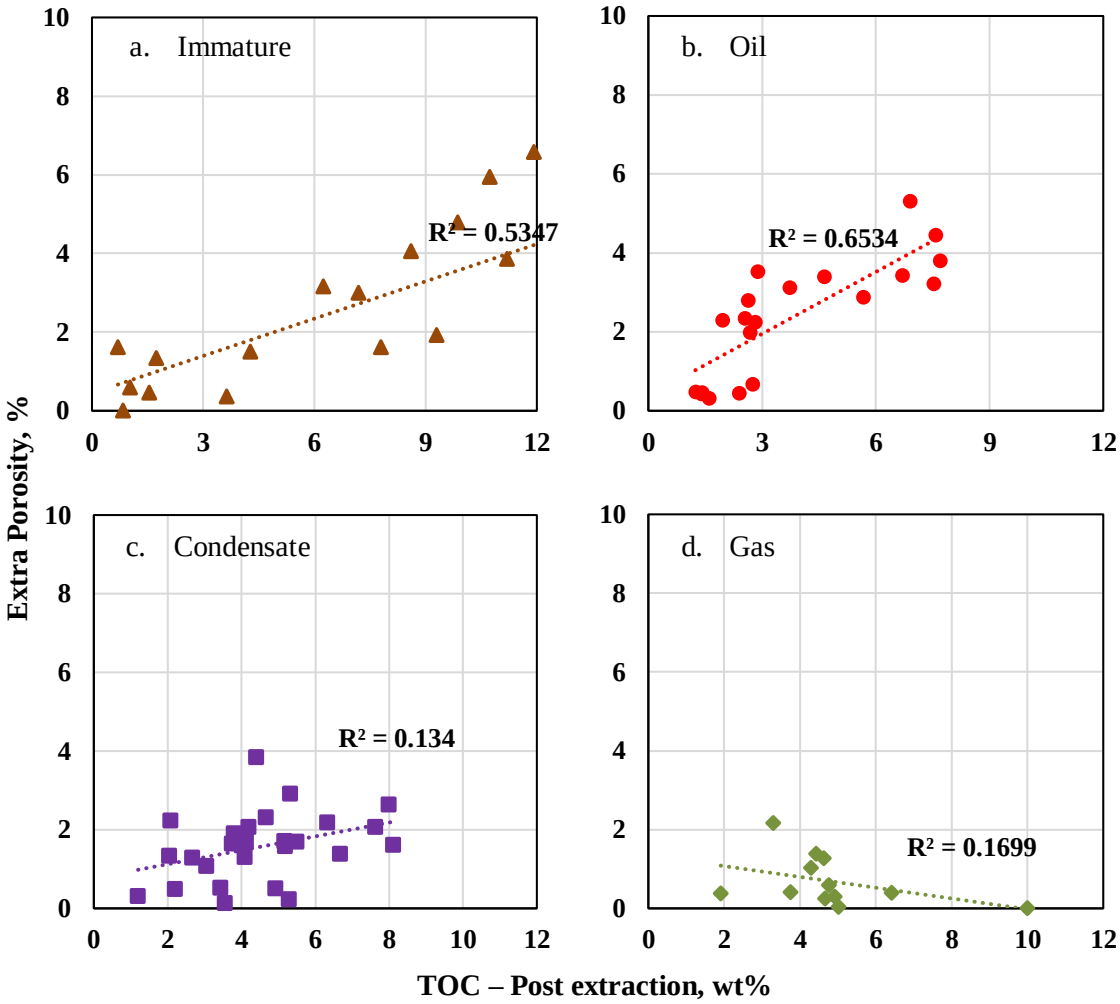

Fig. 22: Relationship between extra porosity and TOC – post extraction, wt% for different thermal maturity window. The strongest correlation coefficients are obtained with the immature and oil window.

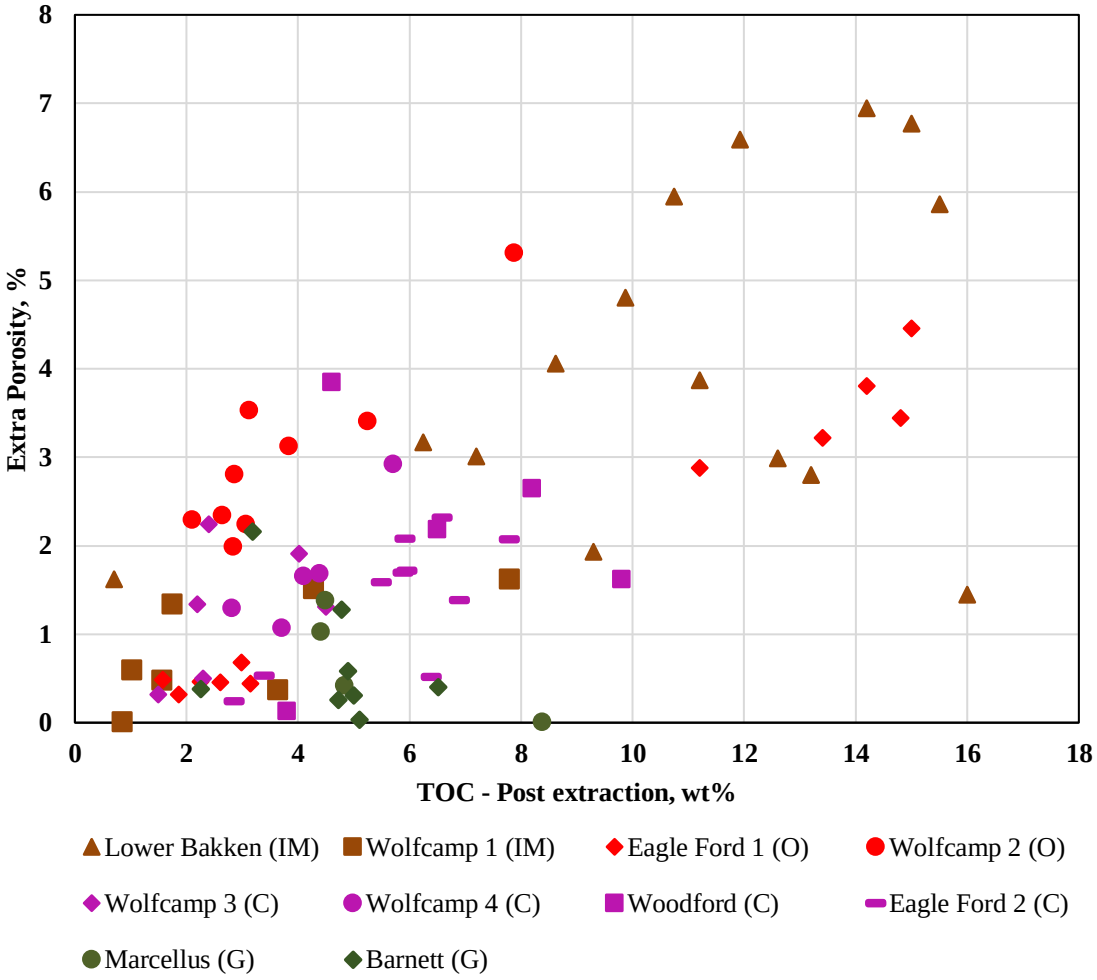

Fig. 23: Relationship between extra porosity with TOC, wt.%. The extra porosity was obtained due to removal of soluble hydrocarbons during Soxhlet extraction.

Fig. 23 is a combination of all the samples from each maturity window shown in **Fig. 22** to have a broader look at all the formations and maturity together. The results indicate a positive linear correlation between the two parameters, i.e., "extra" porosity and TOC. The maximum amount of extra porosity was found in the Lower Bakken formation, which belongs to the immature window. A unique trend is observed in each well which can be attributed to the maturity, clay and organic content.

4.5 SEM

Figs. 24, 25 and 27 show SEM images of Bakken, Eagle Ford and Marcellus samples from the immature, oil and gas maturity window, respectively, pre and post solvent extraction. These samples were selected based on their TOC and clay contents.

The Bakken sample has high clay (57 wt.%) and organic content (13.2 wt.%). **Fig. 24** shows the SEM pre and post solvent extraction. The image shows extremely high organic content with very little organic pore development. This is consistent with the measured surface area for the "as-received" state which was only 2.74 m^2/g. The image shows a clear boundary between the organics and the minerals separated by fractures.

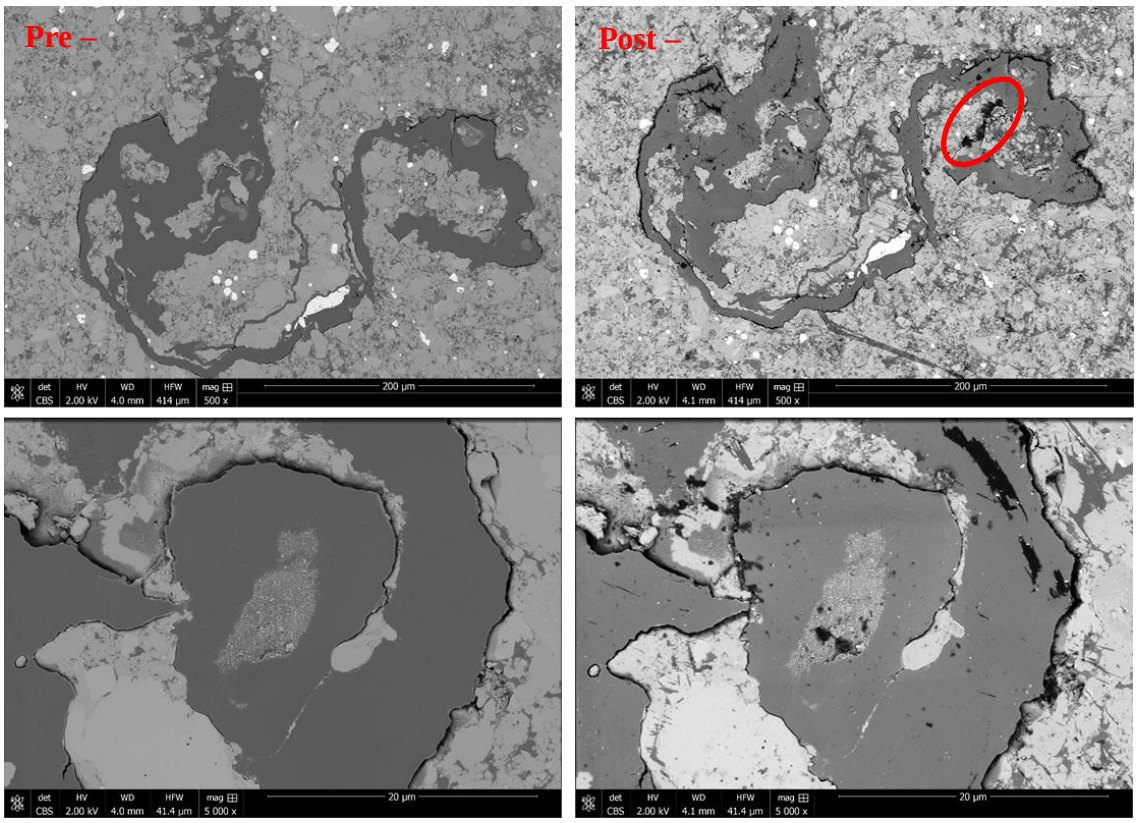

Fig. 24: SEM images of the immature shale from the Lower Bakken formation (clay – 57 wt%, TOC – 13.2 wt%,) showing the cracks and poorly developed organic matter pores. The image shows removal of some soluble HC post extraction.

The Eagle Ford sample from the late oil window shows the presence of small pores hosted inside the organic pores. After solvent extraction more pores are exposed. It is clear from these images that the pore sizes increase with the removal of bitumen and soluble hydrocarbons are removed. The images on the right show exposure of the previously coated clays and organics "post extraction". These clays and organics contribute to the increase in porosity and surface area, that we observe as a function of solvent extraction mainly in the oil and the condensate window.

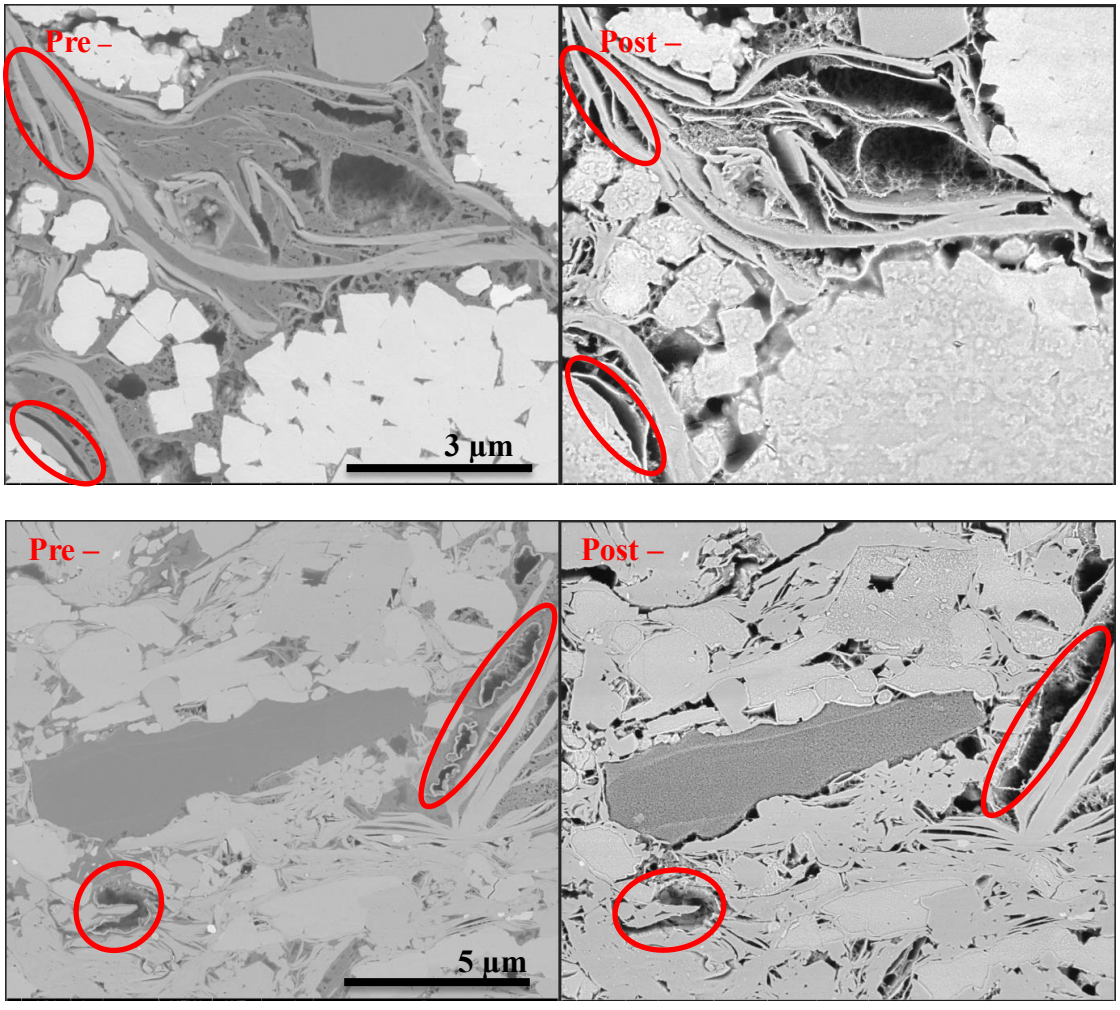

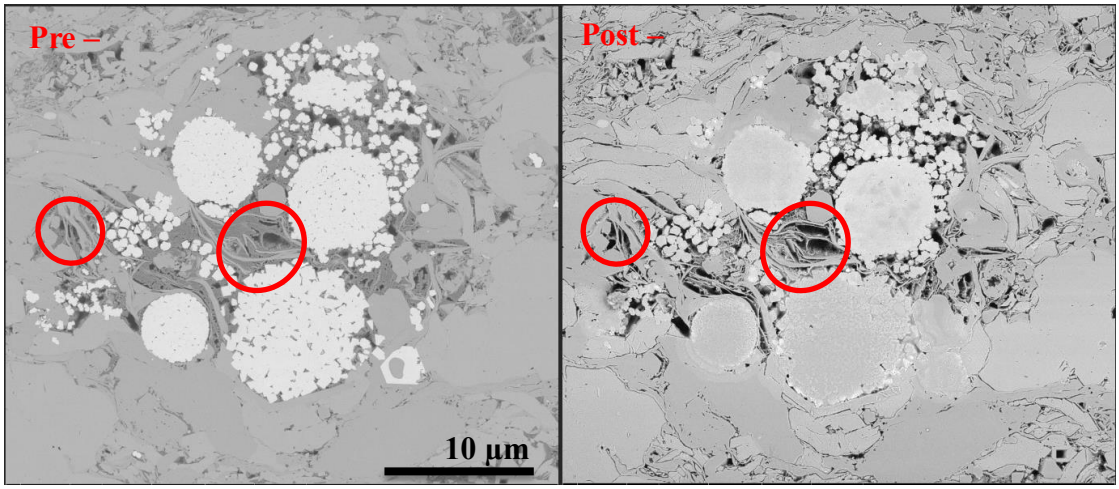

Fig. 25: Alteration in organic microstructure before and after solvent extraction in Eagle Ford - late oil window (clay – 14.3 wt% and TOC – 5.2 wt%) sample qualitatively providing information about the location of the pores throughout the sample. In each case, the size of the pores within the organics increases upon solvent extraction.

The above image shows how the bitumen occupies the pore and hinders the pore connectivity and inhibits the exposure to the organics which are the main contributors to the surface area.

Loucks et al. (2009) reported that the shale reservoirs host abundant pores in OM. In the gas window, Curtis et al. (2012) observed more porosity in the organic matter as the maturity increases. The general explanation given by Curtis et al. (2012) is that the generation of hydrocarbons by cracking of the kerogen will produce porosity in the organic matter. Valenza et al., (2013) observed an increase of the specific surface of the organic matter from 50 m^2/g on immature samples to 400-600 m^2/g on post mature samples. This is consistent with the development of porosity as a function of maturity. However, the weakness of the trend observed by Curtis et al., (2012) suggests that the

origin of the organic matter could play an important role on the generation of organic porosity or possibly the inadequacy of the Ro (%) measurements.

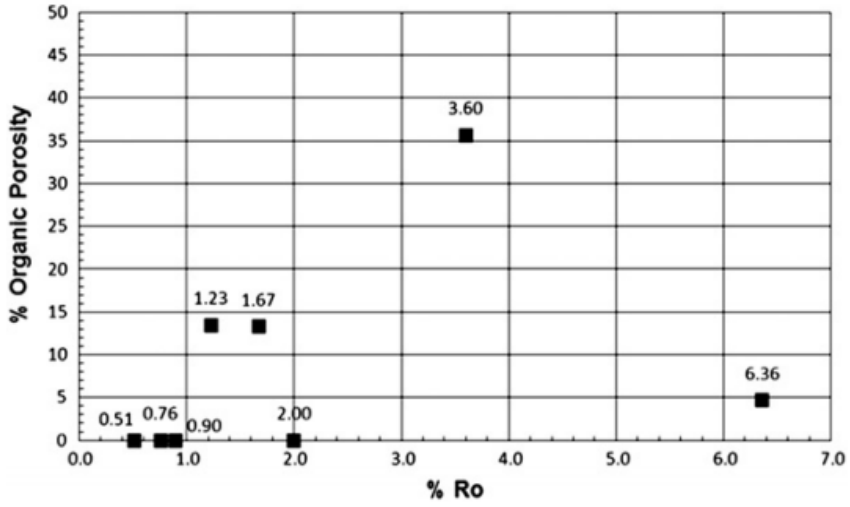

Fig. 26: Organic porosity as a function of thermal maturity (Curtis et al. 2012). A weak positive correlation can be observed. This implies thermal maturity is a contributing factor but not the sole factor controlling adsorption.

Based on the above explanations and studies we find the SEM images for the Marcellus sample show ample numbers of smaller organic pores. This accounts for the high surface area (41.53 m^2/g) obtained in the "as-received" sample. In addition, if we closely examine the images pre and post extraction, we do not see any change in the size of the pores or any visual change in the microstructure implying all the bitumen has been converted to gas during maturation. The numerous organic pores are a result of cracking of kerogen.

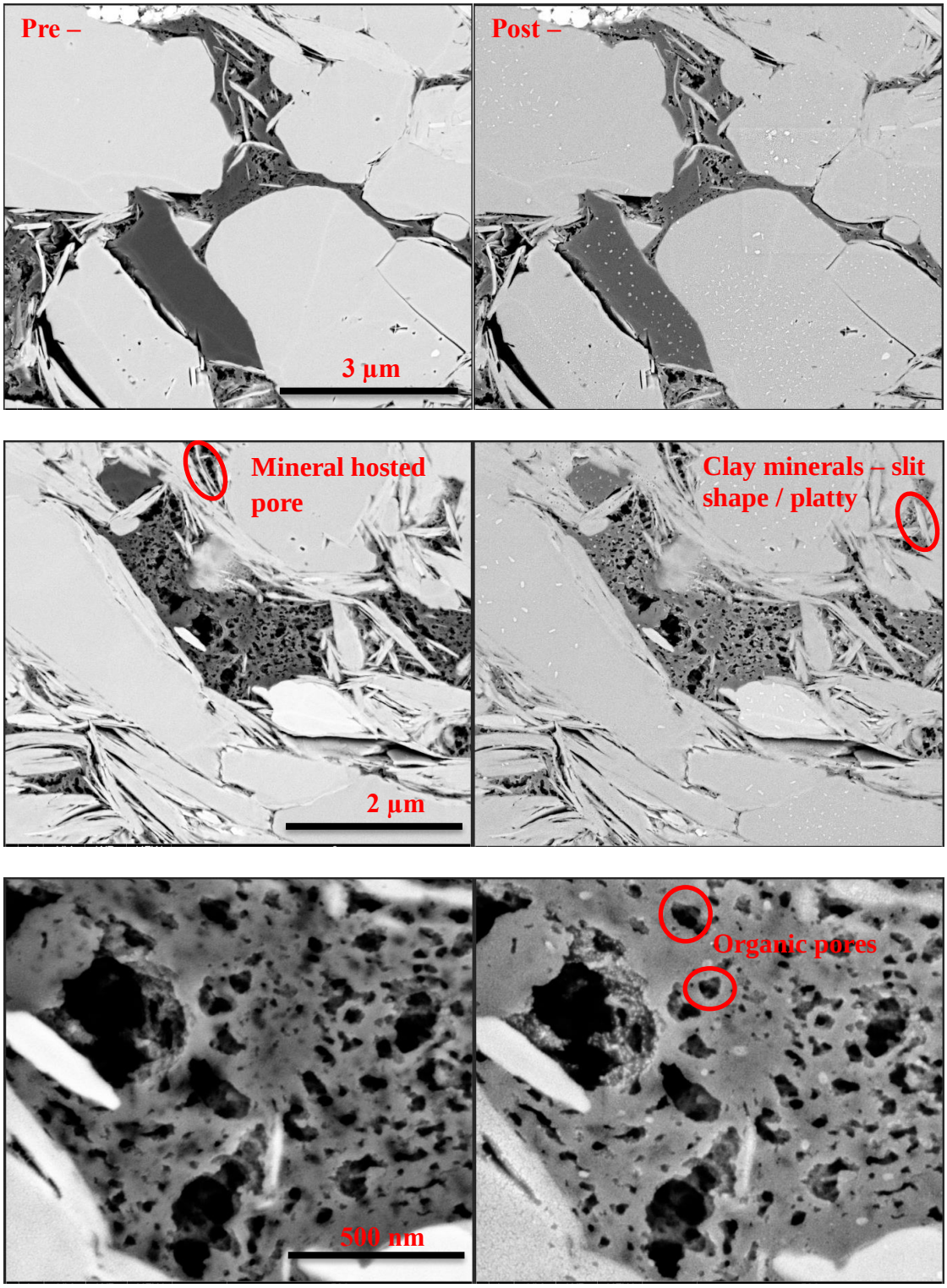

Fig. 27: SEM images of the gas shale from the Marcellus formation (clay – 72 wt%, TOC – 4.5 wt%) showing abundant organic pores. There is no change in the microstructure pre- and post-extraction. The pores associated with clay minerals appear to be slit-shaped.

4.6 Adsorption / Desorption Isotherms for shales and kerogens

Nitrogen adsorption/desorption isotherms and their hysteresis patterns may provide information about the physisorption mechanism and pore structure characteristics of shales (Kuila and Prasad, 2013). In this study, nitrogen gas adsorption technique was used to obtain the quantitative pore structure parameters including the specific surface area (SSA) and PSD of OM with different thermal maturity.

4.6.1 Low pressure N_2 analyses – Organic rich shales

Low pressure N_2 isotherms for "as-received" and solvent extracted organic rich shale samples are shown in **Fig. 28**. According to the IUPAC classification of isothermal adsorption curves, the isotherms of shale samples were confirmed to be Type IV and hysteresis is Type H_3 indicating slit-shaped pores (Sing et al. 1985) and the 'forced closure' phenomena of the desorption isotherm confirming the presence of pores with diameter less than 4 nm.

In general, the adsorbed N_2 quantity and the specific surface area increased post extraction, **Figs. 28 a, b, c and d.** The adsorption isotherms show that, the adsorption quantity dramatically increases as the relative pressure approaches 1.0, without showing a saturation phenomenon. This implies the presence of meso- and macropores in the shale sample and confirming the occurrence of capillary condensation at higher relative pressures. The Soxhlet extract was analyzed using GC-MS spectra which showed the presence of both light and heavy hydrocarbons from C_{11} to C_{30+}. This confirms that solvent extraction removes intermediate to heavy hydrocarbons and hence the increase in

surface area in immature, oil and condensate window can be attributed to removal of soluble hydrocarbons which are clogging the pore space within the OM (Mastalerz et al., 2013).

The adsorption isotherm for the solvent extracted Bakken sample **(Fig. 28a – immature window)** shows a faster and a larger adsorption capacity than the adsorption isotherm for the "as-received" formation at lower relative pressure (P/Po < 0.8), indicating that the former (solvent extracted sample) has more nanopores. This confirms that Soxhlet solvent extraction removed the soluble hydrocarbons which previously coated the surfaces of the pores and decreased the estimation of the specific surface area. Valenza et al. (2013) observed similar increase in surface areas of shales after solvent extraction, especially noticeable within a Ro range of 1.0 – 1.5 %, and attributed this effect to the opening of formerly bitumen-clogged pores. The percentage increase in specific surface area after solvent extraction for different maturities are shown in **Table 4**.

The adsorption isotherm for the "as-received" Marcellus sample **(Fig. 28d – gas window)**, shows a higher surface area compared to samples from lower maturities (**Figs. 28a – 28c**). This large increase might be due to the generation of abundant nanopores during maturation which contribute to the surface area. Another aspect is that the percent increase in surface area post extraction is negligible in the gas window. This indicates that in these mature shales there is no mobile HC's.

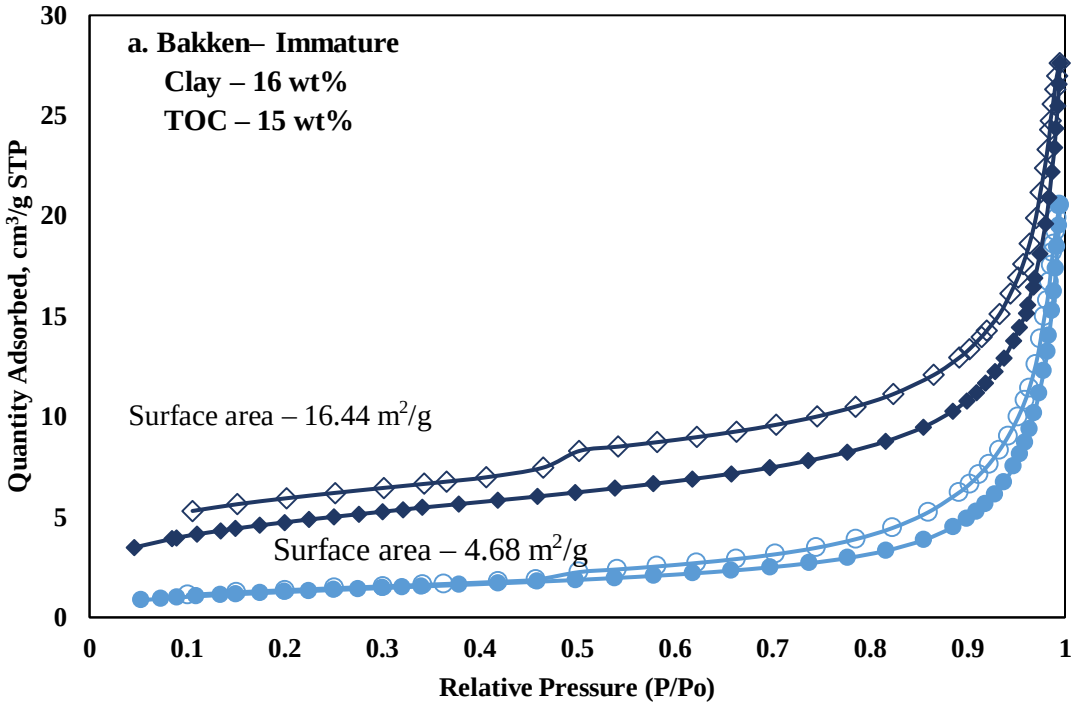
a. Bakken– Immature
Clay – 16 wt%
TOC – 15 wt%
Surface area – 16.44 m²/g
Surface area – 4.68 m²/g
Quantity Adsorbed, cm³/g STP
Relative Pressure (P/Po)
0
5
10
15
20
25
30
0
0.1
0.2
0.3
0.4
0.5
0.6
0.7
0.8
0.9
1

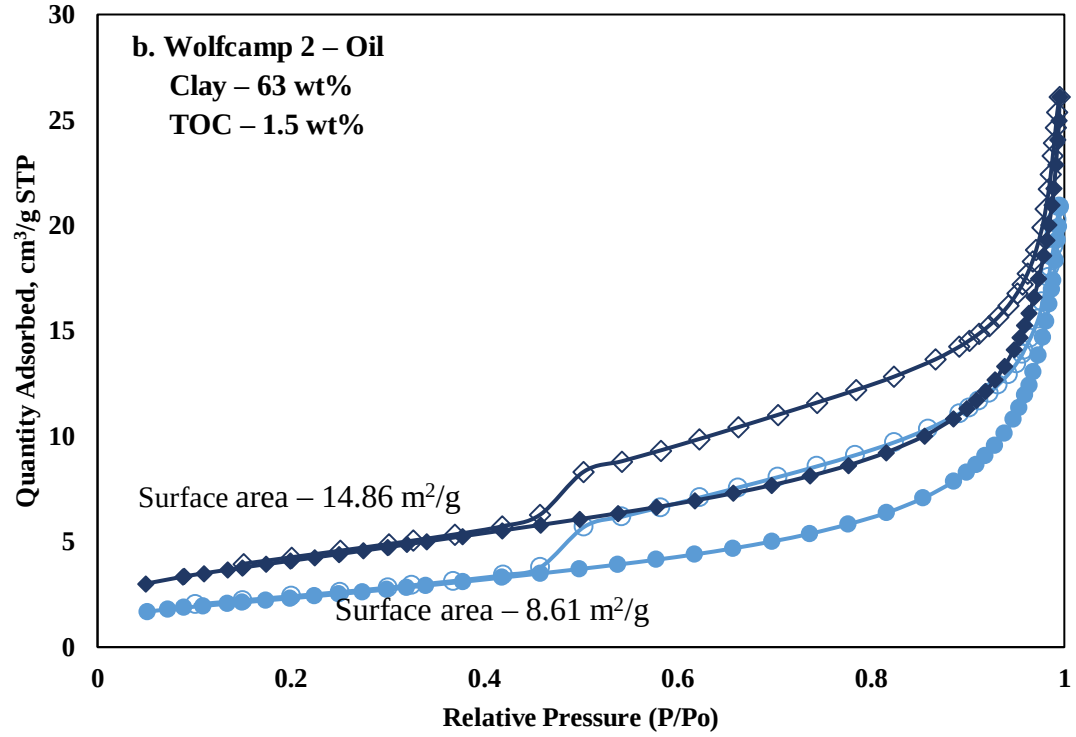
b. Wolfcamp 2 – Oil
Clay – 63 wt%
TOC – 1.5 wt%
Surface area – 14.86 m²/g
Surface area – 8.61 m²/g
Quantity Adsorbed, cm³/g STP
Relative Pressure (P/Po)
0
5
10
15
20
25
30
0
0.2
0.4
0.6
0.8
1

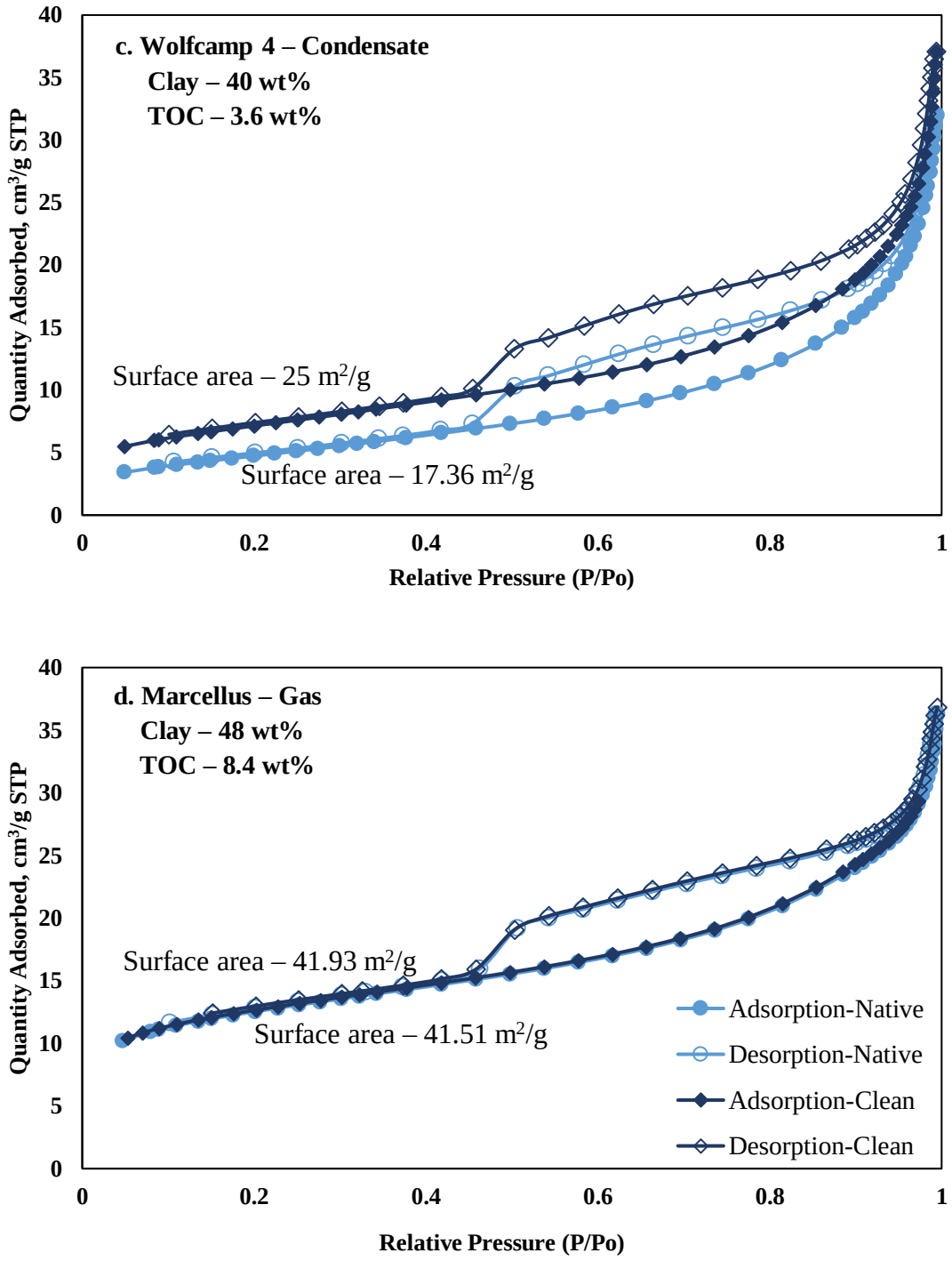

Fig. 28: Adsorption-desorption isotherms of the shale sample from: a. Bakken (immature), b. Wolfcamp 2 (oil), c. Wolfcamp 4 (condensate) and d. Marcellus (gas) formations. The isotherms for the native and clean samples from each formation are shown. In all but the Marcellus isotherm for the "as-received" sample shows a substantial surface area implying the presence of abundant nanopores. The circles represent the "as-received" state and the diamonds represent the solvent extracted state.

Table 4: Summary of the measured specific surface areas for the samples shown in Fig 22.

Formation	Maturity	"As-received" surface area (m^2/g)	"Solvent-extracted" surface area (m^2/g)	Increase %
Bakken	Immature	4.68	16.44	251
Wolfcamp 2	Oil	8.61	14.86	72.7
Wolfcamp 4	Condensate	17.36	25.00	44
Marcellus	Gas	41.51	41.93	0.9

The adsorption increases with increasing maturity, as shown in **Table 4**. Soxhlet extracted samples show noticeable changes in the quantities of adsorbed nitrogen. These observations indicate the BET surface area increases as much as 251% for samples from immature window to little change for samples from the mature gas window.

4.6.2 Pore size distribution for organic rich shales

The distribution of pore volume with respect to pore size can be displayed as cumulative, incremental or differential distribution curves (Chalmers et al., 2012; Clarkson et al., 2012; Kuila and Prasad, 2013). The plot of dV/dlog(D) versus D (pore diameter) is frequently used to display the PSD using the BJH method (Clarkson et al., 2012; Kuila and Prasad, 2013). In this study, DFT technique was used for the PSD analysis for the organic-rich shales between 2 – 200 nm for two reasons:

1. The hysteresis pattern based on the IUPAC classification suggest the pores are slit shaped.
2. The wt% of minerals dominated over the organic matter content and that the pore types associated with the minerals are slit type which was confirmed using SEM (**shown in Fig. 27**).

The PSD of the mesopores and part of the macropores obtained from the gas adsorption analysis using differential and cumulative pore volumes pre-solvent extraction is presented in **Fig. 29**. For the immature window the PSD is mainly dominated by larger meso- and smaller macropores. In case of oil, condensate and gas window, the PSD suggested multi-modal distribution with the main mode approximately between 25 and 60 nm and the other mode is less than 10 nm.

Immature Samples

For the immature window, the pore size is mainly dominated by larger meso- (> 10 nm) and smaller macropores in comparison to other maturity groups (**Fig. 29 – Immature**).

The PSD peaks in volume around 30 – 60 nm and progressively decreases in volume toward smaller pore sizes.

Oil window samples

Samples from the oil window exhibit a similar character to the immature wells, but contain less porosity within the fine macropore and coarse mesopore size fraction (**Fig. 29 – Oil**). The samples from Wolfcamp formation display a modal peak in pore volume at approximately 3 nm which is associated with clay hosted porosity, indicating clay microstructure may be a significant control on porosity (Kuila et al. 2014b). The PSD peaks in volume around 30 – 90 nm and progressively decreases in volume toward smaller pore sizes. TOC shows a moderate control on the pore distribution, with greater TOC samples generally having greater pore volumes and vice versa.

Condensate window samples

The samples from the condensate window show variable amount of coarse meso- and macropores and slightly greater fine mesopore volumes in comparison to the immature and oil window samples. The pore volume only decreases slightly in the fine mesopore size fraction (**Fig. 29 – Condensate**). All the samples from the same well display similar pore size distribution trends. No significant correlation is observed between pore volume distribution and TOC and moderate correlation with clay content.

Dry gas window samples

Overmature samples, in general have the least amount of pore volume within the macropore and coarse mesopore in comparison to samples from other maturity (**Fig. 29 – Gas**). There is pronounce increase in pore volume with decreasing pore size. High pore volumes are associated with high TOC (> 4 wt%) and high clay contents (> 40 wt%). The

sample with the greatest fine mesopore volume is associated with both high TOC (8.4 wt%) and high clay content (48 wt%).

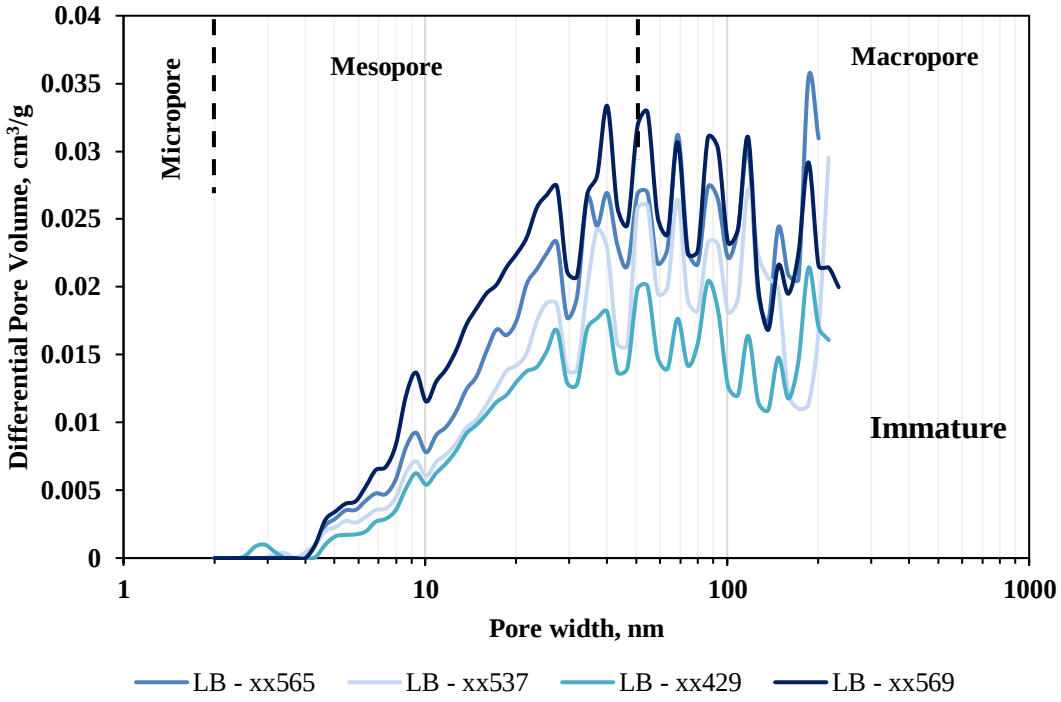

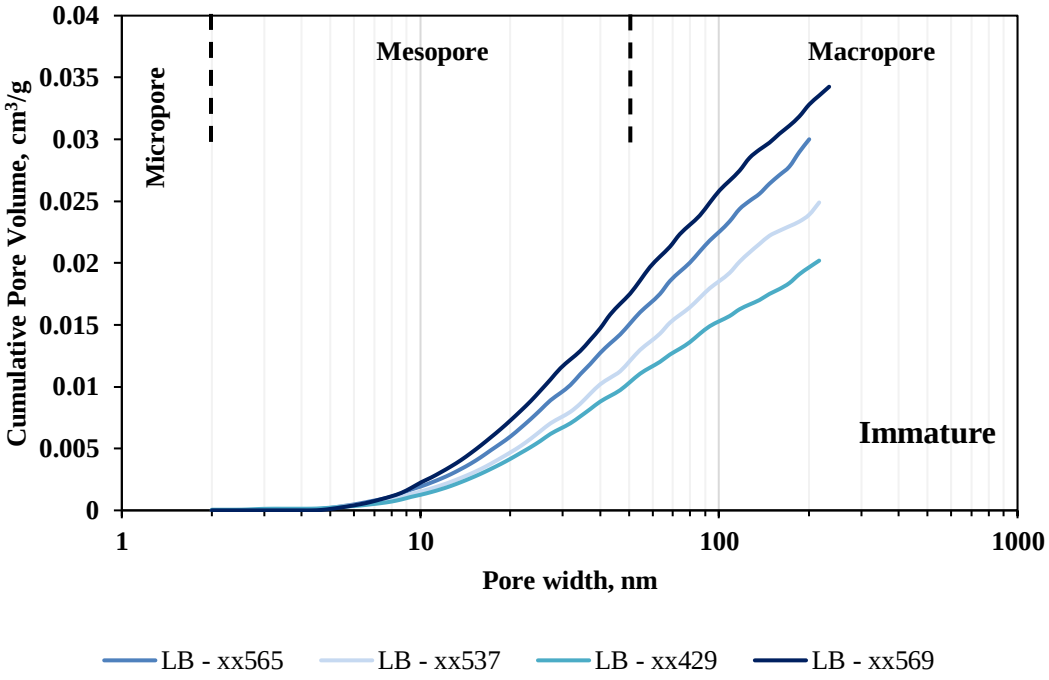

*LB – Lower Bakken

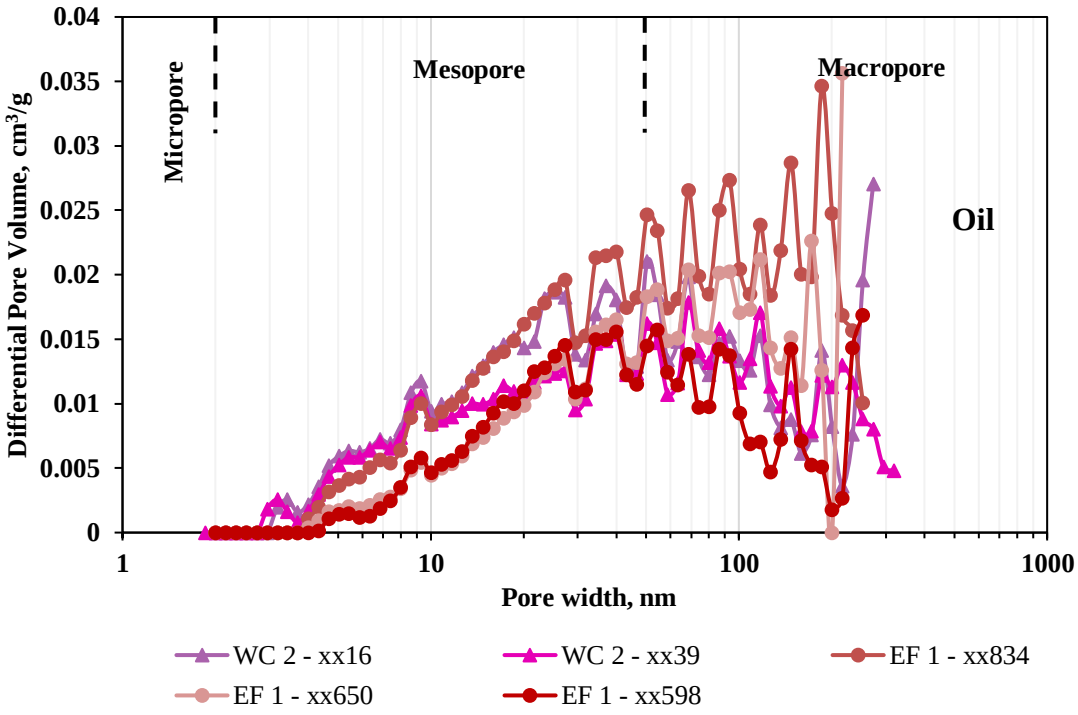

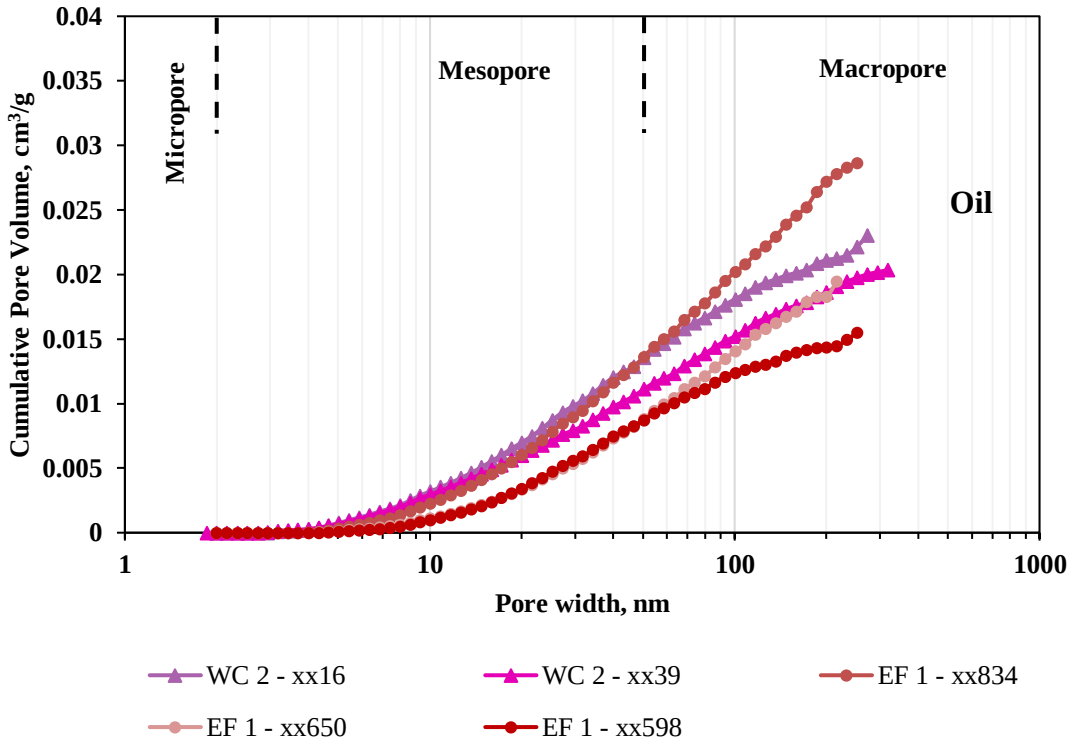

*WC 2 – Wolfcamp 2 and EF 1 – Eagle Ford 1

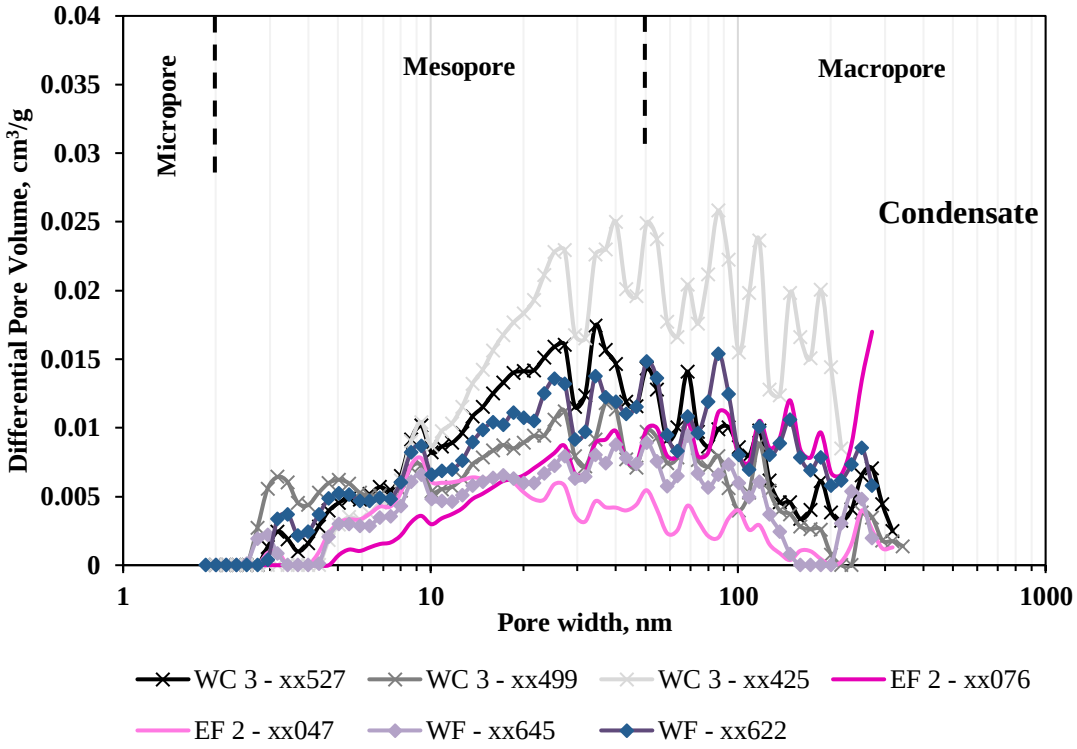

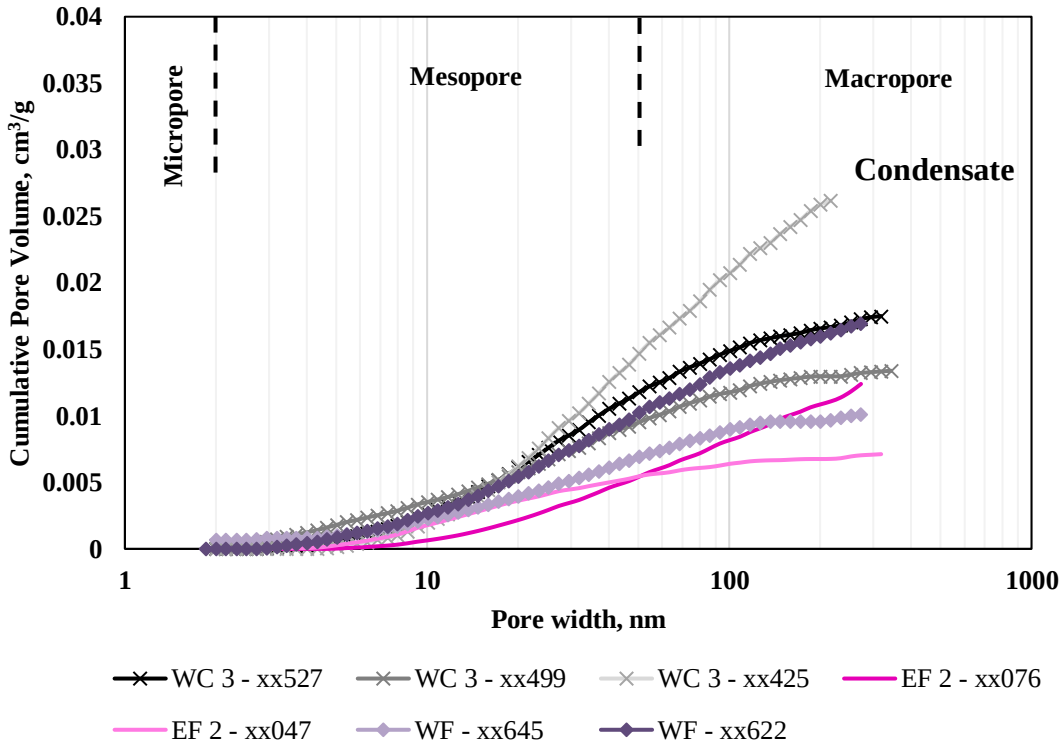

*WC 3 – Wolfcamp 3, EF 2 – Eagle Ford 2 and WF – Woodford

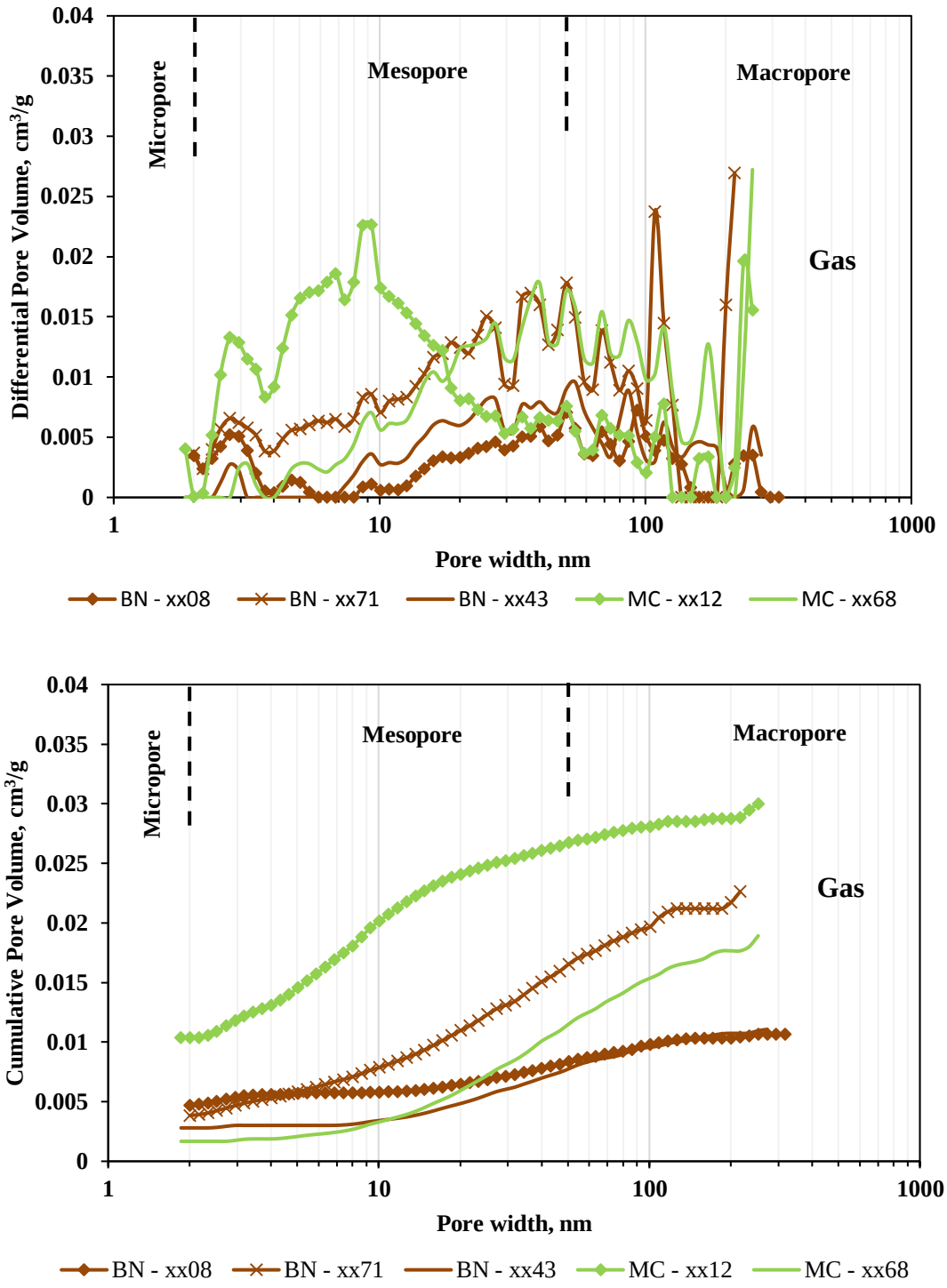

*BN – Barnett and MC – Marcellus

Fig. 29: Comparison of PSD for immature, oil, condensate, and gas window. The graph for differential and cumulative pore volume from each maturity is shown as a function of pore width derived from the N_2 adsorption branch of the isotherms using the DFT model.

The distribution of specific surface area with respect to pore size, for varying maturity samples show similar shapes. (**Fig. 30**). DFT method of PSD was used to quantify the mesoporous characteristics of the shale samples in each maturity window (**Section 2.6**). The PSD suggests that specific surface areas are dominated by pores smaller than 10 nm in width, which is consistent with the results for many gas shales in North American basins (Chalmers and Bustin, 2008; Ross and Bustin, 2009).

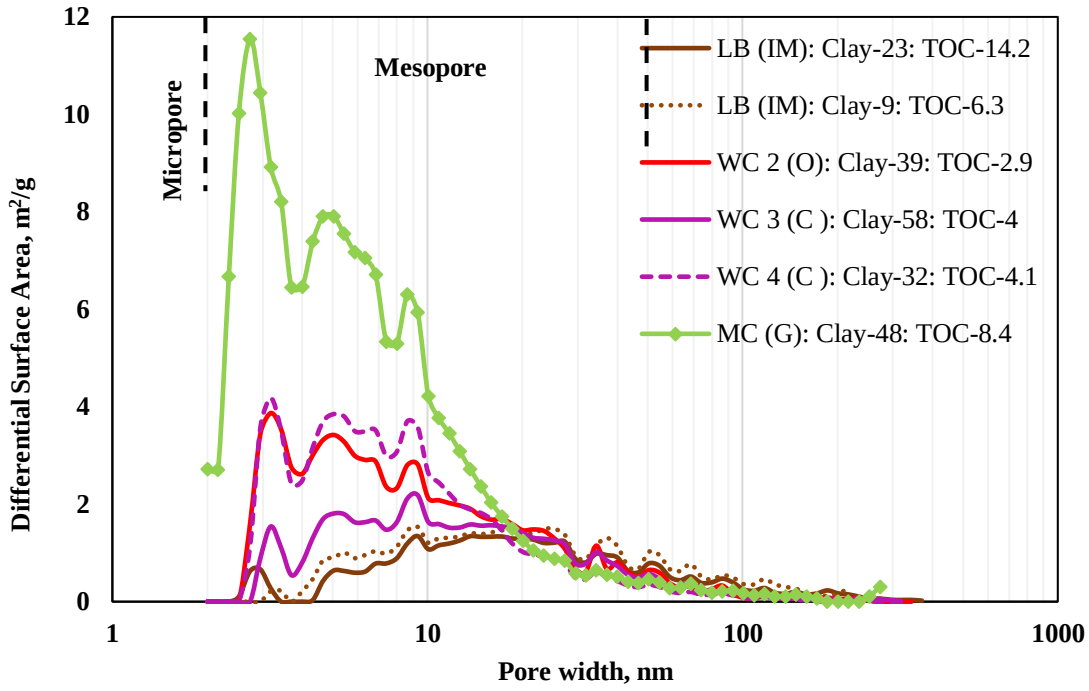

Fig. 30: Comparison of surface area distribution with pore size derived from N_2 adsorption isotherm using DFT model for varying maturity samples.

The next part of the analysis was to compare the distribution of specific surface area with respect to pore size, for samples from the immature, oil and gas window pre- and post-extraction, to identify, where exactly the soluble HC's are coming from (grain coating).

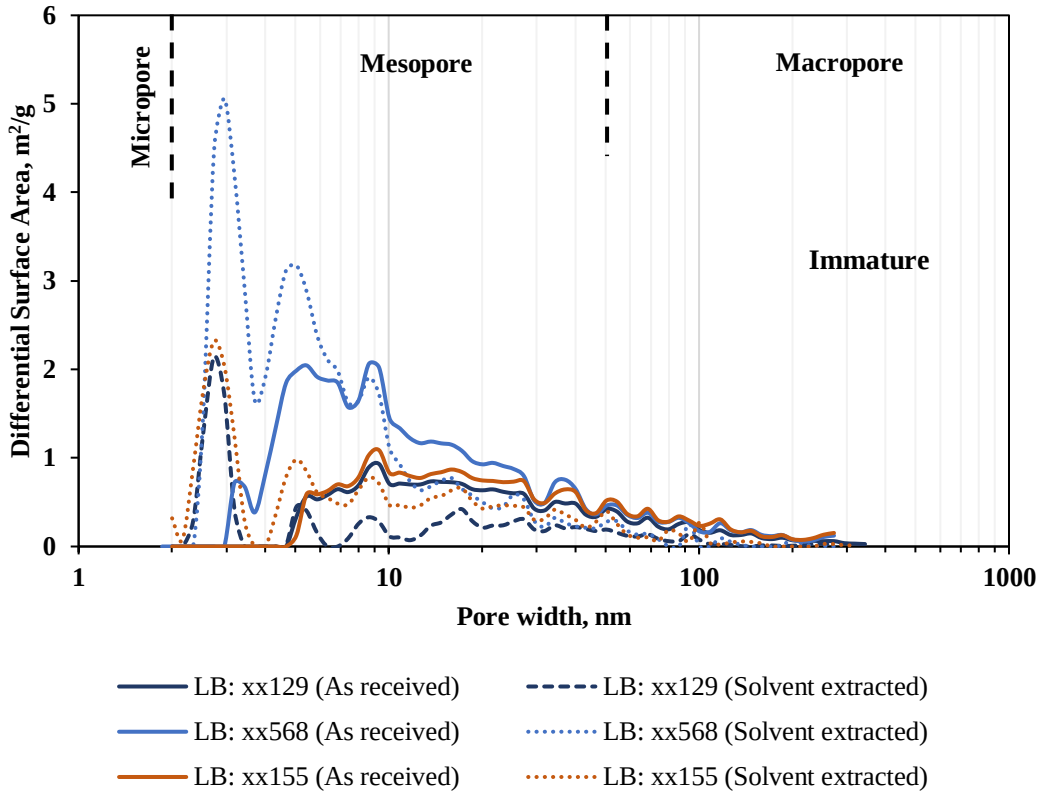
Micropore
Mesopore
Macropore
Immature
Differential Surface Area, m²/g
Pore width, nm
LB: xx129 (As received)
LB: xx129 (Solvent extracted)
LB: xx568 (As received)
LB: xx568 (Solvent extracted)
LB: xx155 (As received)
LB: xx155 (Solvent extracted)

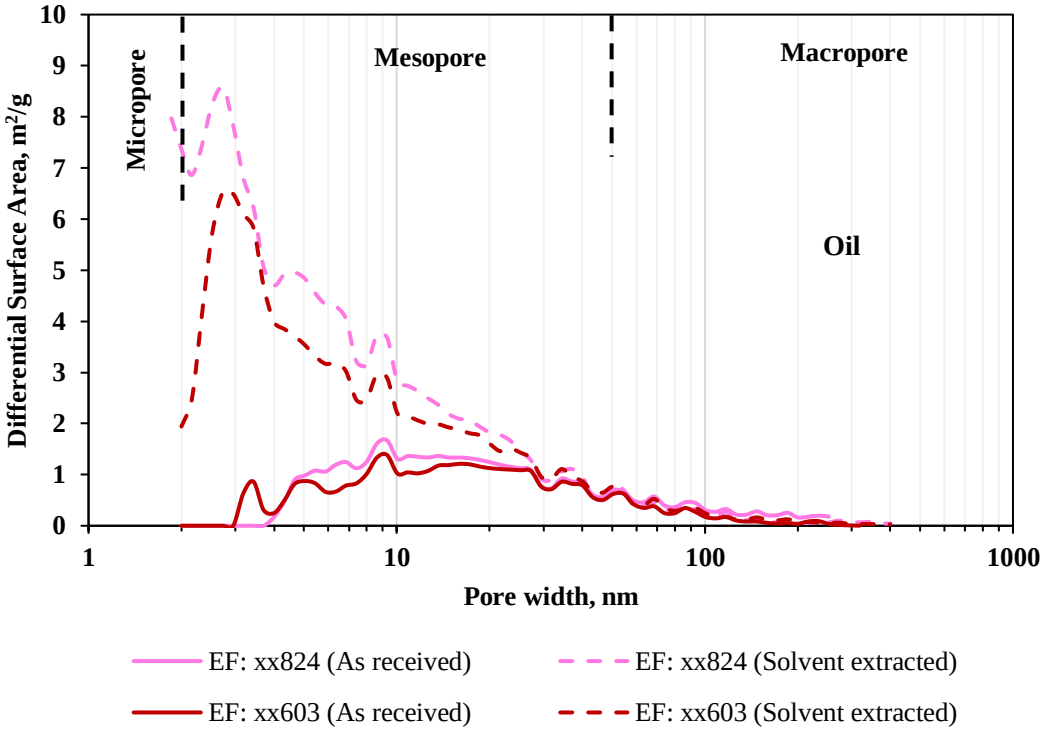
Micropore
Mesopore
Macropore
Oil
Differential Surface Area, m²/g
Pore width, nm
EF: xx824 (As received)
EF: xx824 (Solvent extracted)
EF: xx603 (As received)
EF: xx603 (Solvent extracted)

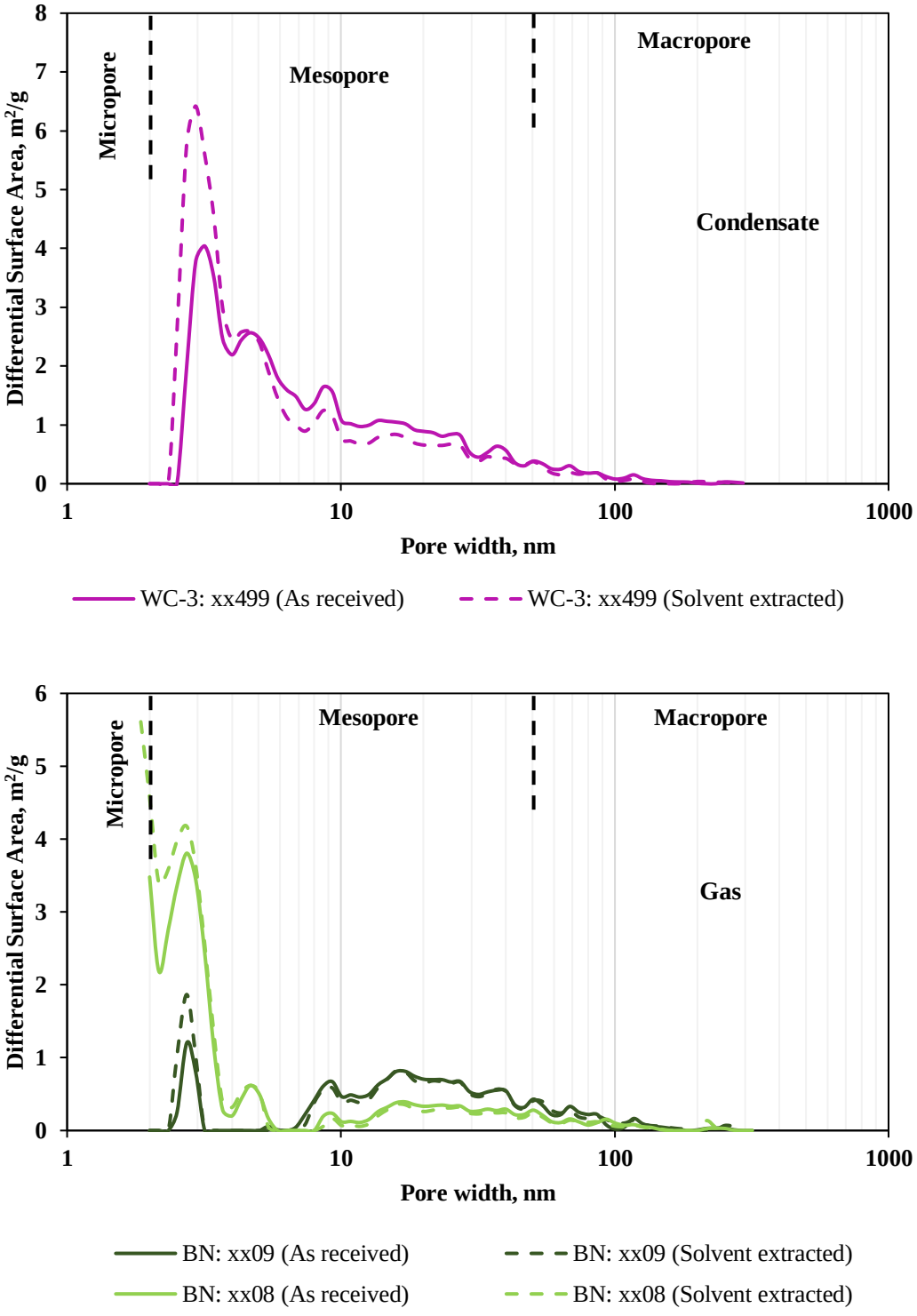

Fig. 31: N_2 differential surface area plots for selected samples from varying thermal maturity window subjected to solvent extraction. Plots were generated using the DFT method applied to the adsorption branch of the isotherms. The maximum change in surface area was observed in the oil window suggesting removal of movable hydrocarbons from the finer mesopores.

Immature window samples

In case of the sample from the immature window (**Fig. 31 – immature**) the method of solvent extraction is effective only in smaller mesopores (< 10 nm) suggesting that the organic solvent dissolves the soluble hydrocarbons and the solid bitumen present in these small pores. Another possibility can be that the residual oil mixes with the solvent, begins to mobilize and is redistributed within the porous network of the rock. Some of the oil may have coated the clay particles or entered the mesorpores greater than 7 nm.

Oil, condensate and gas window samples

In case of samples from oil, condensate and gas window it is evident that the impact of organic solvents is effective in the pores ranging from 2 – 20 nm, since, beyond 20 nm, the differential surface area curves overlay that of the "as-received" state of the samples suggesting most of the HC's are coating the smaller grains thereby inhibiting the measurement of true surface area.

4.6.3 Isolated Kerogen

Kerogen was isolated from their respective shale formations and then analyzed for specific surface area and PSD. The shapes of the isotherms for each kerogen type are very distinct. **Figs. 32, 33 and 34** shows a plot of quantity adsorbed versus relative pressure for kerogen samples from the immature, oil and gas maturity region having T_{max} in the range of 417°C to >600°C.

Green River (IM), Kimmeridge (IM), Woodford (IM), Lower Bakken (O) and Wolfcamp (O) kerogens barely show any hysteresis. The forced closure of hysteresis at relative pressure of 0.45 was not observed suggesting absence of micropores. The presence of

larger meso- and smaller macropores is confirmed by the gradual uptake of N_2 at relative pressure of 1.0.

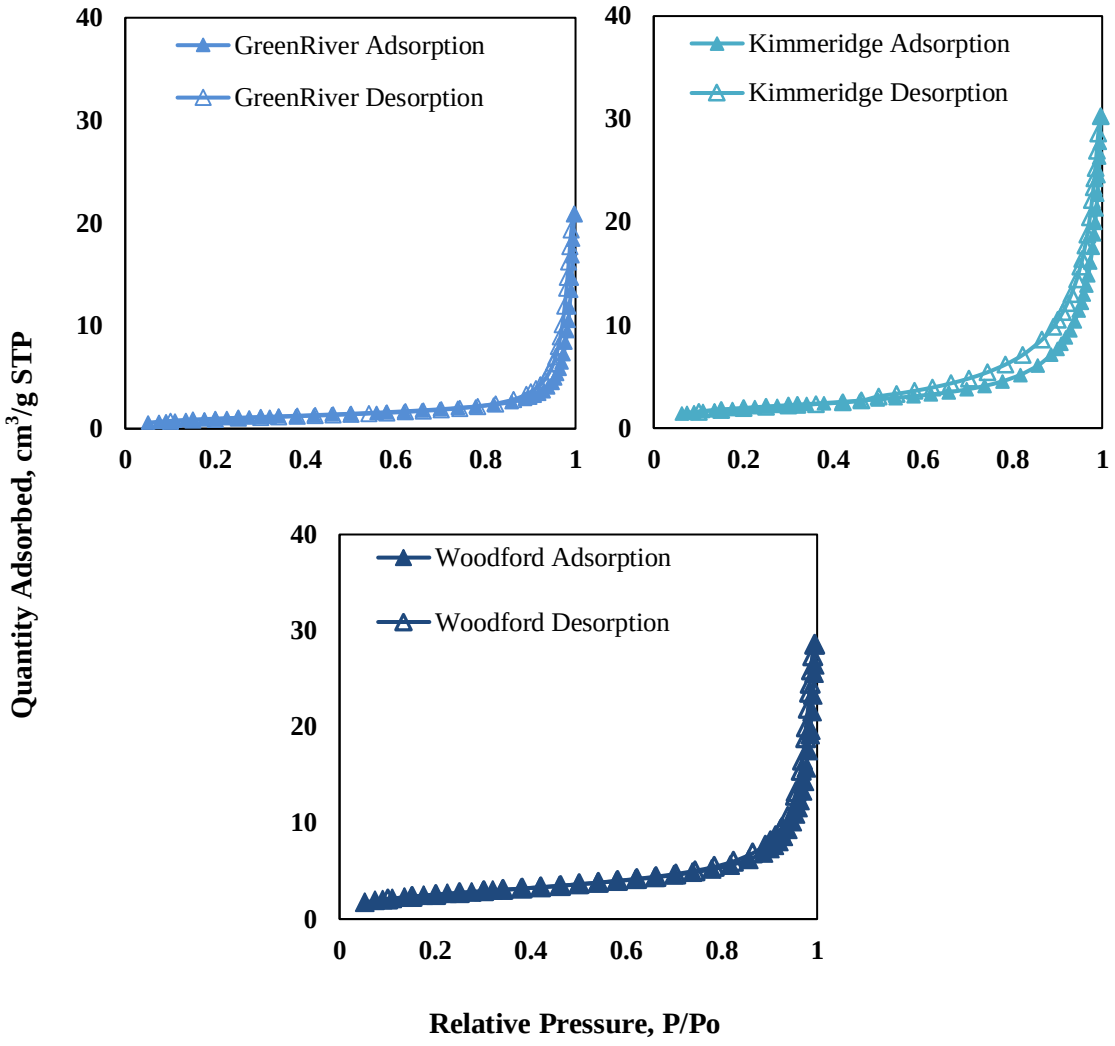

Fig. 32: Nitrogen adsorption and desorption curves for different kerogen samples from the immature window.

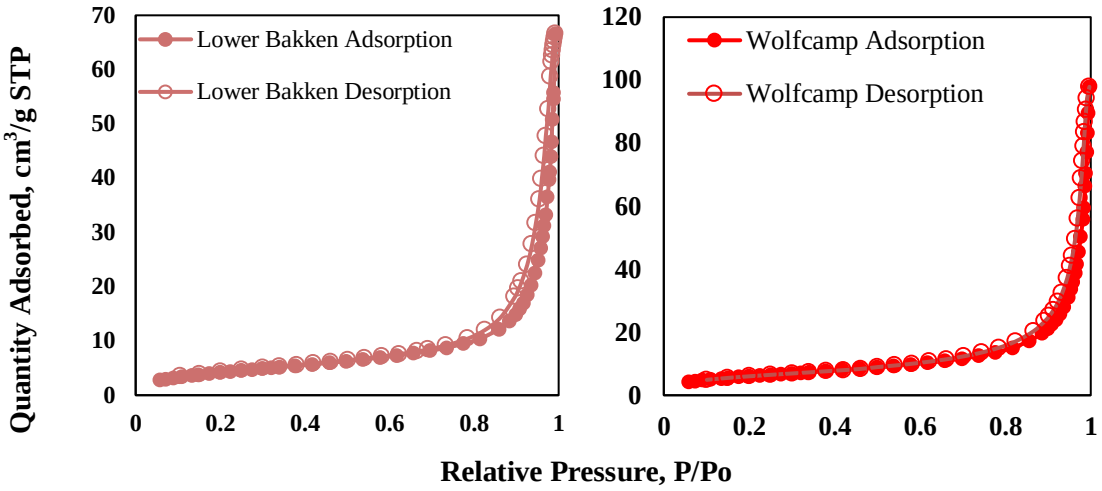

Fig. 33: Nitrogen adsorption and desorption curves for different kerogen samples from the oil window.

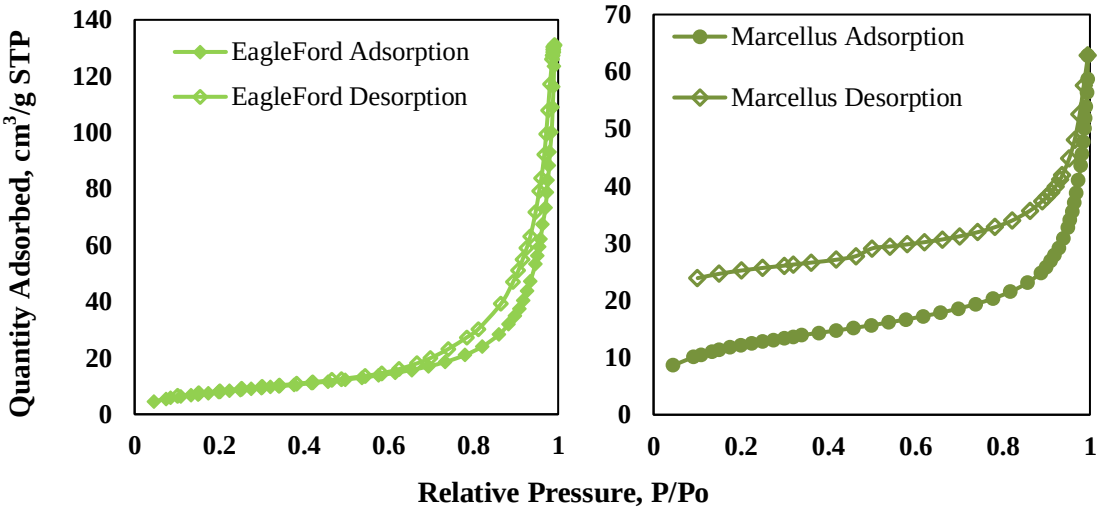

Fig. 34: Nitrogen adsorption and desorption curves for different kerogen samples from gas window.

The isotherm profiles of the Eagle Ford (G) and Marcellus (G) kerogen suggest that the samples are dominated by the mesopores (indicated by the hysteresis pattern) and macropores (indicated by the absence of plateau at higher P/Po = 1). The Eagle Ford isotherm does not show a strong 'forced closure' of the desorption branch (Groen et al., 2003).

The isotherm of the OM from the Marcellus sample shows a characteristic phenomena of hysteresis i.e. the open loop hysteresis as explained by Gregg and Sing (1982). They attribute this phenomenon of lack of hysteresis loop closure below a relative pressure of 0.45, as the result of swelling or adsorption of nitrogen in the micropores. Mastalerz et al. (2012) and Cai et al. (2013) observed similar phenomena in adsorption in coals and marine shales.

4.6.4 Pore size distribution for isolated kerogens

The PSD for the OM was obtained using the BJH inversion method, since the OM pores are typically round to sub-round bubble-like pores (**Fig. 27**). These OM pores either occur as individual pores, unconnected bubble pores or as bubble pores that connect and create a potential network. The OM samples from Woodford, Bakken and Eagle Ford have BET-surface area of 9.24 m^2/g, 15.81 m^2/g and 30.58 m^2/g respectively.

The PSD patterns for the isolated kerogens are similar to those of their shale counterparts, but the pore volumes associated with the kerogens is higher than the respective shale samples (**Fig. 36**).

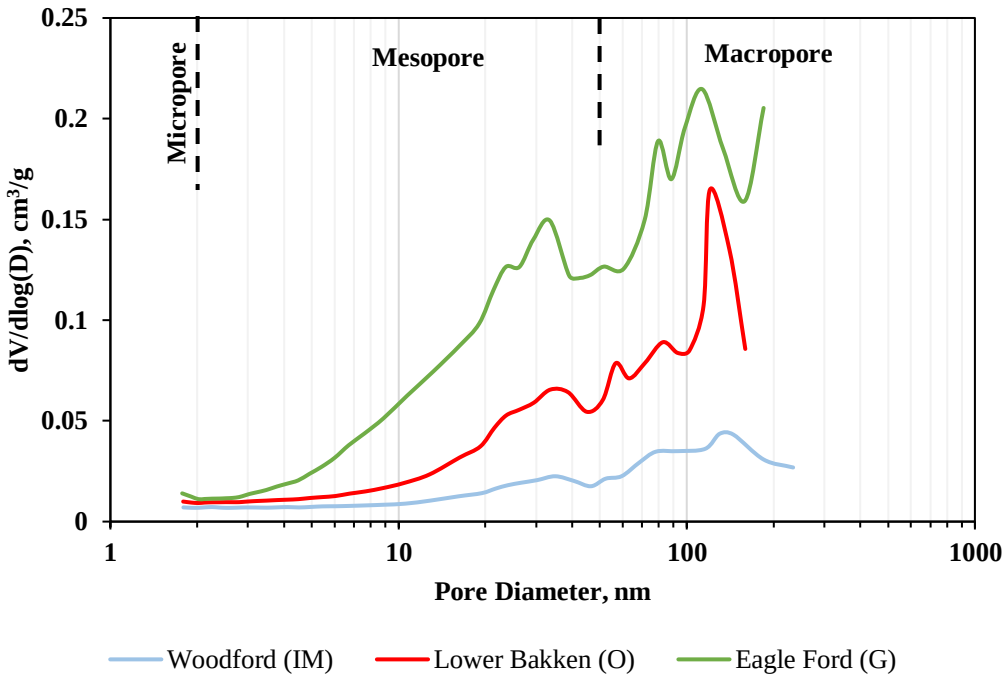

Fig. 35: Plots showing pore volume distributions with pore diameter derived from the N_2 adsorption branch of isotherms for Woodford, Bakken and Eagle Ford kerogens using BJH model.

Fig. 36 shows the relationship between the pore size distribution and the pore surface area for the isolated kerogen from immature (Woodford), low maturity (Bakken) and mature (Eagle Ford) windows. The specific surface area of immature Woodford kerogen and the low-maturity Bakken kerogen is due to the pores of diameter below 10 nm. However, for the mature Eagle Ford kerogen the specific surface area is attributed to pores of diameter 2 and 9 nm. The specific surface areas progressively increases with thermal maturation as more gaseous hydrocarbons are generated which are associated with finer meso- and micropores.

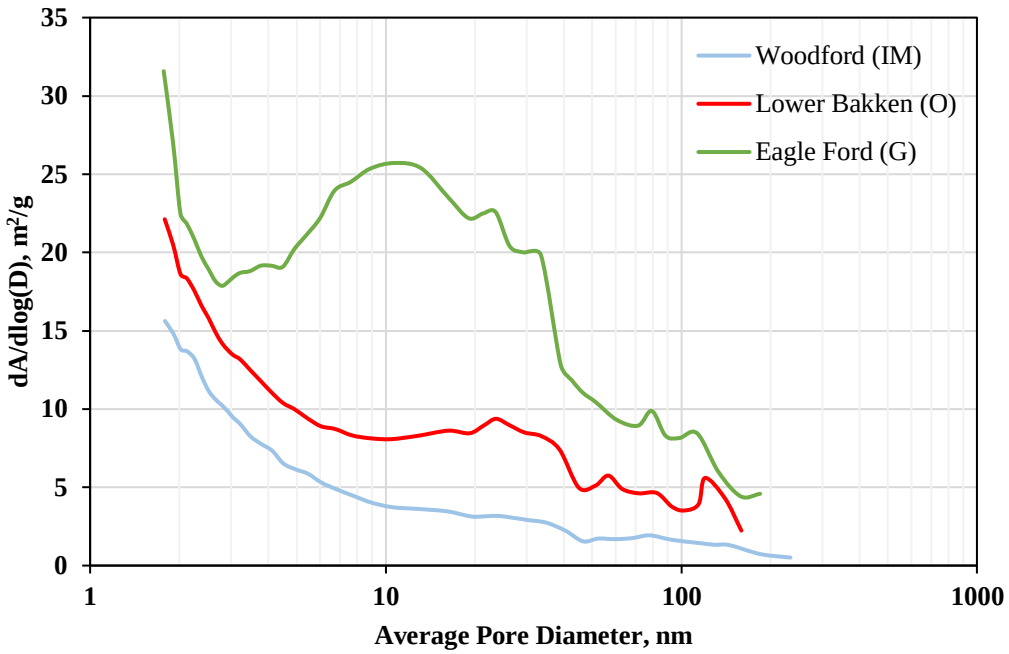

Fig. 36: Plots showing pore surface area distributions with pore diameter derived from the N_2 adsorption branch of isotherms for Woodford, Bakken and Eagle Ford kerogens using BJH model. The abrupt increase in the pore volume (6 – 10 nm) for the Eagle Ford sample can be due the irregular fit of the adsorption isotherm data points with the BJH model.

4.7 Surface area correlation with clay, TOC and thermal maturity on adsorption

One of the important characterization parameters in evaluating the unconventional shale resource plays is the TOC. The amount of OM present is found to be directly proportional with total porosity (Passey et al., 2010), microporosity (Chalmers and Bustin, 2007; Ross and Bustin, 2009) and methane adsorption capacity (Lu et al., 1995; Cui et al., 2009; Zhang et al., 2012).

The dependence of specifc surface area on clay content and TOC for the "as-received" shale samples is shown in **Fig. 37** and **38**. **Fig. 37** shows a plot of BET surface area, m^2/g for the "as-received" samples and clay content, wt%. The surface area obtained for the the "as-received" samples shows a very weak correlation with clay content. This is counter intuitive to the notion that increasing clay content should correlate with increased surface area. The graph consists of data points from six formations and 10 different wells, varying in thermal maturity from immature to gas. The maximum surface area obtained was 41.51 m^2/g (Marcellus – gas window) with a clay wt% of 48. The significance of the high surface area in over mature samples can be attributed to the presence of nanopores in the kerogen generated with increasing thermal maturation. The surface area of various pure clay minerals varies from 25 m^2/g to about 200 m^2/g (Macht et al., 2011).

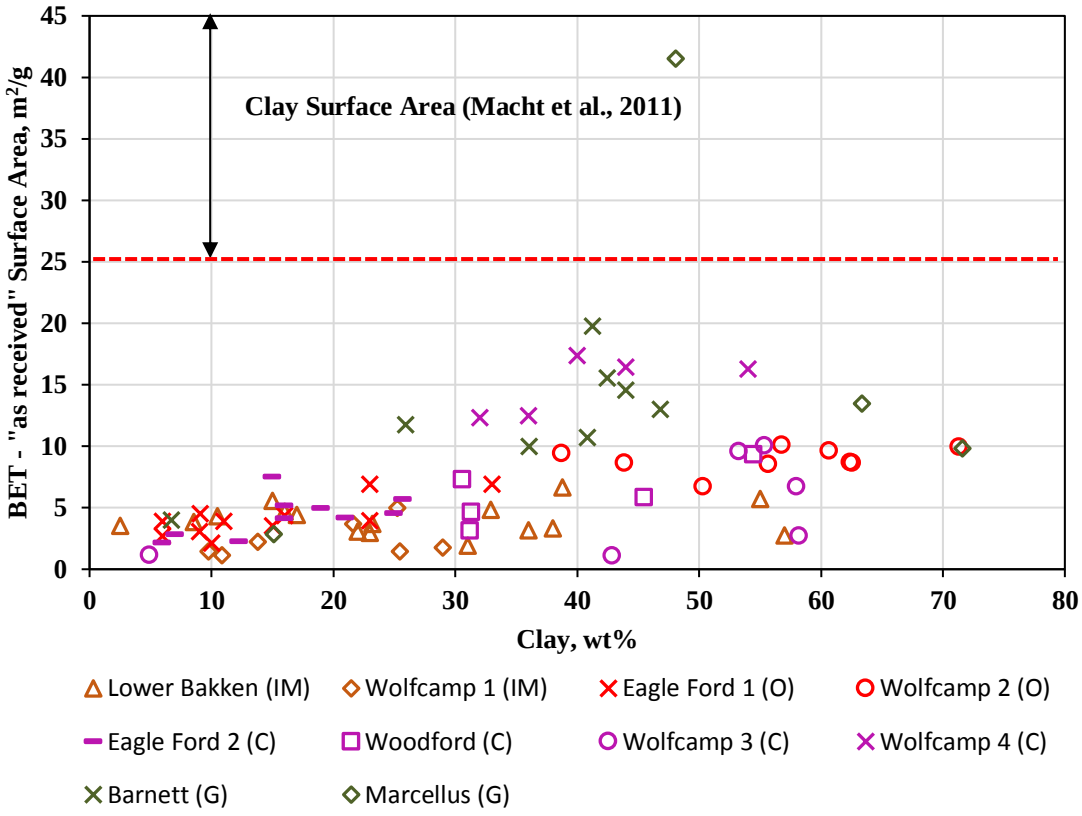

Fig. 37: Relationship between BET-surface area and clay for "as-received" shale samples from different maturity windows. The surface area shows a weak positive correlation with amount of clay. The surface area increases as a function of maturity from as 1.14 m^2/g (Wolfcamp 1 – immature) to as high as 41.51 m^2/g (Marcellus – gas). The low surface area in the immature window can be attributed to the presence of soluble hydrocarbons coating the surface os the shale samples, masking the true surface area. The increase in surface area with increasing maturity is attributed to the generation of nanopores.

Fig. 38 shows relation between BET-on "as received" surface area with OM content represented in terms of TOC. The data appear to possess considerable scatter. There is no definite correlation observed. As such, the differences in the amount and composition of organic and/or inorganic minerals in different shales may cause significant differences in the specific surface area. The open symbols represent "as-received" state of the samples.

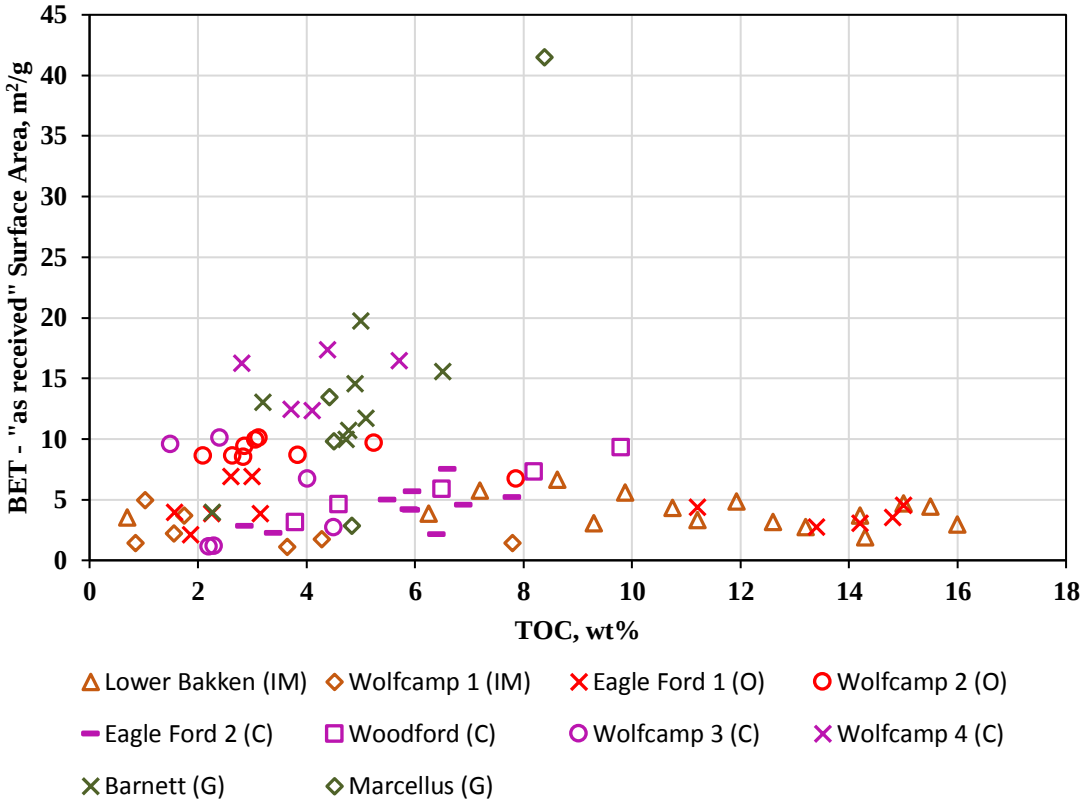

Fig. 38: Relationship between BET-surface area and TOC for "as-received" shale samples from different maturity windows. The surface area shows a considerable scatter. There is no definite correlation observed between the two variables.

Cao et al. (2015) concluded that the surface area in organic rich shale is mainly controlled by the kerogen type, clay mineral content and maturity. In addition, it is also influenced by dominant type of clay mineral, age, depth of burial and other factors. Lu et al. (1995) found that illite content was an important influence on the specific surface area of Devonian shales and that the CH_4 adsorption capacity increased substantially with increasing illite content. Based on the results he also concluded that the structure of illite as it resides within the shales may differ from sample to sample, and that not all the illite in the shales is expected to be accessible for adsorption.

Fig. 39 shows the "as-received" specifc surface area and illite content for the different shales. We observed that above 20 wt% illite there is a positive relationship between the two parameters. In addition, the other observation that we highlight here is for the same illite content the higher maturity shale sample shows a higher specific surface area suggesting significant contribution to the total gas storage. In case of samples having low organic content, illite may be responsible for adsorbed gas storage in shale samples.

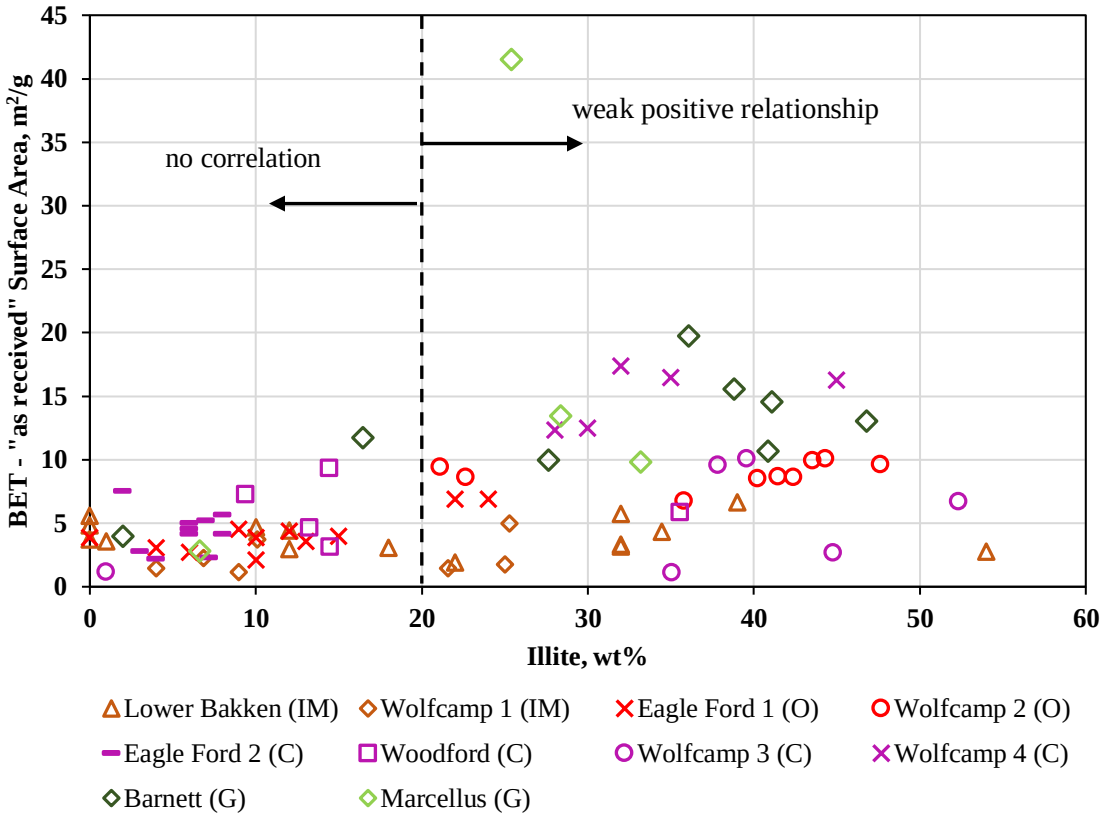

Fig. 39: Cross-plot of "as-received" surface area with illite content. The data set from all the maturity is plotted and shows a weak positive correlation between the two parameters. The vertical line at 20 wt% illite is indicative of two different relationships observed. Lower illite content (< 20 wt%) do not show any correlation with specific surface area whereas, illite content greater than 20 wt% shows a weak positive relation.

Fig. 40 is a graphical representation (box and whisker) of surface area values as a function of maturity.

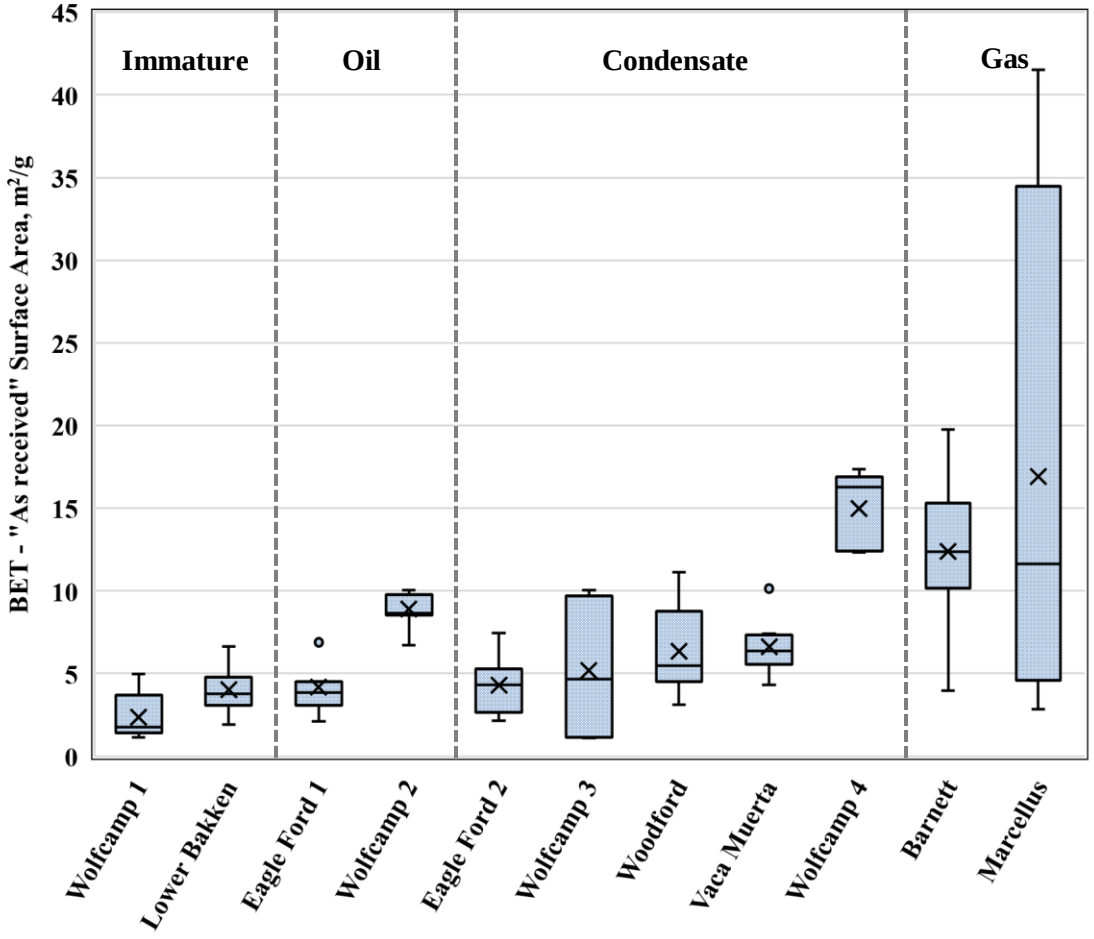

Fig. 40: Box and whisker plot of N_2-BET surface area in the "as-received" state for all wells, sorted by increasing maturity. The black line inside the bars is the median and the cross marks is the average. The wide range of values (e.g. Marcellus) may be indicative of the sedimentary variability.

The next part of the study was to solvent extract the samples and re-examine the relationship between BET-surface area, clay content and TOC (post extraction) for immature, oil, condensate and gas maturity window (**Figs. 41-44).** The open symbols in the figures represent samples in the "as-received" state whereas the closed symbols represent the samples post extraction.

To determine the dependence of clay content and TOC on the BET-surface area multiple linear regression was run pre- and post-extraction in each maturity window on the above data set. The coefficients for clay and TOC, adjusted R^2 and p-value for each case is mentioned in **Table 5** (as-received) and **Table 6** (solvent extracted). The significance level of $\boldsymbol{\alpha = 0.05}$ was used. A p-value (calculated probability) of 0.05 shows 95% probability that the observed relationships will exist, implying confidence in the observed relationship i.e. smaller the p-value ($p < 0.05$) larger the probability of correlation between the two parameters (surface area and TOC; surface area and clay).

In case of "as-received" shale samples the N_2 BET surface areas vary from 1.13 to 41.51 m^2/g. No significant correlation exists between N_2 BET surface area and sample composition when comparing all the wells. The lack of correlation can be attributed to the presence of wide range of thermally mature samples which alters the shale microstructure. For gas wells, N_2 BET surface area averages 14.92 m^2/g and shows no correlation with clay content ($R^2 = 0.14$) and a positive correlation with TOC ($R^2 = 0.63$).

With respect to the p-values listed in **Table 5** for the "as-received" samples using multiple linear regression, the coefficients for clay and TOC do not have a significant effect on the prediction of surface area ($p > 0.05$) for the immature samples. In case of oil and condensate window the coefficents for clay showed a significant effect on the prediction of surface area with low p-value ($p < 0.05$) but no effect of TOC ($p > 0.05$). In case of the gas window, the story is reversed as we observed surface area has a strong dependence on TOC with very low p-value ($p=0.005$) and no dependence on clay ($p=0.43$).

Table 5: Statistical evaluation of TOC, clay and maturity on surface area in the "as-received" state.

Maturity	Predictor	Coefficients	p-value	Adjusted R^2
Immature	Clay	0.017	0.49	-0.03
	TOC	0.042	0.53	
	Intercept	2.75	0.0013	
Oil	Clay	0.11	$p < 0.05$	0.83
	TOC	-0.04	0.48	
	Intercept	3.06	0.0005	
Condensate	Clay	0.14	$p < 0.05$	0.24
	TOC	0.15	0.63	
	Intercept	1.77	0.55	
Gas	Clay	0.09	0.43	0.58
	TOC	4.87	$p < <0.05$	
	Intercept	-13.61	0.083	

Figs. 41-44 show the correlations between BET-surface area, clay content and TOC post extraction. The surface area measurements (post extraction) now show correlations with clay content and TOC which were not evident in the "as received" state (**Fig. 37 and 38**).

4.7.1 Immature window

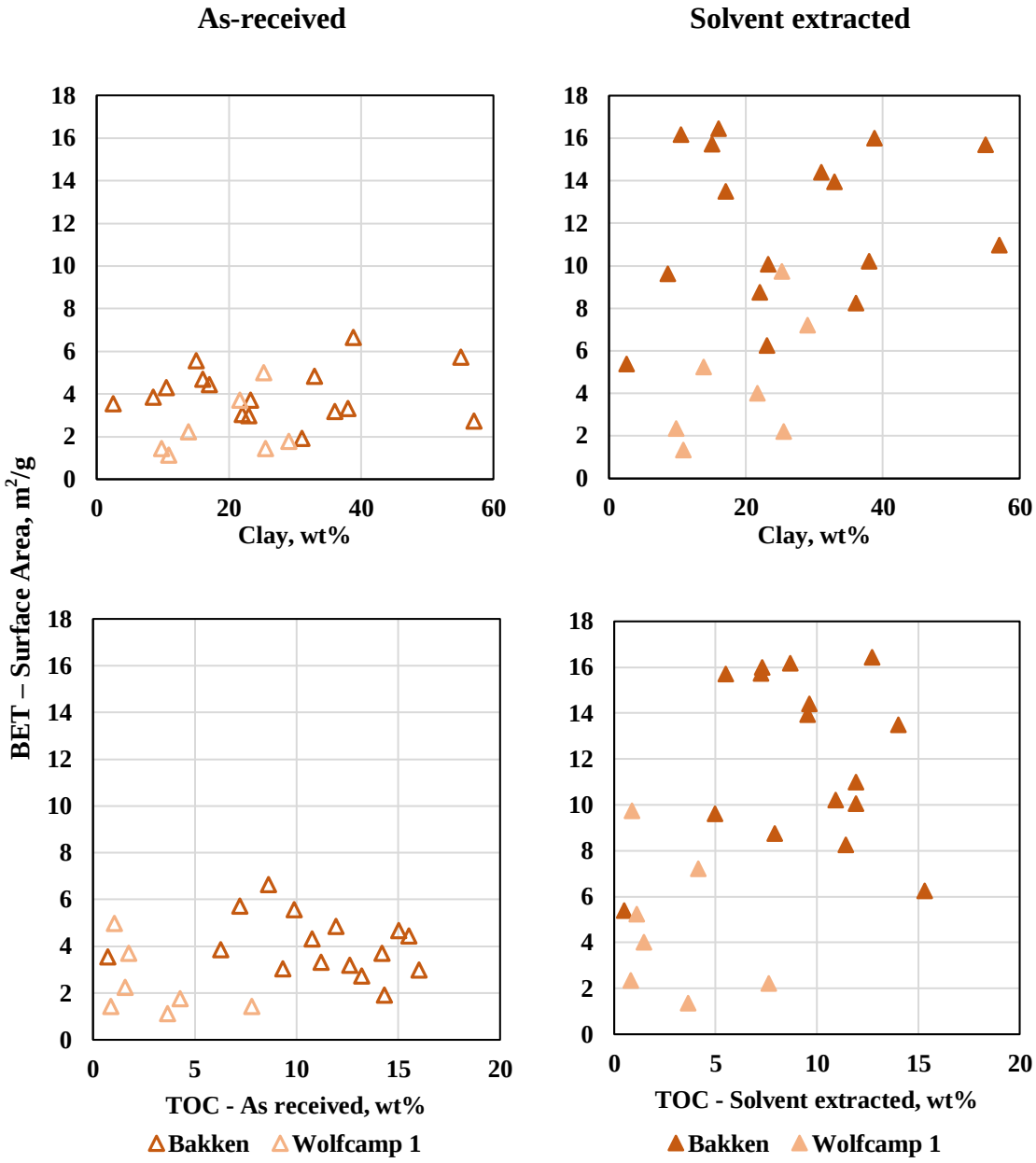

Fig. 41: Relationships between BET-surface area with clay and TOC for "as-received" and solvent extracted state for the samples in the immature window (Bakken-dark orange, Wolfcamp 1-light orange).

4.7.2 Oil window

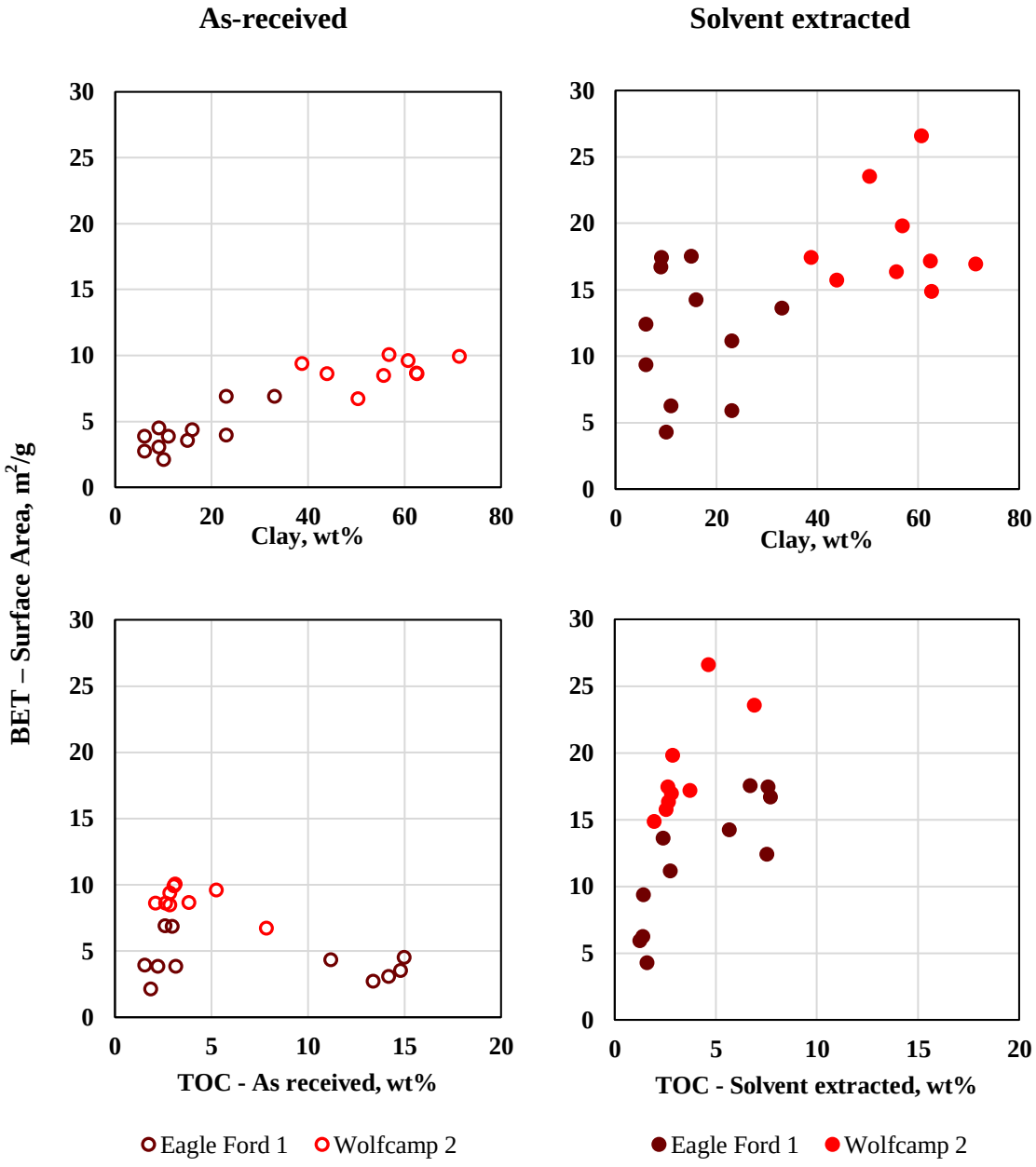

Fig. 42: Relationships between BET-surface area and clay and TOC for "as-received" and solvent extracted state for the oil window (Eagle Ford 1-maroon, Wolfcamp 2-red) shale samples.

4.7.3 Condensate window

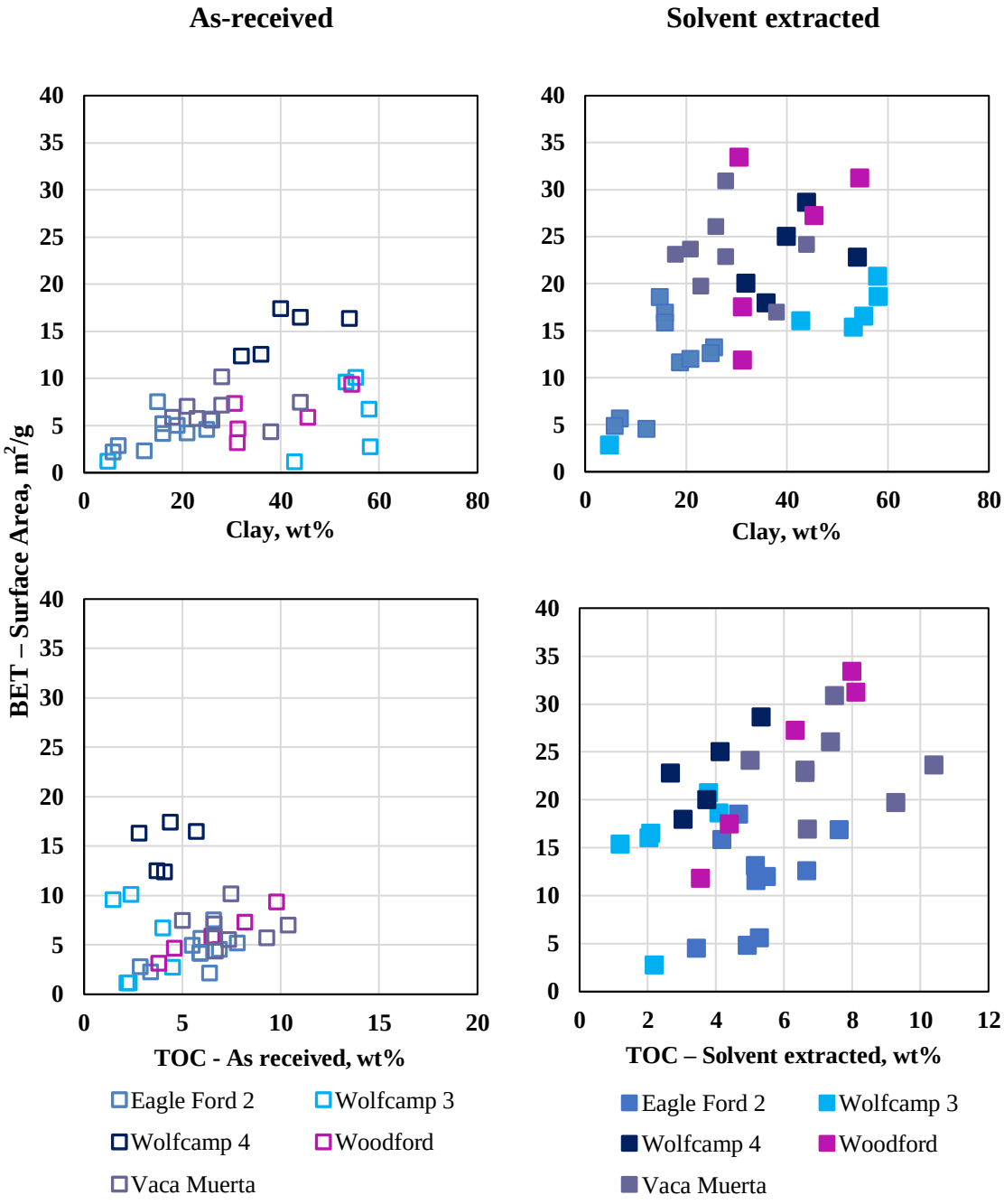

Fig. 43: Relationships between BET-surface area with clay and TOC for "as-received" and solvent extracted state for the condensate window (Eagle Ford 2-blue, Vaca Muerta-indigo, Wolfcamp 3-light blue, Wolfcamp 4-dark blue, Woodford-purple) shale samples.

4.7.4 Gas window

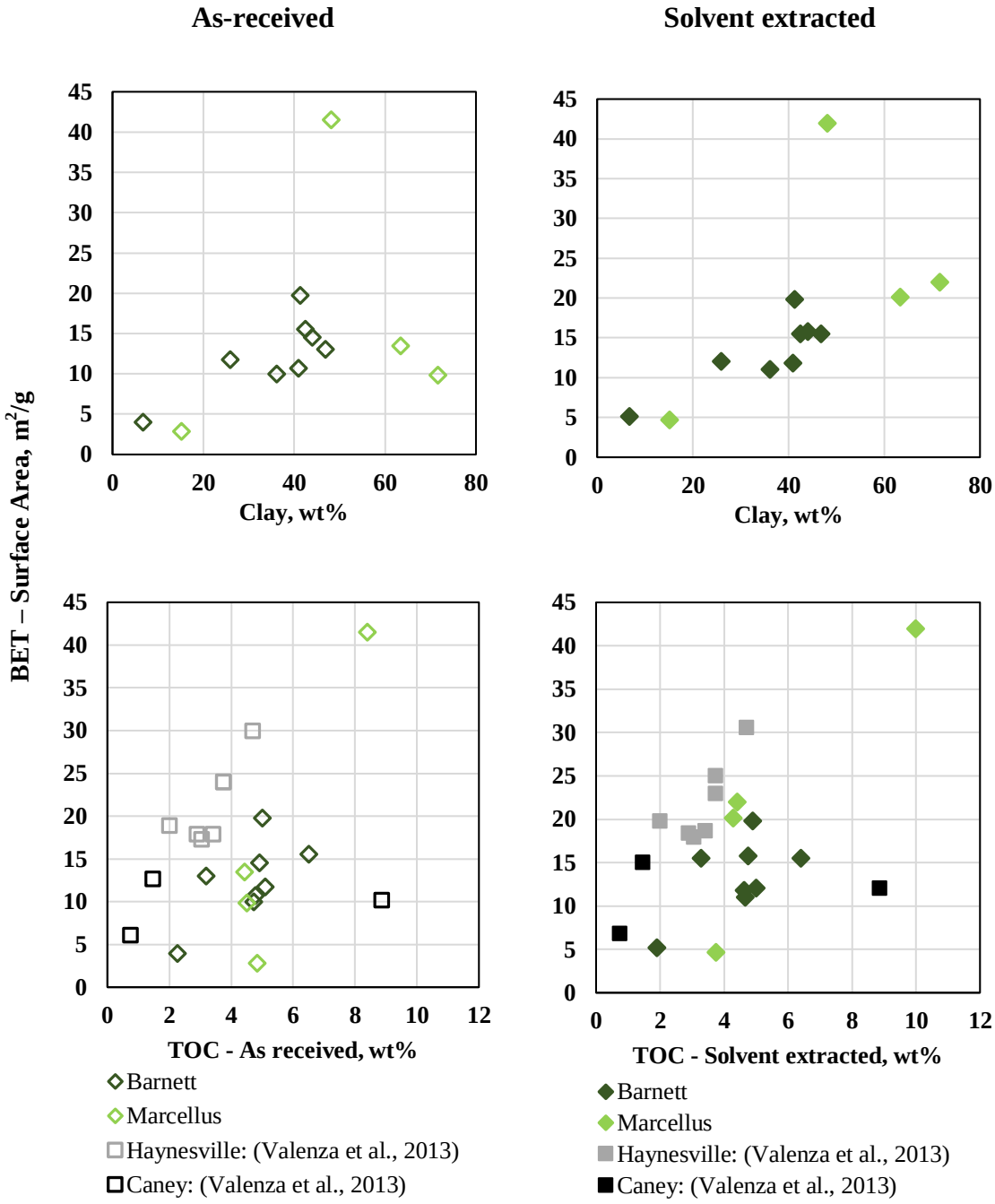

Fig. 44: Relationships between BET-surface area with clay and TOC, for "as-received" and solvent extracted state for the gas window (Barnett-dark green, Marcellus-light green) shale samples.

Based on the observations from **Fig. 41-44**, a positive correlation is observed between "solvent extracted" surface area and TOC. Surface area has a clay content dependence which is evident only after extraction. We observe a similar behavior between the BET – solvent extracted surface area and TOC content. The correlation between surface area and TOC in each maturity window becomes stronger post-extraction implying that the true surface area of a rock is restored to its original value by solvent extraction and that clay surface area are hidden by residual oil.

Wolfcamp 1 (immature) formation shales have low surface areas, this can be attributed to the fact that the kerogen nanopores are not well developed, which implies that the kerogens does not provide sufficient effective adsorption sites for gas adsorption leading to low surface area (1.13 m^2/g to 2.23 m^2/g). In addition, the clay content of these samples is low, leading to very limited surface area contribution from minerals. Gasprik et al. (2014) stated that the lower surface area values can be attributed to the fact that the pores may be occupied by bitumen and/or hydrocarbons which impedes the surface area estimation. Valenza et al. (2013) studied Haynesville and Caney shale samples from the gas window pre and post solvent extraction. Their results are reported in **Fig. 44** along with the results from our study.

Multi linear regression results post extraction are documented in **Table 6**. The coefficients for clay and TOC post extraction do not have a significant effect on the prediction of surface area ($p > 0.05$) in the immature window. Although, the p-value reduced for both the parameters, the higher reduction in p-value was observed for TOC

and also based on the coefficients the TOC shows a higher dependence on surface area over clay content. The weak positive correlation between the surface area and the TOC in the immature window can be attributed to the poor development of the OM pores. In case of oil, condensate and gas window the impact of solvent extraction leads to a strong prediction of surface area post extraction since the coefficents for both, clay and TOC have a very low p-value ($p < 0.005$). Further ahead, purely based on the coefficients of clay and TOC we can infer that TOC has a much stronger impact compared to clay.

Table 6: Statistical evaluation of TOC, clay and maturity on surface area post extraction.

Maturity	Predictor	Coefficients	p-value	Adjusted R^2
Immature	Clay	0.06	0.44	0.08
	TOC	0.33	0.16	
	Intercept	6.38	0.01	
Oil	Clay	0.19	$p < 0.05$	0.78
	TOC	1.69	$p < 0.05$	
	Intercept	2.20	0.19	
Condensate	Clay	0.33	$p < 0.05$	0.63
	TOC	2.25	$p < 0.05$	
	Intercept	-4.88	0.14	
Gas	Clay	0.29	$p < 0.05$	0.85
	TOC	4.06	$p < 0.05$	
	Intercept	-16.05	0.008	

Our results indicate that the thermal maturation can significantly affect the gas adsorption in organic rich shales; where gas adsorption is in the following order: Immature <Oil < Condensate <Gas. This relationship is the result of increased presence of small pores which is in agreement with Curtis et al. (2012), where they showed an increase in organic porosity for Woodford samples with increasing thermal maturity.

Post extraction we also tried to compare the inorganic surface area (total surface area – organic surface area) with the clay content to determine the dependence of the inorganic surface area with the total clay content. We did not observe any correlation between the two parameters which can be attributed to the following reasons:

1. While measuring the surface area of the sample, the organic surface area is underestimated due to the coating of the clay layers onto the organics, which inhibits accounting for all the organics contributing to the actual surface area of the rock.
2. The contribution from the inorganics may not be completely associated with the surface area from each of the individual clay minerals present due to the changes in the clay morphology.

Wang et al. (2013), Ross and Bustin (2009), Chalmers et al. (2012), Curtis et al. (2012) stated that the main factors controlling the organic pore structure are the type and amount of OM and the maturity of shale. Mastalerz et al. (2012) observed similar results for samples from gas shales. Our results show that TOC is the controlling factor in

determining the surface area in each maturity window and that the dependence becomes stronger as we move from the oil to the gas window (**Figs. 40-44 and Table 6**).

The comparison of BET-surface area pre- and post-extraction for the 10 wells grouped together by maturity is represented in the form of box and whisker plot, shown in **Fig. 45**. The results indicate that the maximum impact of Soxhlet extraction on surface area was in the immature window and the least in the gas window. This is also associated with increase in porosity as observed in **Fig. 21**. The average percentage change in BET surface area is approximately 175% in the immature window and 15% in the gas window.

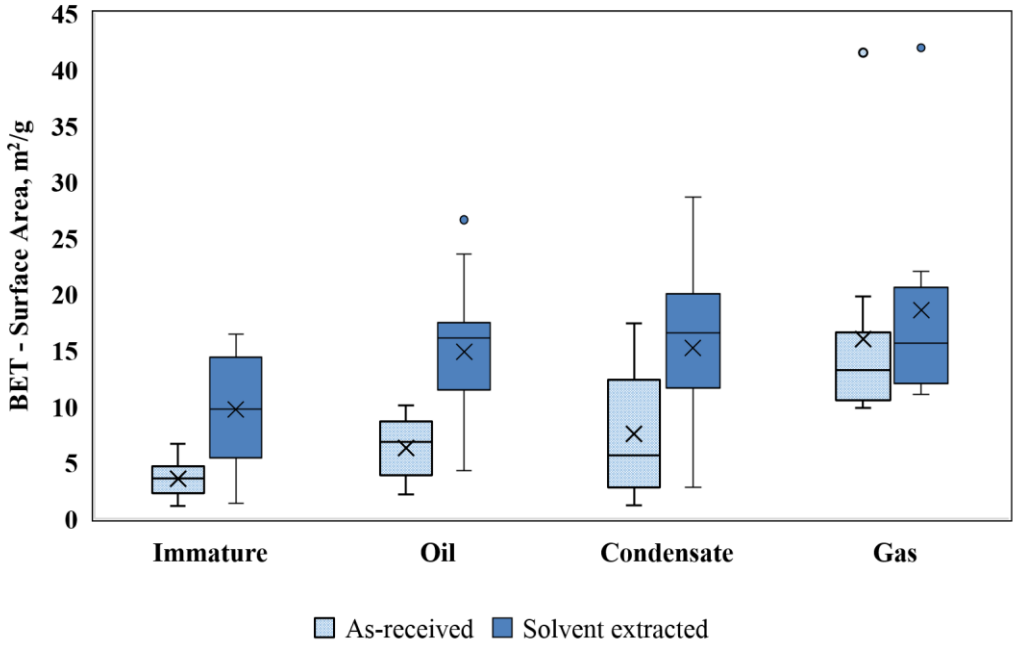

Fig. 45: Box and whisker plot for the 10 wells from six different shale formations showing the increase in surface area with increasing thermal maturity. The black cross marks shown in the figure are the mean values for each dataset. The average percentage increase in immature, oil, condensate, and gas window are 175%, 136%, 101% and 15% respectively.

4.8 Dependance of surface area on maturity of kerogens

Jarvie et al. (2007) and Schieber (2010) have suggested that the pores in OM are a result of the generation of oil and gas with increasing thermal maturity.

The previous section highlighted the impact of solvent extraction and the surface area after extraction as a function of maturity. In this section, we examine the response of the extracted kerogen. **Fig. 46** shows the plot of surface area with increasing thermal maturity for isolated kerogen from this study and literature (Cao et al., 2015; Rexer et al., 2014). The trend of increasing surface area with increasing maturity is similar to the pattern observed in the shale samples.

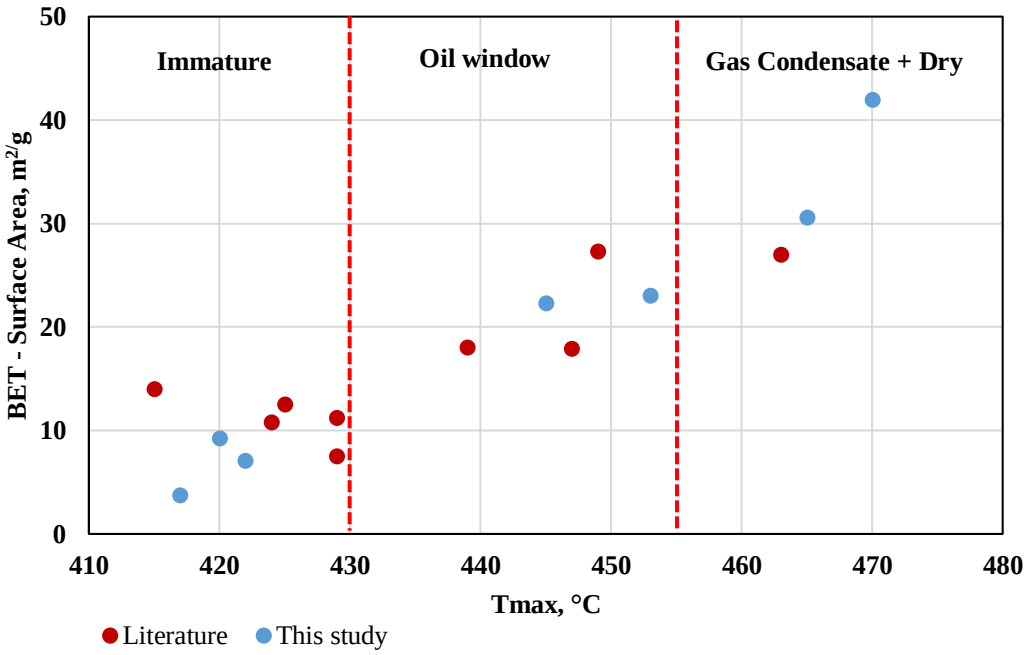

Fig. 46: Graphical representation of the data reported in Appendix B, Table 15. The graph consists of data points from this study (blue dots) and from the literature (Rexer et al., 2014; Cao et al., 2015; Hu et al., 2015; Wang et al., 2015) (red dots). The increasing trend observed in BET surface area with increasing maturity from immature to over mature is in agreement with the previous studies in the literature.

4.9 Economic Analysis

The increase in porosity post extraction is maximum in the immature and oil window and almost negligible in the gas window. This further confirms the importance of measuring the crushed helium porosity for liquid rich samples only after extraction. An example of the calculation of reserves based on the change in porosity in an oil and gas reservoir is shown below. **Table 7** consists of the parameters used for calculating the reserves.

Initial oil in place is given by:

$$N_i = \frac{7758 * A * h * \varphi * (1 - S_{wi})}{B_{oi}} \quad (17)$$

Initial gas in place is given by:

$$G_i = \frac{43560 * A * h * \varphi * (1 - S_{wr} - S_{gr})}{B_{gi}} \quad (18)$$

Table 7: Data for estimating the in place reserves for oil and gas reservoirs.

Area	160 acres
Net productive thickness	200 ft
Average S_{wi} for oil reservoir	50%
Average change in porosity for oil reservoir	3%
B_o at P_i	1.5 res bbl/STB
Average S_{gr} for gas reservoir	5%
Average S_{wr} for gas reservoir	30%
Average change in porosity for gas reservoir	1%

B_g at P_i	0.006 ft^3/SCF
Initial reservoir pressure	4000 psi

In this study we computed the change in OIP and GIP reserves based on the change in porosity in an oil and gas reservoir respectively. Based on the values given in **Table 7** the OIP reserves will be underestimated by 2 MM STB and the GIP will be underestimated by 1.5 MMM SCF.

4.10 Summary – Analysis of adsorption capacity of different shales.

Shale adsorption capacity was determined using nitrogen as the adsorbate. Adsorption capacity was measured on samples from different maturity formations across North America. TOC and maturity are the main factors influencing the specific surface area, other factors such as kerogen type, the dominant clay mineral type and moisture content play minor roles. Hao et al. (2013) summarized the list of factors affecting the gas adsorption in organic-rich shales. This study shows that the development of nanopores in kerogen leads to an increase in the adsorption capacity and hence the specific surface area with increasing TOC and maturity. This is verified when the immature shale (Wolfcamp 1 with low TOC) undergoes maturation to condensate (Wolfcamp 4 high TOC) and the obtained specific surface area increases. The adsorption capacity differs greatly between the same maturity window with different type of clay minerals present. Schettler and Parmoly (1990) argued that gas adsorption was primarily associated with illite, and the adsorption onto kerogen was of secondary importance for shale formation within the Appalachian Basin. They concluded that the clay minerals, dominated by illite, provide a large surface area and effective adsorption sites and can be the most important medium for gas adsorption. A plot of surface area with illite content in each maturity window is shown in **Fig. 39**. Our results show a similar trend as proposed by Schettler and Parmoly, with increasing illite content the surface area increased linearly, i.e. they have a weak positive correlation.

Chapter 5: Conclusions

We studied the effect of OM richness, maturity, and mineralogy on the adsorption capacity of organic rich shale using nitrogen as the adsorbate. The main conclusions are summarized as follows:

- Specific surface area increases with the increasing thermal maturity as result of maturation of the OM and generation of smaller and smaller nanopores.
- The specific surface area and porosity are strongly dependent on sample cleaning.
- Solvent extraction increases the porosity of the shale samples in the order of immature (93%) > oil (39%) > condensate (19%) > gas (10%).
- "Extra-porosity," recorded as the difference between "as received" and solvent extracted porosity, is directly related to the TOC.
- Solvent extraction using toluene and methanol opens additional pore space for N_2 adsorption thus, increasing the surface area multifold depending on the maturity window of the sample. The effect of solvent extraction on measured surface area is greatest in the lower maturity samples (175% in immature) and becomes systematically less as maturity increases (15% in gas).
- Comparing PSD curves for surface area pre- and post- extraction, a significant increase in contribution from the smaller mesopores (2 – 7 nm) was observed in the immature and oil window due to removal of mobile hydrocarbons.
- The relationships between the surface area (SA), clay content and TOC are masked in "as received" samples due to the coating of the soluble hydrocarbons onto the organic pores by almost a factor of 2 to 3.

- The relative abundance of micro– and fine mesopores in shales is controlled by both, the clay and the OM contents. An empirical correlation was developed for each maturity window based on the TOC and clay content and surface area **(see Table 6)**. The primary controlling factor for the adsorption capacity in shale is the TOC content at any maturity level and the correlation between TOC and surface area post extraction becomes stronger with increasing maturity.
- Comparison to historical data is questionable without a clear description of how the samples are treated or cleaned prior to the measurements.

Recommendation

In order to have a proper comparison of the data from lab to lab the samples must be cleaned and cleaning procedure must be stated.

References

Adesida, A. 2011. Pore Size Distribution of Barnett Shale using Nitrogen Adsorption Data. MS thesis, University of Oklahoma, Norman, Oklahoma.

Ambrose, R. J., Hartman, R. C., Diaz-Campos, M., Akkutlu, I. Y., and Sondergeld, C. H. 2010. New pore-scale considerations for shale gas in place calculations. Presented at SPE Unconventional Gas Conference, Pittsburgh, Pennsylvania, 23-25 February. SPE 131772.

Ambrose, R. J. 2011. Micro-Structure of Gas Shales and its Effect on Gas Storage and Production Performance. PhD Dissertation, University of Oklahoma, Norman, Oklahoma.

Ballard, D. B. 2007. Quantitative Mineralogy of Reservoir Rocks Using Fourier Transform Infrared Spectroscopy. Presented at SPE Annual Technical Conference and Exhibition, Anaheim, California, 11-14 November. SPE 113023.

Barrett, E. P., Joyner, L. G., and Halenda, P. P. 1951. The determination of pore volume and area distributions in porous substances: computations from nitrogen isotherms. Journal of the American Chemical society **73**: 373-380.

Barnes, G., and Gentle, I. 2005. Interfacial Science. Oxford University Press Oxford.

Bernard, S., Wirth, R., Schreiber, A., Schhulz, H.M., and Horsfield, B. 2012. Formation of nanoporous pyrobitumen residues during maturation of the Barnett Shale (Forth Worth Basin). International Journal of Coal Geology **103**, 3-11.

Boggs Jr, S. 2012. Principles of Sedimentology and Stratigraphy, 5th ed.: Upper Saddle River, New Jersey, Pearson Education, Ltd., 585 p

Bohacs, K. M. 1998. Contrasting Expressions of Depositional Sequences in Mudstones from Marine to Non-marine Environs, in Schieber, J., Zimmerle, W., and Sethi, P., Mudstones and Shales, Characteristics at the Basin Scale: Stuttgart, Schweizerbart'sche Verlagsbuchhandlung, **1**: 32-77.

Bohacs, K. M., Grabowski Jr, G. J., Carroll, A. R., Mankiewicz, P. J., Miskell-Gerhardt, K.J., Schwalbach, J. R., Wegner, M. B. and Simo, J. T. 2005. Production, Destruction, and Dilution—The Many Paths to Source-Rock Development. SEPM Special Publication **82**: 61-101.

Bowker, K.A. 2007. Barnett Shale gas production, Fort Worth Basin: Issues and discussion. AAPG Bulletin **91** (4): 523—533.

Brunauer, S., Emmett, P. H. and Teller, E. 1938. Adsorption of Gases in Multimolecular Layers. Journal of American Chemical Society **60**: 309-319.

Bustin, R. M., Bustin, A. M., Cui, X., Ross, D., Murthy, J. K., and Pathi, V. S. 2008. Impact of Shale Properties on Pore Structure and Storage Characteristics. SPE 119892. Presented at the SPE Shale Gas Production Conference, Fort Worth, Texas, USA, 16-18 November 2008. SPE 119892.

Cai, Y., Liu, D., Pan, Z., Yao, Y., Li, J. and Qui, Y. 2013. Pore structure and its impact on CH_4 adsorption capacity and flow capability of bituminous and sub-bituminous coals from Northeast China. Fuel 103: 258-268.

Cao, T. T., Song, Z. G., Wang, S. B., and Xia, J. 2015. A comparative study of the specific surface area and pore structure of different shales and their kerogens. Science China Earth Sciences **58** (4): 510-522.

Cases, J. M., Berend, I., Besson, G., Francois, M., Uriot, J. P., Thomas, F. and Poirier, J. E. 1992. Mechanism of adsorption and desorption of water vapor by homoionic montmorillonite. 1. the sodium-exchanged form. Langmuir **8**: 2730-2739.

Chalmers, G. R. L., and Bustin, R. M. 2007. The organic matter distribution and methane capacity of the Lower Cretaceous strata of Northeastern British Columbia, Canada. International Journal of Coal Geology, **70** (1-3): 223—239.

Chalmers, G. R., and Bustin, R. M. 2008. Lower Cretaceous gas shales in northeastern British Columbia, Part I: Geologic controls on methane sorption capacity. Bulletin of Canadian Petroleum Geology **56** (1): 1-21.

Chalmers, G. R., Bustin, R. M. and Power, I. M. 2012. Characterization of gas shale pore systems by porosimetry, pycnometry, surface area, and field emission scanning electron microscopy / transmission electron microscopy image analyses: Examples from the Barnett, Woodford, Haynesville, Marcellus, and doig units. AAPG Bulletin, **96:** 1099-1119.

Chen, H. J., Mehmani, A., Li, B.., Georgi, D., and Guodong, J. 2013. Estimation of Total Hydrocarbon in the Presence of Capillary Condensation for Unconventional Shale Reservoirs. Presented at the Middle East Oil and Gas Conference, Manama, Bahrain, 10-13 March. SPE-164468.

Clarkson, C. R. and Bustin, R. M. 1999. The effect of pore structure and gas pressure upon the transport properties of coal: a laborartory and modelling study. 1. Isotherms and pore volume distributions. Fuel **78** (11): 1333-1344.

Clarkson, C. R., Freeman, M., He, L., Agamalian, M., Melnichenko, Y. B., Mastalerz, M., Bustin, R. M., Radlinski, A. P. and Blach, T. P. 2012. Characterization of tight gas reservoir pore structure using USANS/SANS and gas adsorption analysis. Fuel **95**: 371-385.

Clarkson, C. R., Solano, N., Bustin, R. M., and Bustin, A. M. M. 2013. Pore structure characterization of North American shale gas reservoirs using USANS/SANS, gas adsorption, and mercury intrusion. Fuel **103***:* 606-616.

Condon, J. B. 2006. Surface Area and porosity Determinations by Physisorption Measurements and Theory. Elsevier Academic Press.

Cramer, D. D. 2008. Stimulating Unconventional Reservoirs: Lessons Learned, Successful Practices, Areas for Improvement. Presented at Unconventional Gas Conference, Keystone, Colorado, USA, 10-12 February. SPE 114172-MS.

Cui, X., Bustin, A. M., and Bustin, R. 2009. Measurements of gas permeability and diffusivity of tight reservoir rocks: different approaches and their applications. Geofluids **9**: 208-223.

Curtis, J. B. 2002. Fractured shale-gas systems. AAPG Bulletin **86**: 1921-1938.

Curtis, M. E., Ambrose, R. J., Sondergeld, C. H., and Rai, C. S., 2010. Structural Characterization of Gas Shales on the Micro- and Nano-Scales. Presented at the Canadian Unconventional Resources and International Petroleum Conference, Calgary, Alberta, Canada, 19-21 October. SPE-137693.

Curtis, M. E., Cardott, B. J., Sondergeld, C. H., and Rai, C. S. 2012. Development of organic porosity in the Woodford shale with increasing thermal maturity. International Journal of Coal Geology **103** (1): 26-31.

Do, D. D. and Do, H. D. 2003. Pore Characterization of Carbonaceous materials by DFT and GCMC simulations: A Review. Adsorption Science Technology **21**: 389-423.

Durand, B. 1980. Kerogen: Insoluble Organic Matter from Sedimentary Rocks. Editions TECHNIP, Jan 1, 1980, Paris.

Folk, R. L., 1974. Petrology of Sedimentary Rocks, Hemphill Publishing Company.

Friedman, G. 2003. Classification of Sedimentary Rocks. In G. V. Middleton (Ed.), Encylopedia of sediments and sedimentary rocks Kluwer Academic encyclopedia of earth sciences series. Dordrecht, The Netherlands, Boston: Kluwer Academic Publishers.

Fu, H., Wang, X., Zhang, L., Gao, R., Li, Z., Xu, T., Zhu, X., Xu, W., and Li, Q. 2015. Investigation of the factors that control the development of pore structure in lacustrine shale: A case study of the block X in the Ordos Basin, China. Journal of Natural Gas Science and Engineering **26**: 1422-1432.

Furmann, A., Mastalerz, M., Brassell, S. C., Schimmelmann, A., and Picardal, F. 2013. Extractability of biomarkers from high- and low- vitrinite coals and its effect on the porosity of coal. International Journal of Coal Geology **107**: 141-151.

Gan, H., Nandi, S.P., and Walker Jr, P.L. 1972. Nature of the porosity in American coals. Fuel **51** (4): 272—277.

Gasparik, M., Bertier, P., Gensterblum, Y., Ghanizadeh, A., Krooss, B. M., and Little, R. 2014. Geologic Controls on the Methane Storage Capacity in Organic-Rich Shales. International Journal of Coal Geology 1**23**: 34-51.

Ghanizadeh, A., Clarkson, C.R., Aquino, A., and Vahedian, A. 2015. Impact of Solvent-Extraction on Fluid Storage and Transport Properties of Montney Formation. Presented at the Unconventional Resources Conference, Calgary, Canada, 30 October—2 November. SPE-175954.

Giesche, H. 2006. Mercury Porosimetry: A General (Practical) Overview. Particle and Particle System Characterization **23** (1): 9-19.

Gregg, S. J., and Sing, K. S. W. 1982. Adsorption, Surface Area, and Porosity. 2nd edition. New York: Academic Press, New York.

Groen, J. C., Peffer, L. A. A., and Perez-Ramirez, J. 2003. Pore size determination in modified micro- and mesoporous materials. Pitfalls and limitations in gas adsorption data analysis. Microporous and Mesoporous materials **60**: 1-17.

Guo, W., Xiong, W., Gao, S. S., Hu, Z. M., Liu, H. L., and Yu, R. Z. 2013. Impact of temperature on the isothermal adsorption/desorption characteristics of shale gas. Petroleum Exploration and Development, 40: 514-519.

Gupta, I., Rai, C., Tinni, A., and Sondergeld, C. 2017. Impact of Different Cleaning Methods on Petrophysical Measurements. Presented at SPWLA 58th Annual Logging Symposium, Oklahoma City, Oklahoma, 17-21 June.

Guthrie, J. M., and Bohacs, K. M. 2009. Spatial Variability of Source Rocks: A Critical Element for Defining the Petroleum System of Pennsylvanian Carbonate Reservoirs of the Paradox Basin, SE Utah. Paradox Basin 95-130.

Halsey, G. D. 1948. Physical Adsorption on Non-Uniform Surfaces. Journal of Chemical Physics, **16** (10): 931-937.

Hao, F., Zou, H. Y., and Lu, Y. C. 2013. Mechanisms of shale gas storage: Implications for shale gas exploration in China. AAPG Bulletin, **97**: 1325-1346.

Harkins, W. D., and Jura, G. 1944. Surfaces of Solids. XII. An Absolute Method for the Determination of the Area of Finely Divided Crystalline Solid. Journal of American Chemical Society, **66** (8): 1362-1366.

Hossain, Z., Grattoni, C. A., Solymar, M., and Fabricius, I. L., 2011. Petrophysical properties of greensand as predicted from NMR measurements: Journal of Petroleum Geoscience **17**: 111-125.

Hou, Y., He, Sheng., Yi, J., Zhang, B., Chen, X., Wang, Y., Zhang, J., Cheng, C. 2014. Effect of pore structure on methane sorption potential of shales. Petroleum Exploration and Development, **41** (2): 272-281.

Howard, J. J., 1991. Porosimetry measurement of shale fabric and its relationship to Illite/Smectite Diagenesis. Journal of Clays and Clay Minerals **39** (4): 355-361.

Hunt, J. M. 1996. Petroleum Geochemistry and Geology. 2nd edition. USA. W. H. Freeman and Company.

IUPAC. 1985. Pure & Applied Chemistry **57** (4): 603-619, Great Britain.

Jarvie, D. M. 1991. Total Organic Carbon (TOC) Analysis in Treatise of Petroleum Geology: Handbook of Petroleum Geology: Source and Migration Processes and Evaluation Techniques. AAPG Press, Tulsa, USA.

Jarvie, D. M., Hill, R. J., Ruble, T. E., and Pollastro, R. M., 2007. Unconventional shale-gas systems: The Mississippian Barnett Shale of north-central Texas as one model for thermogenic shale-gas assessment. AAPG Bulletin, **91** (4), 475-499.

Jiang, T., Rylander, E., Singer, P. M., Lewis, R. E., and Sinclair, S. M. 2013. Integrated Petrophysical Interpretation of Eagle Ford Shale with 1-D and 2-D Nuclear Magnetic Resonance (NMR). Presented at SPWLA 54th Annual Logging Symposium, New Orleans, LA, 22-26 June.

Kale, S. 2009. Petrophysical Characterization of Barnett Shale Play. MS thesis, University of Oklahoma, Norman, Oklahoma.

Karastathis, A. 2007.Petrophysical Measurements on Tight Gas Shale. MS thesis, University of Oklahoma, Norman, Oklahoma.

Katsube, T. J., Cox, W. C., and Issler, D. R. 1998. Porosity characteristics of shale formations from the Western Canadian Sedimentary Basin. Geological Survey of Canada. Pp. 63-74.

Kuila, U., and Prasad, M. 2013. Specific surface area and pore-size distribution in clays and shales. Geophysics Prospect **61**: 341-362.

Kuila, U., McCarty, D. K., Derkowski, A., Fischer, T. B., and Prasad, M., 2014a. Total porosity measurement in gas shales by the water immersion porosimetry (WIP) method: Journal of Fuel, **117** (Part B): 1115-1129.

Kuila, U., McCarty, D. K., Derkowski, A., Fischer, T. B., Topor, T., and Prasad, M., 2014b. Nano-scale texture and porosity of organic matter and clay minerals in organic-rich mudrocks. Fuel, **35**: 359-373.

Labani, M. M., Rezaee, R., Saeedi, A., and Hinai, A. A. 2013. Evaluation of pore size spectrum of gas shale reservoirs using low pressure nitrogen adsorption, gas expansion and mercury porosimetry: A case study from the Perth and Canning Basins, Western Australia. Journal of Petroleum Science and Engineering **112:** 7-16.

Lemmens, H. J., Butcher, A. R., and Botha, P., 2011. FIB/SEM and SEM/EDX: A New Dawn for the SEM in the Core Lab?. International Symposium of the Society of Core Analysts, Paper SCA2010-08.

Li, T., Tian, H., Chen, J., and Cheng, L. 2016. Application of Low Pressure Gas Adsorption to the Characterization of Pore Size Distribution of Shales: An example from Southeastern Chongqing area, China. Journal of Natural Gas Geoscience **1**: 221-23.

Lippens, B. C., and de Boer, J. H. 1965. Studies on Pore Systems in Catalysts: V. The t-method. Journal of Catalysis **4** (3): 319-323.

Liu, D., Yuan, P., Liu, H., Li, T., Tan, D., Yuan, W., and He, H. 2013. High pressure adsorption of methane on montmorillonite, kaolinite and illite. Applied Clay Science, **85**: 25-30.

Loucks, R. G., Reed, R. M., Ruppel, S., and Jarvie, D. M. 2009. Morphology, Genesis, and Distribution of Nanometer-Scale Pores in Siliceous Mudstones of the Mississippian Barnett Shale: Journal of Sedimentary Research **79** (12), 848-861.

Loucks, R. G., Reed, R. M., Ruppel, S. C., and Hammes, U. 2012. Spectrum of Pore Types and Networks in Mudrocks and Descriptive Classification for Matrix related Mudrocks Pores. AAPG Bulletin, **96** (6): 1071-1098.

Lowell, S. Introduction to Powder Surface Area. 1979. John Wiley and Sons, New York.

Lowell, S. 2006. Characterization of Porous Solids and Powders: Surface area, Pore size and Density, first edition. Springer.

Lu, X. C., Li, F. C., and Watson, A. T. 1995.Adsorption measurements in Devonian shales. Fuel **74**: 599-603.

Macht, F., Eusterhues, K., Pronk, G.J., and Totsche, K.U. 2011. Specific surface area of clay minerals: Comparison between atomic force microscopy measurements and bulk-gas (N_2) and –liquid (EGME) adsorption methods. Applied Clay Science **53**: 20-26.

Mastalerz, M., He, L., Melnichenko, B. Y., and Ruppa, J. A. 2012. Porosity of coal and shale: Insights from gas adsorption and SANS/USANS techniques. Energy and Fuels **26**: 5109-5120.

Mastalerz, M., Schimmelmann, A., Drobniak, A., and Chen, Y. 2013. Porosity of Devonian and Mississippian New Albany Shale across a maturation gradient: insights from organic petrology, gas adsorption, and mercury intrusion. AAPG Bulletin **97** (10), 1621-1643.

Matthews, G. Peter, Cathy J. Ridgway, and Michael C. Spearing. 1995. Void space modeling of mercury intrusion hysteresis in sandstone, paper coating, and other porous media. Journal of Colloid and Interface Science **171** (1): 8-27.

McCarthy, K., Rojas, K., Niemann, M., Palmowski, D., Peters, K., and Stankiewicz, A. 2011. Basic Petroleum Geochemistry for Source Rock Evaluation, Oil field Review, Schlumberger.

Milliken, K. L., Rudnicki, M., Awwiller, D. A., and Zhang, T. 2013. Organic matter-hosted pore system, Marcellus Formation (Devonian), Pennsylvania. AAPG Bulletin **97**: 177-200

Montgomery, S. L., Jarvie, D. M., Bowker, K. A., and Pollastro, R. M. 2005. Mississippian Barnett Shale, Fort Worth Basin, north-central Texas: gas-shale play with multi-trillion cubic foot potential, AAPG Bulletin **89**, 155-175.

Nelson, P. 2009. Pore throat sizes in sandstones, tight sandstones and shales. AAPG Bulletin **93** (3): 329-340.

Nimmo, J. R. 2004. Porosity and pore size distribution. Encyclopedia of Soils in the Environment., (pp. 295–303)

Passey, Q. R., Bohacs, K. M., Esch, W. L., Klimentidis, R., and Sinha, S. 2010. From Oil-Prone Source Rock to Gas-Producing Shale Reservoir – Geologic and Petrophysical Characterization of Unconventional Shale-Gas Reservoirs. Presented at CPS/SPE International Oil & Gas Conference and Exhibition in China, Beijing, China, 8-10 June. SPE 131350.

Potter, P. E., Maynard, J. B. and Depetris, P. J. 2005. Mud and Mudstones: Introduction and overview: Berlin, Germany, Springer, 304 p.

Reed, R., and Loucks, R. 2007. Imaging Nanoscale Pores in the Mississippian Barnett Shale of the Northern Fort Worth Basin. AAPG Annual Convention Abstracts, v. 16. Search and Discovery Article 90063.

Rexer, T. F., Mathia, E. J., Aplin, A. C and Thomas, K. M. 2014. High-Pressure Methane Adsorption and Characterization of Pores in Posidonia Shales and Isolated Kerogens. Energy and Fuels, **28**: 2886-2901.

Rivera, S., Saidian, M., Godinez, L. J., and Prasad, M. 2014. Effect of Mineralogy on NMR, Sonic and Resistivity: A Case Study of the Monterey Formation. Presented at the Unconventional Resources Technology Conference, Denver, Colorado, 25-27 August. URTeC 1922872.

Rouquerol, J., Avnir, D., Everett, D. H., Fairbridge, C., Haynes, M., Pernicone, N., Ramsay, J. D.F., Sing, K. S. W., and Unger, K. K. 1994. Guidelines for the characterization of porous solids. Studies in surface science and catalysis, **87**: 1 – 9.

Rouquerol, J., Rouquerol, F., and Sing, K. S. W. 1998. Absorption by powders and porous solids. Academic Press.

Rouquerol, J., Llewellyn, P., and Rouquerol, F. 2007. Is the BET equation applicable to microporous adsorbents? Studies in Surface Science and Catalysis, **160**: 49–56.

Ross, D. J. K., and Bustin, R. M. 2007. Shale gas potential of the Lower Jurassic Gordondale Member, northeastern British Columbia, Canada. Bulletin of Canadian Petroleum Geology **55**: 51-75

Ross, D. J. K., and Bustin, R. M. 2008. Characterizing the shale gas resource potential of Devonian-Mississippian strata in the Western Canada Sedimentary Basin; application of an integrated formation evaluation. American Association of Petroleum Geologists Bulletin **92**: 87-125.

Ross, D. J. K., and Bustin, R. M. 2009. The importance of shale composition and pore structure upon gas storage potential of shale gas reservoirs. Marine and Petroleum Geology **26**: 916-927.

Saidian, M., Kuila, U., Prasad, M., Alcantar-Lopez, L., Rivera, S., and Godinez, L. 2015. A Comparison of Measurement Techniques for Porosity and Pore Size Distribution in Shales (Mudrocks): A Case Study of Haynesville, Eastern European Silurian, Niobrara, and Monterey Formations. AAPG Memoir 110: 60.

Schettler, P. D. and Parmoly, C, R. 1990. The measurement of gas adsorption isotherms for Devonian shale. GRI Devonian Gas Shale Technology Review **7**: 4-9.

Schmitt, M., Fernandes, C. P., da Cunha Neto, J, A. B., Wolf, F. G., dos Santos, V. S. S. 2013. Characterization of pore systems in seal rocks using Nitrogen Gas Adsorption combined with Mercury Injection Capillary Pressure techniques. Marine and Petroleum Geology **39** (1): 138-149.

Schieber, J. 2010. Common themes in the formation and preservation of intrinsic porosity in shales and mudstones-Illustrated with examples across the Phanerozoic. Presented at SPE Unconventional Gas Conference in Pittsburgh, Pennsylvania, USA, 23-25 February. SPE 132370

Sigal, R. F. 2009. A Methodology for Blank and Conformance Corrections for High Pressure Mercury Porosimetry. Measurement Science and Technology **20** (4): 1-11.

Sing, K. S. W., Everett, D. H., Haul, R. A. W., Moscou, L., Peirotti, R. A., and Rouquerol, J. 1985. IUPAC commission on colloid and surface chemistry including catalysis. Pure and Applied Chemistry **57**: 603-619.

Slatt R. M., and O'Brien, N. R. 2011. Pore types in the Barnett and Woodford gas shales: contribution to understanding gas storage and migration pathways in fine-grained rocks. AAPG Bulletin **95** (12): 2017-2030.

Sondergeld, C. H., and Rai, C. S. 1993. A New Concept of Quantitative Core Characterization. The Leading Edge **12** (7): 774-779.

Sondergeld, C., Ambrose, R. J., Rai, C. S. and Moncrieff, J. 2010a. Microstructural studies of gas shales: Presented at the SPE Unconventional Gas Conference, Pittsburgh, Pennsylvania, 23-25 February. SPE 131771.

Sondergeld, C., Newsham, K., Comisky, J., Rice, M., and Rai, C. 2010b. Petrophysical considerations in evaluating and producing shale gas resources. Presented at SPE Unconventional Gas Conference, Pittsburgh, Pennsylvania, USA, 23-25 February. SPE 131768.

Sondhi, N. and Solano, L. P. 2009. Application of Thermogravimetric and Fourier Transform Infrared Spectroscopy Analysis in Determining Heating Protocols for Porosity Measurements in Shales. Presented at SPWLA 50th Annual Logging Symposium, Houston, Texas, 21-24 June.

Tian, H., Pan, L., Xiao, X. M., Wilkins, R. W. T., Meng, Z. P., and Huang, B. J. 2013. A preliminary study on the pore characterization of Lower Silurian black shales in the Chuandong Thrust Fold Belt, southwestern China using low pressure N_2 adsorption and FE-SEM methods. Marine and Petroleum Geology **48**: 8-119.

Valenza, J. J., Drenzek, N., Marques, F., Pagels, M., and Mastalerz, M. 2013. Geochemical controls on shale microstructure. Geology **41**: 611-614.

Wang, F. P. and Reed, R. M. 2009. Pore Networks and Fluid Flow in Gas Shales. Presented at the SPE Annual Technical Conference and Exhibition, New Orleans, Louisiana, USA, 4-7 October. SPE-124253.

Wang, S. B., Song, Z. G., and Cao, T. T. 2013. The methane sorption capacity of Paleozoic shales from the Sichuan Basin, China. Marine Petroleum Geology **44**: 112-119.

Wang, R., Zhang, N., Liu, X., Wu, X., Chen, J and Ma, L. 2015. Characteristics of Pore Volume Distribution and Methane Adsorption on Shales. Adsorption Science and Technology **33** (10): 915-937.

Webb, P. A. and Orr, C. 1997. Analytical Methods in Fine Particle Technology. Micromeritics Instrument Corporation Publishers, Norcross, GA, USA.

Wei, L., Mastalerz, M., Schimmelmann, A., and Chen, Y. 2014. Influence of Soxhlet-extractable bitumen and oil on porosity in thermally maturing organic-rich shales. International Journal of Coal Geology **132**: 38-50.

Wood, J.M., Sanei, H., and Curtis, M.E., and Clarkson, C. R. 2015. Solid bitumen as a determinant of reservoir quality in an unconventional tight gas siltstone play. International Journal of Coal Geology **150**: 287-295.

Zhang, T., Ellis, G. S., Ruppel, S. C., Milliken, K., and Yang, R. 2012. Effect of organic matter type and thermal maturity on methane adsorption in shale-gas systems. Organic Geochemistry **47***:* 120-131.

Zhu, R. K., Bai, B., Cui, J. W., Wu, S., Cui, J., and Wang, T. 2013. Research advances of microstructure in unconventional tight oil and gas reservoirs. Journal of Palaeogeography, **15** (5): 615-23.

Appendix A: Experimental Procedure

1. Nitrogen Adsorption Procedure

Prior to the adsorption analysis, the following steps were followed:

Step 1: Crush the core sample and sieve it to pass through a screen of 35 mesh and mix it thoroughly for uniformity.

Step 2: Heat the sample in an oven at 100°C for 24 hours.

Step 3: Sample tube, which is sonicated, washed and dried in oven for 4 hours is weighed empty with a rubber cap.

Step 4: Put approximately 1-2 grams of crushed sample into the sample tube and cover with the rubber cap. The sample tube is weighed again

Step 5: The sample tube along with the crushed sample is put in the degassing port and degassed for 12 hours at 100°C under vacuum to remove any moisture or volatile matter if any.

Step 6: After 12 hours of degassing the sample tube along with the rubber cap is weighed again and the weight loss is noted.

Step 7: The degassed sample/tube with the filler rod and isothermal jacket is put in the analysis port.

Step 8: The Dewar flask is filled with liquid Nitrogen

Step 9: The empty tube weight, degassed sample weight, N_2 characteristics are entered in the analysis software.

Step 10: The measurement and analysis starts automatically after equilibrium is attained through the instruments computer software.

2. Transmittance FTIR Mineralogy

In this study, the mineralogical estimation was done using the FTIR technique proposed by Sondergeld and Rai (1999) and Ballard, (2007). Sixteen commonly found minerals in sedimentary rocks are quantified using this technique. These minerals are quartz, calcite, dolomite, siderite, aragonite, illite, smectite, kaolinite, chlorite, mixed clay, oligoclase feldspar, orthoclase feldspar, albite, pyrite, apatite and anhydrite. Mineralogy was determined after removing the organic matter. The organic natter was removed using a low temperature plasma asher (Kale 2009).

3. Total Organic Carbon Determination

The weight percent of organic matter (OM) in a rock sample is given by 'Total Organic Carbon' or TOC. TOC is composed of three components namely, the extractable organic matter (EOM), the convertible carbon and the residual carbon fraction (Jarvie, 1991).

The Leco C844 machine was used for measuring the organic carbon content. The experiment was conducted after the crushed sample (particle size $\leq$ 35 mesh) was treated with HCl to remove any inorganic carbonate present. Thereafter, the sample was placed in the Leco Carbon Analyzer where the carbon in the sample is oxidized to carbon dioxide by the combustion of organic carbon in a pure stream of oxygen. The gas stream then passes through an infrared (IR) detector or thermal conductivity detector (TCD) which determines the amount of CO_2 produced.

4. SRA™

Pyrolysis is used to quantify the organic carbon content as well as to establish the type of kerogen present inside the rock and the thermal maturity of the sample. Source Rock Analyzer™ (SRA) by Weatherford Laboratories was used to carry out the dry pyrolysis measurements.

Procedure:

A small amount (< 1 g) of sample ground to 35 mesh undergoes a programmed temperature heating in a pyrolysis oven. The sample is first heated to 300^0C for 3 minutes and held constant to volatilize the free hydrocarbons present in the sample. The flame ionization detector (FID) records the first peak and quantifies it as S_1 which is denoted in mg of hydrocarbon per gram of rock. Temperature is then increased at 25^0C/minute to 600^0C. This leads to cracking of kerogen in the rock sample which results in generation of hydrocarbons and is called the generative potential of the rock. FID quantifies this peak as S_2 and is denoted in mg of hydrocarbons per gram of rock. S_2 peak is used to determine Hydrogen Index (HI) of the sample which is measured in terms of mg of hydrocarbon in S_2 per gram of TOC (S_2×100/TOC). The temperature associated with the peak of S_2 is called Tmax and is the measure of organic thermal maturity. During cool down i.e. between 300-400°C, the trapped CO_2 is released resulting in a third peak S_3 which is determined using the infrared detectors. S_3 is used to determine Oxygen Index (OI) of the sample which is expressed as the ratio of mg of CO_2 in S_3 per gram of TOC (S_3×100/TOC). Knowing the HI and OI and using the Van Krevelen diagram, the kerogen type can be determined (Hunt 1996).

5. Scanning Electron Microscopy

The SEM was used to visualize the pore structures of the shale samples. To better view the pore type and the pore microstructure within shales, we performed broad beam argon ion milling on samples from Bakken, Wolfcamp and Marcellus formation to obtain a highly-polished surface (Loucks et al., 2009; Sondergeld et al., 2010b; Curtis et al., 2012). The imaging of nanopores was performed on the surfaces prepared by argon ion milling using an accelerating voltage of 30 kV and a milling time of 4 hours. Curtis et al. (2010), Slatt and O'Brien (2011), Milliken et al. (2013) concluded imaging the samples can provide important information on the variation of pore types, pore size, pore microstructure and general locations of pores throughout the sample.

The samples are imaged in the back scattered mode at various magnifications to quantify the effect of solvent extraction on different maturity windows. The sample preparation procedure is in accordance with Curtis et al. (2012).

6. Kerogen isolation procedure

The procedure followed to isolate the kerogen from the rock samples is described below:

Step 1: The shale samples were crushed and sieved for uniformity to pass through a screen of 35 mesh (500 µm).

Step 2: The sample was treated with chloroform to remove any free hydrocarbons and bitumen. The obtained sample was then dried in an oven at 100°C.

Step 3: The sample is then treated with 6M HCl acid to remove the carbonate minerals.

Step 4: The sample was then treated twice with 6M HCl + 48% HF acid to eliminate the presence of any siliceous mineral.

Step 5: The obtained sample was treated with 6M HCl acid again to remove any newly formed complex fluorides.

Step 6: The treated sample was again cleaned with chloroform to remove any newly freed HC's and bitumen during this process. The final product obtained is kerogen with small amount of pyrite.

7. Derivation for Extra Porosity

$$\boldsymbol{\varphi_{clean} = \varphi_{native} + \varphi_{extra}}$$

$$\boldsymbol{\varphi_{extra} = \frac{\rho_{grain\ clean} - \rho_{grain\ native}}{\rho_{grain\ clean} - \rho_{bitumen}} (1 - \varphi_{native})}$$

$$\boldsymbol{\frac{V_{bitumen}}{V_{grain\ native}} = \frac{\rho_{grain\ clean} - \rho_{grain\ native}}{\rho_{grain\ clean} - \rho_{bitumen}}}$$

$$\boldsymbol{\frac{V_{grain\ native}}{V_{bulk}} = 1 - \varphi_{native}}$$

$$\boldsymbol{\frac{V_{bitumen}}{V_{bulk}} = \frac{\rho_{grain\ clean} - \rho_{grain\ native}}{\rho_{grain\ clean} - \rho_{bitumen}} (1 - \varphi_{native})}$$

Appendix B: Sample Description

Table B- 1: Lower Bakken – Mineralogy, TOC, Porosity and Surface area (Immature)

Depth	Clay wt%	Carbonate wt%	TOC Native wt%	Porosity Native %	Surf. Area Native m^2/g	Surf. Area Clean m^2/g
xx561	11	33	10.7	3.5	4.3	16.17
xx537	9	40	6.3	4	3.86	9.62
xxx57	33	9	11.9	3.5	4.84	13.94
xxx29	17	20	15.5	3.5	4.43	13.5
xxx61	3	37	0.2	6.13	3.55	5.39
xxx65	15	21	9.9	5.53	5.57	15.73
xxx29	23	18	14.2	3.5	3.71	10.06
xxx33	16	21	15.0	3.5	4.68	16.44
xxx69	39	5	8.6	3.5	6.64	15.99
xxx29	57	6	13.2	2.66	2.74	10.98
xxx35	36	8	12.6	3.02	3.18	8.25
xxx55	38	9	11.2	2.82	3.32	10.21
xxx59	22	10	9.3	3.39	3.04	8.74
xxx29	31	3	14.3	3.37	1.91	14.39
xxx59	23	3	16.0	3.49	2.97	6.26
xxx68	55	3	7.2	3.40	5.73	15.7

Table B- 2: Wolfcamp 1 – Mineralogy, TOC, Porosity and Surface area (Immature)

Depth	Clay wt%	Carbonate wt%	TOC Native wt%	Porosity Native %	Surf. Area Native m^2/g	Surf. Area Clean m^2/g
xx97	14	25	1.6	7.70	2.23	5.24
xx74	22	14	1.8	3.95	3.71	4.01
xx76	10	29	0.9	2.42	1.43	2.35
xx28	29	29	4.3	1.65	1.76	7.22
xx39	25	35	7.8	2.12	1.43	2.2
xx52	11	56	3.6	1.30	1.13	1.34
xx59	25	6	1.0	8.02	4.99	9.73

Table B- 3: Wolfcamp 2 – Mineralogy, TOC, Porosity and Surface area (Oil)

Depth	Clay wt%	Carbonate wt%	TOC Native wt%	Porosity Native %	Surf. Area Native m^2/g	Surf. Area Clean m^2/g
xx92	71	3	3.1	7.59	9.93	16.96
xx16	62	4	3.8	7.77	8.66	17.18
xx19	63	4	2.1	8.96	8.61	14.86
xx31	39	16	2.9	7.32	9.39	17.45
xx37	56	8	2.8	6.86	8.51	16.36
xx61	57	5	3.1	7.40	10.06	19.81

xx30	61	4	5.3	8.27	9.63	26.6
xx39	50	5	7.9	8.17	6.72	23.56
xx72	44	16	2.6	5.87	8.62	15.75

Table B- 4: Eagle Ford 1 – Mineralogy, TOC, Porosity and Surface Area (Oil)

Depth	**Clay wt%**	**Carbonate wt%**	**TOC Native wt%**	**Porosity Native %**	**Surf. Area Native m^2/g**	**Surf. Area Clean m^2/g**
xx598	23	69	3.0	7.23	6.89	11.15
xx603	33	54	2.6	6.69	6.91	13.60
xx626	11	82	3.2	4.57	3.87	6.26
xx650	23	69	1.6	5.37	3.96	5.92
xx690	10	85	1.9	5.82	2.13	4.29
xx767	6	84	2.3	3.14	3.87	9.37
xx798	6	86	13.4	3.96	2.72	12.40
xx817	9	76	15.0	4.65	4.52	17.45
xx824	9	76	14.2	4.86	3.08	16.72
xx834	16	72	11.2	5.47	4.36	14.26

Table B- 5: Wolfcamp 3 – Mineralogy, TOC, Porosity and Surface area (Condensate)

Depth	Clay wt%	Carbonate wt%	TOC Native wt%	Porosity Native %	Surf. Area Native m^2/g	Surf. Area Clean m^2/g
xx393	43	12	2	6.63	7.62	16.05
xx425	55	11	1.6	10.42	10.06	16.55
xx499	53	15	1.2	7.22	9.56	15.37
xx527	58	6	4.0	8.40	6.68	20.75
xx536	58	10	3.5	10.49	2.68	18.62
xx580	5	77	1.1	3.42	1.15	2.80

Table B- 6: Wolfcamp 4 – Mineralogy, TOC, Porosity and Surface area (Condensate)

Depth	Clay wt%	Carbonate wt%	TOC Native wt%	Porosity Native %	Surf. Area Native m^2/g	Surf. Area Clean m^2/g
xx68	44	23	5.7	10.99	16.45	28.66
xx94	40	30	4.4	9.01	17.36	25.00
xx11	36	17	3.7	7.04	12.48	17.96
xx63	32	23	4.1	7.53	12.34	20.00
xx028	54	7	2.8	10.77	16.28	22.79

Table B- 7: Woodford – Mineralogy, TOC, Porosity and Surface area (Condensate)

Depth	Clay wt%	Carbonate wt%	TOC Native wt%	Native Porosity %	Surf. Area Native m^2/g	Surf. Area Clean m^2/g
xxx13	31	21	2.2	6.97	2.54	2.64
xxx56	50	9	7.5	6.06	4.49	5.1
xxx90	31	12	3.8	4.97	3.12	11.83
xxx22	55	9	9.8	7.8	9.29	31.24
xxx45	46	8	6.5	5.7	5.84	27.23
xxx56	31	10	8.2	8.21	7.26	33.42
xxx62	31	13	4.6	6.74	4.61	17.51

Table B- 8: Barnett – Mineralogy, TOC, Porosity and Surface area (Gas)

Depth	Clay wt%	Carbonate wt%	TOC Native wt%	Native Porosity %	Surf. Area Native m^2/g	Surf. Area Clean m^2/g
xx57	7	91	2.3	3.18	3.97	5.16
xx09	36	12	4.7	9.59	9.98	11.04
xx09	26	9	5.1	6.63	11.73	12.07
xx68	41	3	4.8	6.46	10.7	11.81
xx71	42	2	6.5	7.25	15.56	15.66
xx08	41	14	5.0	6.12	19.76	19.83
xx43	44	8	4.9	5.6	14.56	15.76
xx51	47	5	3.2	5.05	13.03	15.47

Table B- 9: Marcellus – Mineralogy, TOC, Porosity and Surface area (Gas)

Depth	Clay wt%	Carbonate wt%	TOC Native wt%	Native Porosity %	Surf. Area Native m^2/g	Surf. Area Clean m^2/g
xx99	72	4	4.5	9.78	9.83	21.99
xx68	63	5	4.4	10.78	13.46	20.1
xx12	48	10	8.4	13.07	41.51	41.93
xx57	15	74	4.8	2.88	2.83	4.66

Table B-10: The maturity and the BET surface area of different kerogens. The samples highlighted in gray are from this study and compared with the data from literature.

Maturity Window	Formation	Tmax °C	BET – Surface Area (m^2/g)	References
Immature	Type II China	-	1.1	Wang et al., 2015
	Green River	417	3.74	This study
	Youganwo Formation – China	427	5.54	Cao et al., 2015
	Kimmeridge	422	7.06	This study
	Posidonia Shale WIC 7155	429	7.5	Rexer et al., 2014
	Woodford	420	9.24	This study
	WF Hydrous Pyrolysis - Native	424	10.8	Hu et al., 2015
	WF Hydrous Pyrolysis - 300C	429	11.2	Hu et al., 2015
	Posidonia Shale WIC 7145	425	12.5	Rexer et al., 2014
Oil	Bakken	435	15.81	This study
	Posidonia Shale HAR 7060	447	17.9	Rexer et al., 2014

	WF Hydrous Pyrolysis - 330C	439	18	Hu et al., 2015
	Wolfcamp - Key9	445	22.3	This study
	Posidonia Shale HAR 7038	449	27.3	Rexer et al., 2014
Gas Condensate	WF Hydrous Pyrolysis - 400C	-	26	Hu et al., 2015
	WF Hydrous Pyrolysis - 365C	463	27	Hu et al., 2015
	Eagle Ford	465	30.58	This study
	Marcellus	> 600	41.96	This study
	Posidonia Shale HAD 7119	459	56.1	Rexer et al., 2014
	Posidonia Shale HAD 7090	464	68.1	Rexer et al., 2014

Table B- 11: Mineral content, Organic matter content and the thermal maturity of the formations						
Formation	Well ID	TOC, wt.%	Clay, wt.%	Carbonate, wt.%	Tmax, °C	Maturity
Bakken	Bakken	0.2 – 15.5	3 – 39	3.0 – 27.0	< 435	Early Oil
Wolfcamp	Wolfcamp 1	0.4 – 3.3	10 – 36	6.0 – 56.0	< 435	Early Oil
	Wolfcamp 2	1.5 – 4.9	39 – 71	2.6 – 16.4	435 – 455	Oil window
	Wolfcamp 3	1.1 – 4.0	5 – 58	6.0 – 77.0	455 – 470	Condensate
	Wolfcamp 4	2.5 – 4.7	32 – 54	6.0 – 30.0	455 – 470	Condensate
Eagle Ford	Eagle Ford 1	1.6 – 15.0	6.0 – 33	54 – 86	435 – 455	Oil window
	Eagle Ford 2	1.6 – 7.9	4 – 26	59 – 88.5	455 – 470	Condensate
Woodford	Woodford	3.1 -8.0	31 – 46	8.0 – 21.0	455 – 470	Condensate
Vaca Muerta	Vaca Muerta	4.9 – 11.0	20 – 45	15 – 58	455 – 470	Condensate
Barnett	Barnett	3.2 – 4.9	26 – 47	2.0 – 14.0	475 – 485	Gas
Marcellus	Marcellus	4.1 – 8.4	15 – 72	4.0 – 73.5	> 600	Gas

Table B- 12: Geochemical properties of Eagle Ford-1 formation (Oil Window)										
	As-received					Solvent-extracted				
Sample No.	TOC, wt.%	Tmax, °C	S_1, mg HC/g rock	S_2, mg HC/g rock	HI	TOC, wt.%	Tmax, °C	S_1, mg HC/g rock	S_2, mg HC/g rock	HI
1	3.0	456	.54	1.04	64	2.8	452	0.16	0.49	40
2	2.6	455	1.07	2.1	107	2.4	451	0.16	0.75	57
3	3.2	455	0.52	0.63	58	1.4	451	0.14	0.24	29
4	1.6	449	0.45	0.78	73	1.2	448	0.16	0.36	41
5	1.9	452	0.53	0.68	66	1.6	446	0.16	0.28	40
6	13.4	449	15.93	9.72	176	7.5	457	0.25	2.88	89
7	15	452	10.89	10.95	179	7.6	457	0.25	4.59	97
8	14.2	452	15.79	9.58	161	7.7	457	0.25	4.17	93
9	11.2	449	4.82	7.8	168	5.7	457	0.23	3.52	90
10	14.8	451	19.5	9.2	147	6.7	457	0.23	4.02	91

Table B- 13: Geochemical properties of Wolfcamp – 2 formation (Oil Window)										
	As-received					Solvent-extracted				
Sample No.	TOC, wt.%	Tmax, °C	S_1, mg HC/g rock	S_2, mg HC/g rock	HI	TOC, wt.%	Tmax, °C	S_1, mg HC/g rock	S_2, mg HC/g rock	HI
1	3.1	448	1.45	2.24	91	2.8	439	0.24	0.77	37
2	3.8	447	1.65	3.35	104	3.7	447	0.27	1.72	60
3	2.1	444	0.93	1.18	74	2.0	443	0.22	0.47	37
4	2.9	443	1.12	2.21	101	2.6	445	0.21	0.78	42
5	2.8	446	1.38	2.03	92	2.7	444	0.22	0.83	40
6	3.1	448	2.03	4.39	109	2.9	449	0.30	5.81	99
7	5.3	447	1.47	2.34	94	4.6	444	0.22	0.49	36
8	7.9	444	4.93	11.5	168	6.9	451	0.21	1.08	57
9	2.6	435	0.41	1.08	68	2.6	452	0.34	2.47	59